SAPIENZA
UNIVERSITÀ DI ROMA

Nanostructured catalysts production through electrochemical methods: synthesis, characterization and possible applications

Facoltà di Ingegneria Civile e Industriale
Dipartimento di Ingegneria Chimica Materiali Ambiente
XXXII Ciclo Dottorato in Ingegneria Chimica

Antonio Rubino
Matricola 698650

Tutor
Prof.ssa Francesca Pagnanelli

A.A. 2018-2019

This page is intentionally left blank

Nanostructured catalysts production through electrochemical methods: synthesis, characterization and possible applications

Abstract

Abstract

In this work a study of the electrochemical synthesis of TiO_2 based nanostructured electrodes for photocatalytic and electrocatalytic applications is presented.

The study on the electrochemical synthesis of TiO_2 nanotubes (NTs) through anodization has been aimed to develop a novel “single-step” anodization method in symmetric electrochemical cells (i.e. both electrodes are Ti sheets), instead of traditional “double-step” processes, which include the sequence of two anodizations separated by the dissolution of the first formed TiO_2 and are carried out in asymmetric cells with Pt electrocatalysts as counter electrodes.

Besides the anodization, in relation to the specific applications discussed in this study, further electrochemical synthesis routes, employing the anodized TiO_2 electrodes, were investigated.

In photocatalytic applications, the electrodeposition of Cu_2O nanoparticles over the surface of TiO_2 NTs has been adopted as strategy to overcome the limited light absorption of the bare TiO_2 photocatalyst (active only under UV irradiation). Here, in agreement with most of the studies among the available literature, under visible irradiation the TiO_2/Cu_2O based electrodes showed improved performances than the bare TiO_2 (inactive under only visible light). These improved performances have been frequently claimed based on the only analysis of the photocatalytic performances under visible light, while in the present study it was found that, when the light source employed was UV + visible rather than only visible, the photo-catalytic performances of the composite electrodes were lower as compared to the bare TiO_2 electrode. Furthermore, the bare TiO_2 activity registered under UV + visible was higher than the composite electrode activity registered under only visible irradiation. To overcome this unexpected behaviour, at this stage the study has been aimed to the development of photo/electrochemical post-treatments, which allowed to improve the performances of the Cu_2O based electrodes also under UV + visible light.

Black TiO_2 electrocatalysts were finally synthesized in the framework of the activities related to the *e.THROUGH* EU project (H2020-MSCA-RISE-2017-778045), which is aimed to the recovery of critical raw materials and sustainable remediation.

Briefly, this goal would be achieved through the development of electrokinetic technologies for soil remediation, as in the case of the electrodialytic mine tailings remediation performed in this work, where the transport phenomena involved during EK processes (i.e. electromigration, electroosmosis and electrophoresis) are combined with the principles of the electrodialysis. Electrodialytic remediations are generally carried out in symmetric cells which employ commercial Ti/MMO (Mixed Metal Oxides; Ir/Ru-based) electrodes, for both anode and cathode, where the soil matrix to treat is separated by the electrodic compartments employing ionic exchange membranes. Main limit for the real employment of this technology is the energy costs related to the stirring, requested to favour the contaminants mobilization in the soil matrix, and the power supply. To overcome this limit and minimize the overall process cost, considering that the main reactions involved during the process are the water splitting reactions, one of the proposed strategies foresee the recovery of the evolved hydrogen as valuable byproduct. In this perspective, the employment of a specific hydrogen evolution reaction (HER) electrocatalyst instead of Ti/MMO, which is benchmark catalysts for the anodic reaction involved, would allow to boost the hydrogen production and further contributing to minimize the overall energy cost of the process. Consequently, at this stage the study has been aimed to the development of a non-commercial hydrogen evolution reaction (HER) electrocatalyst, namely the Black TiO_2 based electrodes. These electrodes have been synthesized through a facile electrochemical reduction strategy, starting from the amorphous TiO_2 based electrodes resulting from the anodization. The synthesized electrodes have been then tested in comparison to the commercial Ti/MMO cathode.

Chapter 1

Introduction

1 - Introduction

During the past several decades, the study of electrochemical phenomena (bulk phases phenomena as well as across interfaces between ionic, electronic, semiconductor, photonic, and dielectric materials) has advanced rapidly. This was owed, in large part, to the invention of a suite of new scientific tools, strictly connected to the development of nanotechnologies, which provided the ability to create precisely characterized systems, at unprecedented levels of sensitivity, atomic resolution, and chemical specificity. At the same time, that ability was made possible thanks to the development of electrochemical processes, either in the fabrication as well as in the functionalization of many nanostructured materials, processes and devices [1]. Today, many research groups working in nanotechnology also have wider interests in electrochemistry, as electrochemical methods are typically low-cost and highly effective for the preparation of nanostructures. This mutual interaction among the study of electrochemical phenomena and nanotechnologies, that is the applications of electrochemical phenomena in nanotechnology (e.g. nanomaterial synthesis through electrochemical methods), and vice versa (e.g. nanomaterials application in electrochemical systems), paved the way to the born of a new field that includes both, namely the Electrochemical Nanotechnology [2].

This work focuses the attention on that interaction, on one side toward the electrochemical routes for nanostructured materials synthesis, i.e. TiO_2 based electrodes synthesis, while on the other it is focused on their applications in photoelectrochemical, i.e. photoelectrochemical cells for Hydrogen production, and electrochemical systems, i.e. Electrodialytic systems for soil remediation.

1.1 Nanostructures through electrochemical methods

Transition to nanoscale, thanks to the strong reduction of the dimensions, results in a precise control of the surface geometry of nanostructured materials, which exhibits novel and unique catalytic, electronic, magnetic, optoelectronic and mechanical properties. These characteristics are the result of the collective behaviour and interaction of a group of nano-elements which acting together produce responses as a whole system [3]. These features led to a grown scientific interest of many research groups, involved in different topics, in the study of nanomaterials and their applications.

To date nanostructures are synthesized through a large variety of methods ranging from lithography [4], wet chemical processes employing microemulsion systems [5], electrochemical processes [6], photochemical reduction [7], and also soft chemical routes that includes sol-gel techniques [8] and wet impregnation [9].

Among them, electrochemical synthesis of nanostructures may be implemented following two different strategies, one based on the electrochemical oxidation, that includes the so called anodization processes, where the anodic polarization of metal substrates leads to the growth of nanostructured oxides, while the other one is based on the electrochemical reduction, namely the electrodeposition of metal or metal oxides over a conductive substrate. Both strategies are particularly effective when supported nanostructures over conductive substrates are needed.

Anodic polarization of valve metals, such as Al, Ti, Ta, Sb, Nb, V, Hf or W, started to grow interest in the last century in reason of the practical importance of the resulting bulk anodic oxides in applications such surface protection (i.e. metal passivation) and capacitors. In the last decades a further interest increase was registered for self-assembled nanostructured oxides, in reason of their unique and excellent properties for optical, electronic, photochemical and biological applications [1]. Besides that, the ordered nanoporous structure of some of these anodic oxides, like “honeycomb” structures for Al_2O_3, or nanotubes array for TiO_2, makes them materials of interest also as templates for the synthesis of nanostructured metals or metal oxides through electrodeposition techniques [10]–[13].

Electrodeposition indeed is the other electrochemical strategy (i.e. electrochemical reduction) previously mentioned as a tool for nanostructured materials synthesis. Besides template methods, several studies focused on the electrodeposition on conductive bulk substrates, demonstrated as by controlling the experimental conditions of the electrodeposition process is possible to control sizes and morphologies of the deposited nanostructures [14]–[16]. This latter aspect is of great interest, in particular in relation to catalytic purposes, considering that the catalytic activity would be strongly influenced by catalyst morphology and sizes [17].

In this work nanostructured TiO_2 based electrodes were synthesized through electrochemical routes. Specifically, anodization processes were carried out to synthesize Ti/TiO_2 nanostructured based electrodes, while Cu_2O electrodeposition was successively performed to improve the TiO_2 based electrodes characteristic respect to the photocatalytic application. Furthermore, electrochemical methods have been employed also as post-treatments useful to improve the TiO_2 based electrodes for both, photocatalytic and electrocatalytic purposes. Electrodes synthesis and their applications will be widely discussed in the following sections.

Chapter 2

TiO_2 Nanotubes (NTs) synthesis

2 TiO_2 Nanotubes (NTs) synthesis

2.1 State of the art

Different techniques have been developed to produce nanostructured TiO_2, such as sol-gel synthesis [18], anodization [19], electrodeposition [20], sonochemical deposition [21], and hydrothermal techniques [22], with different geometrical shapes and structures. Among these, potentiostatic anodization, which is a low cost nanofabrication method, leads to nanotubular structures that show a high surface to volume ratio [23]–[26]. Besides the cost effectiveness the main advantage of the anodic polarization is in its versatility, allowing to have control on dimensions and morphology of the resulting oxide by the modulation of anodizing parameters like voltage, pH, composition of the electrolyte and time of electrolysis [23], [27], [28].

Highly ordered vertically oriented TiO_2 nanotubes, in reason of the ordered material architecture, are excellent electron percolation pathways for vectorial charge transfer between interfaces [29]. These characteristics confer outstanding charge transport and carrier lifetime properties which makes this material particularly appealing in such advanced applications, including sensors [30], dye sensitized solar cells [31], hydrogen generation by water photoelectrolysis [32], photocatalytic reduction of CO_2 [33], energy storage devices [34] and supercapacitors [35]. Furthermore, TiO_2 NTs demonstrated great utility in biomedical related applications including biosensors, molecular filtration, drug delivery, and tissue engineering [29].

As above mentioned, anodization as production method gives the possibility to design and control the geometrical features of the self-organized nanotubular architecture, allowing to achieve a material with specific light absorption and propagation characteristics, which makes this material of great interest in photocatalytic applications [36]–[38]. As well as by an electrocatalytic point of view, considering that in many electrochemical reactions the electrolyte diffusion can be tuned by tailoring the pore sizes of the porous materials [39].

In literature a large variety of works on the TiO_2 NTs synthesized through anodization processes is present. They can be classified in relation to the employed electrolyte in four different generations. First NTs generation derives from anodizations carried out in acidic fluoride-based electrolytes, characterized by a maximum nanotube lengths of approximately 500 nm [40]. In the second-generation, to reduce the chemical dissolution of TiO_2 during the anodization, buffered pH electrolytes were employed, reaching NTs lengths up to approximately 5 µm [41]. A further increase in NTs length, nearly 1000 µm, was reached with the third NTs generation which was developed employing non-aqueous polar organic electrolytes containing fluoride [27], [30], [42]. The fourth generation, unlike previous, is characterized by non-fluoride-based electrolytes [43], using HCl [44], H_2O_2 aqueous electrolytes with nanorods morphology instead of NTs [45] and the combination of both of them [46].

The general growth mechanism of nanoporous anodic oxides during anodization (Figure 2.1) can be explained as the contribution of different processes. Oxide growth starts at the metal/electrolyte interface through the interactions between the metal and O_2^- or OH^- ions. Once the initial oxide layer is formed, O_2^- anions migrate through it toward the metal where they react, and the oxide growth go on.

At the meantime, in reason of the applied electric field, metal ions move in the opposite direction, from the bulk metal toward the oxide/electrolyte interface and are ejected, while the formed oxide undergoes polarization promoting dissolution of the metal cations (i.e. field assisted dissolution), which dissolve into the electrolyte, and the free O_2^- anions migrate towards the metal/oxide interface, as in the first step described above, to interact with the metal. Besides that, chemical etching by the acidic electrolyte on the formed oxide also takes place during anodization [47].

As reported in several works, this latter aspect is of great importance in fluoride based electrolytes where the chemical dissolution plays a key role both, in the formation of nanotubes instead of nanoporous continuous layer, either in top nanotubes morphology [31], [48], [49].

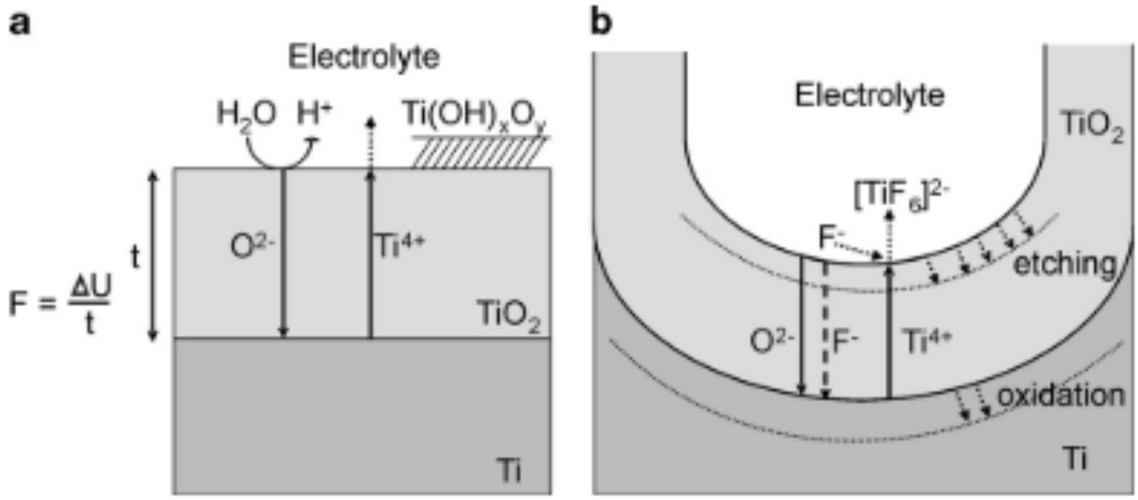

Figure 2.1 - Schematic representation of the Ti anodization (a) in absence of fluorides (flat layers), and (b) in presence of fluorides (tube growth) [24].

2.2 Anodization process: TiO_2 NTs growth

Anodization is an electrochemical process generally carried out in acidic aqueous solution, where the growth of an oxide layer on the surface of a suitable metal takes place under a sufficient applied potential. During the current flow in the electrolytic cell, in which the metal substrate is employed as anode, the anions migrate towards the anode oxidizing it. According to the electrolyte composition and the specific experimental conditions of the anodization process, three different scenario may occurs: I) the metal is continuously dissolved with Mn^+ ions which are solvated in the electrolyte (i.e. corrosion, or electropolishing of the metal); II) a compact oxide layer is formed in reason of the Mn^+ reaction with O_2^-, with the resulting oxide which is insoluble in the anodization electrolyte (Figure 2.1, a); III) under some conditions, a porous oxide layer is the result of the competition between solvation and oxide formation (Figure 2.1, b), where oxide solubility in the electrolyte plays a key role in the self-organized nanoporous oxide growth [26].

Since first report in 1999 by Zwilling and co-workers on anodic oxide growth on titanium substrate [40], was well recognized that the fluoride content in the electrolyte was the crucial factor in nanotubes self-organized growth. Anodization in fluoride-based electrolytes to form tube layers is usually carried out applying a constant potential in the range 5 – 150 V, with a fluoride content in the range 0.1 – 1 $\%_{wt}$ [26], [27], [31], [41].

The growth mechanism of nanoporous anodic oxides during anodization in non fluoride-based electrolyte, as reported by Schmuki et al. [1], can be summarized as the contribution of the following reactions:

$$Ti \rightarrow Ti^{4+} + 4e^- \tag{2.1}$$

$$Ti + 2H_2O \rightarrow TiO_2 + 4H^+ + 4e^- \tag{2.2}$$

$$Ti^{4+} + 4H_2O \rightarrow Ti(OH)_4 + 4H^+ \tag{2.3a}$$

$$Ti(OH)_4 \rightarrow TiO_2 + 2H_2O \tag{2.3b}$$

$$2H_2O + 2e^- \rightarrow H_2\uparrow + 4OH^- \tag{2.4}$$

These equations describe the compact oxide layer growth: ion formation (2.1); reaction with O_2^- (2.2) or OH^- (2.3); and the cathodic reaction of hydrogen evolution (2.4). Specifically, oxide growth starts at the metal/electrolyte interface through the interactions between the metal and O_2^- or OH^- ions, generated by the field assisted deprotonation of OH^- or H_2O, respectively. Once the initial oxide layer is formed, in reason of the electric field, anions migrate through the formed oxide toward the metal where they react and the oxide growth go on (Figure 2.1).

In fluoride-based electrolytes are implied two further reactions:

$$Ti^{4+} + 6F^- \rightarrow [TiF_6]^{2-} \tag{2.5}$$

$$TiO_2 + 6F^- \xrightarrow{H^+} Ti + 2H_2O \tag{2.6}$$

namely the complexation of the ions that are moving through the formed oxide and are ejected in the electrolyte (2.5); and the chemical etching of the fluoride on the formed oxide (2.6).

According to that, appears clear as the fluoride content and pH would strongly influence the overall anodization process, as well as the anodization time. While it is well defined the linear relation between nanotubes outer diameter and anodization potential [24], [50], the nanotubes length results strongly influenced by the etching effect promoted by the same anodization electrolytes. Consequently, to achieve the fine control on NTs length, the optimization of the anodization parameters is needed [49].

Anodization carried out in non-aqueous polar organic electrolytes containing fluoride, was specifically developed to improve the nanotubes length thanks to the low water content [27], [30], [42]. Specifically, reduced water content (i.e. lower than 5%) strongly decrease the etching rate, and longer nanotubes would be achieved [29]. It should be remarked at the same time that organic electrolytes imply a reduced oxygen availability, which would lead to a decrease in the oxide formation rate [51].

Appears clear as the electrolyte composition would play a key role in determining the nanotubes morphology, as in the formation of “V-shaped” sidewall thickness profiles (i.e. thinner sidewall on the top, thicker at the bottom), strictly connected to the electrolyte etching effect [52]. Considering that this etching effect is permanent during the anodization, the V-shaped profile evolves as function of the anodization time, in a continuous thinning of the top tubes until they collapse, leading to a disordered top tubes layer called nanograss [48], [52].

Consequently, fixed the fluoride content and the applied potential, the inner tube diameter such as the top tubes morphology could be finely controlled through the combination of water content in the electrolyte, as well as the anodization time. This control on the pore size of the nanostructures would results in the tuning of the electrolyte diffusion, useful to regulate many electrochemical and photochemical processes [39].

Titania nanotubes gained by anodization in fluoride-based polar organic electrolytes are generally synthesized in “asymmetric” two electrodes electrochemical cells, generally employing Pt as counter electrode [23], [35], [53].

The most diffused anodization methods are based on “double step” processes (Figure 2.2, A), where after the first anodization, the formed oxide is selectively removed by the titanium substrate leaving an imprinting on its surface which is useful to guarantee the self-ordered growth during the second anodization [54], [55], while are very few works based on single anodization processes [53], [56], among which must be highlighted some works where the authors proposed single step anodizations characterized by a potentiodynamic regime in the early stage of the process, with the linear growth of the applied potential up to the value of the subsequent potentiostatic anodization (Figure 2.2, B), reached which the anodization proceeds in potentiostatic regime [57].

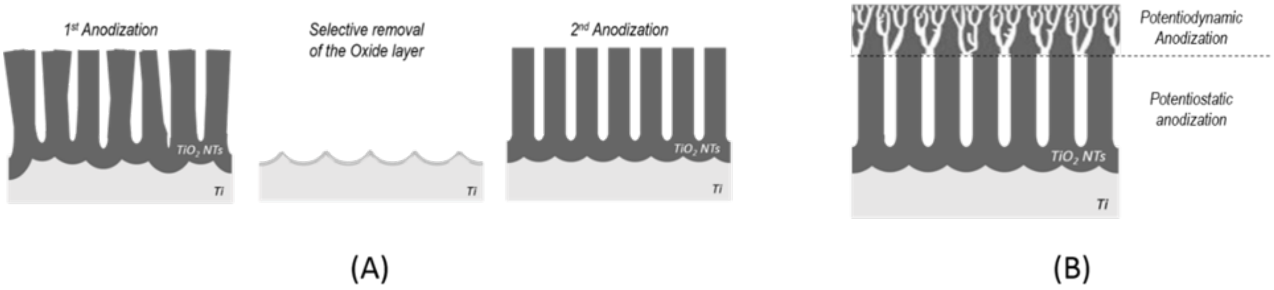

Figure 2.2 - Schematic representation of: A) typical “Double-step” anodization; B) “Single-step” anodization with potentiodynamic pretreatment [58].

2.3 Annealing treatment. From amorphous TiO_2 to its crystal phases

Titanium dioxide exists in three different crystalline phases: anatase, rutile and brookite [59], while the TiO_2 NTs resulting from the anodization process are characterized by an amorphous nature [60].

It is well recognized that for photocatalytic purposes the most photoactive phase is Anatase TiO_2 [61]. It is a metastable phase which for high annealing temperature converts to Rutile, the thermodynamically stable phase. Both, Anatase and Rutile crystallize in tetragonal structures [62].

Some works report on partial crystallization achieved already during the anodization for certain electrolyte compositions and anodization potentials [63], [64], while the most common method employed to improve the crystallinity of the Titania nanotubes is based on annealing treatments [65]–[67].

Annealing temperature and duration are the parameters that allow to control the crystal phases ratio of the treated nanotubes, so that an increase in temperature and duration results in the transition from Anatase to Rutile phase [68].

In several works Authors report on annealing treatments carried out in different atmospheres, like in argon, air or nitrogen flow [24], [69]. In this latter case the annealing treatment allows to have the contextual doping of the Titania NTs, thanks to the incorporation of nitrogen into the TiO_2 lattice [70].

Chapter 3

TiO_2-based photocatalysts for solar energy conversion

3 TiO_2-based photocatalysts for solar energy conversion

3.1 Solar energy conversion through semiconductor photocatalysts

The increasing atmospheric concentration of greenhouse gases and the related risks arising from global warming raises serious concerns on fossil fuels energy supply [71]. To date, great attention is paid to the development of renewables-based energy production systems (e.g. solar, photovoltaic, geothermal) [72].

The real employment of renewables in large scale energy production is limited by the large degree of intermittency of which are characterized. Cause the natural variability of climate factors, as well as the geographic position, the adoption of renewables as continuous supply sources is precluded. As consequence electric energy from renewable productions imposes the recourse to storage technologies, including batteries and accumulators, which are however insufficient to guarantee the required autonomy in many applications [73].

A promising strategy to overcome these limits, is the conversion of the produced energy in chemical fuels, which can be stored and later used to generate power. Among the fuels that can be produced, attention has been paid to hydrogen, mainly for its high energy density and null environmental impact deriving from its combustion [74]. Photocatalysts employed for that purpose are semiconductor materials, among which are included transition metals oxides, like titanium dioxide [75].

Figure 3.1 shows a schematic representation based on the energy band model. When the atoms form a crystal, the motion of the electrons of the outermost layer is modified respect to what happens for an isolated atom. The electrons are no longer bound to a single atom but are shared between multiple atoms (which form the lattice structure). As consequence the allowed energy levels close together lead to the bands formation. In a conductor (Figure 3.1, metal) these bands are overlapped, so that the electrons which occupies the lower energy level, i.e. valence band, in presence of an external electric field can acquire sufficient energy to move freely within the crystal. Otherwise in an insulator the energy bands are separated by a forbidden band gap characterized by high energy. Under an external electric field, in reason of the high energy band gap, electrons cannot acquire sufficient energy to move in the conduction band.

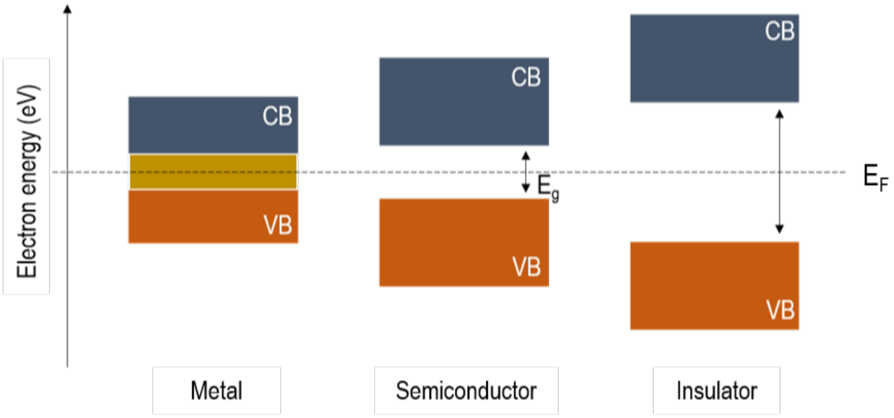

Figure 3.1 - Schematic representation based on energy band model. Comparison between metal, semiconductor and insulator respect to the Fermi energy level (E_F). E_g is the energy band gap characteristic of the semiconductor; VB and CB are the Valence and Conduction Bands respectively.

Semiconductors, compared to insulators, are characterized by lower energy band gaps which allows to acquire sufficient energy useful to guarantee the conduction. When this happens, e.g. under solar irradiation, an electron is promoted from the valence to the conduction band, leaving a hole in the lattice structure (i.e. incomplete bound in the lattice). In this situation it is possible that an electron of a neighboring atom goes to fill the formed hole producing in turn a new hole. Subsequent movements of the electrons produce a “movement of the hole” through the crystal, so that the hole behave like a particle with a positive charge, free to move in the opposite direction to the motion of the electrons within the crystal.

An “intrinsic” undoped semiconductor is characterized by the absence of defects in its lattice structure, and the concentration of the charge carriers, i.e. electrons and holes, is constant. This condition is represented by the Fermi level (E_F) which lies in the mid of the semiconductor band gap. This is why the Fermi level can be considered to be a hypothetical energy level of an electron, such that at thermodynamic equilibrium this energy level would have a 50% probability of being occupied at any given time [76].

The introduction in the crystal of substitutive impurities, i.e. foreign atoms that replace some of the atoms in the original lattice structure, involves the modification of the concentrations of electrons and holes respect to the intrinsic semiconductor. This procedure is generally named doping.

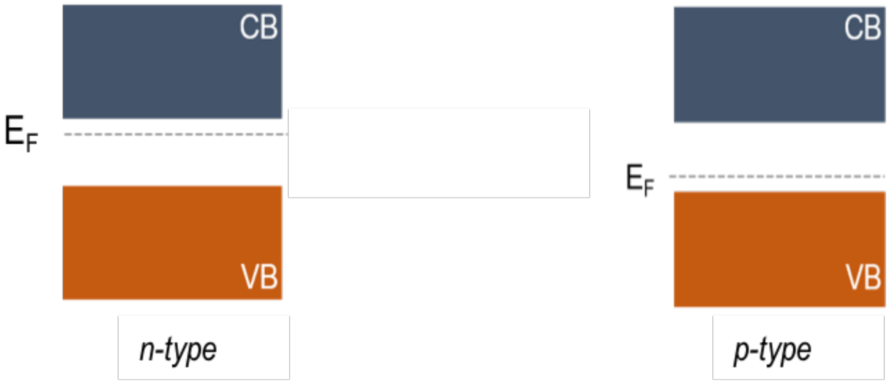

Figure 3.2 - Schematic representation based on energy band model. Comparison between n-type and p-type semiconductors.

According to the valence electrons of the substitutive atom, two kinds of doping are possible. Lower valence atoms are called acceptors and cause an increase in the concentration of holes leading to *p-type* semiconductors, while higher valence atoms are called donors and cause an increase in the concentration of the electrons leading to *n-type* semiconductors (Figure 3.2). As showed the Fermi levels are shifted towards the conduction band and the valence band for *n-type* and *p-type* respectively, as consequence of the varied concentrations of the majority charge carriers.

TiO_2 is an *n-type* semiconductor able to promote the photocatalytic water splitting. The main feature that semiconductors must possess in order to promote both the water splitting reactions is related to the energies of the conduction and the valence bands, which must restrain the water reduction and oxidation potentials respectively, as in the case of *n*-TiO_2 (Figure 3.3).

In principle, when the photocatalyst is subjected to illumination, the supplied energy allows the electrons present in the semiconductor valence band to overcome the forbidden energy band (i.e. energy band gap) and pass into the conduction band leaving a positive charge in the valence band, the so-called hole-electron pairs formation. In photocatalytic cells for water splitting the overall reaction takes place over the photocatalyst surface, so that the photogenerated electrons promote the water reduction at the conduction band, while the holes promote the water oxidation at the valence band, closing the photo-electrolysis (photo-splitting) [77].

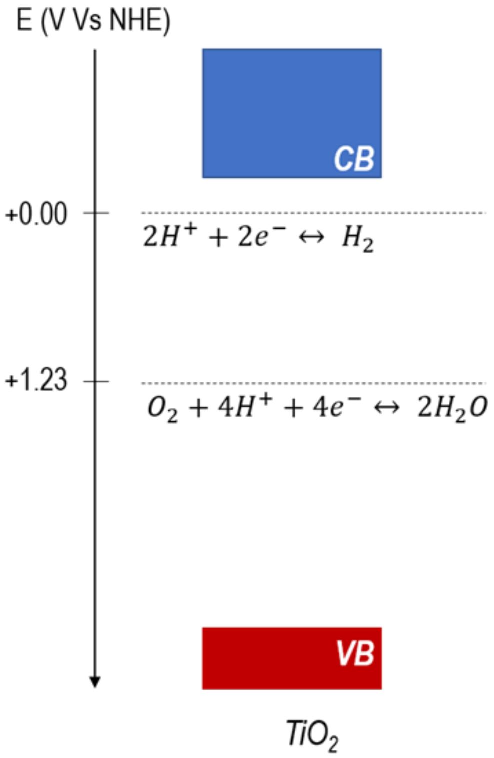

Figure 3.3 - Schematic representation of the relation between energy band levels of TiO_2 semiconductor and water reduction and oxidation potentials. CB and VB are the conduction and valence bands respectively.

Besides photocatalytic cells, is possible to employ the photocatalysts in systems called photoelectrochemical (PEC) cells, where, according to the type of doping, they can be employed as photoanodes (*n-type*) or photocathodes (*p-type*), or both in a tandem cell configuration [78]. Respect to photocatalytic cells where the overall electrolysis reaction takes place over the photocatalyst surface, in PEC cells the photocatalyst which acts as photoelectrode will be responsible only for a half reaction. For example, referring to a PEC cell based on a *n-type* photoanode and a metal as counter electrode, under illumination the photogenerated electrons will be driven to the counter electrode, where they promote the reduction, while the holes will promote the oxidation over the photocatalyst surface.

Titanium dioxide is one of the most studied photocatalysts, since Fujishima and Honda in 1972 for the first time demonstrated its employment in photocatalytic water splitting [79].

The main features that justify the extensive investigation on this material through the last decades, are related to its high photocatalytic activity, photochemical stability, non-toxicity and low cost, besides the advantages related to the nanotubular architecture, which thanks to an elevate surface to volume ratio can ensures a high number of photogenerated charge carriers and their reduced recombination rate as a function of NTs length, enhancing the overall process kinetic [80].

On the contrary, main limit for the TiO_2-based photocatalyst activity is its wide band gap (i.e. 3,0 - 3,3 eV [81], [82]), that makes it suitable only for UV light absorption, with the consequent absence of photoactivity in the visible region of solar spectrum.

This can be explained considering that the band gap corresponds to the minimum energy required to have photoactivity (i.e. to promote an electron from the valence to the conduction band). As a consequence, considering that the energy source employed is the solar light, and that there is an inverse proportionality between the energy and the light wavelength, there will be a threshold wavelength value which will define the wavelength range that could be absorbed for each semiconductor, so that wider will be the band gap, lower will be the absorbed light fraction, and vice versa.

TiO_2 energy band gap, as above mentioned allows to absorb light only in the UV region, which corresponds to 3-5% of the entire solar radiation, while more than 40% is in the visible region. Consequently, a lot of researcher efforts has been devoted to the study of strategies for the improvement of the visible light absorption in TiO_2-based photocatalysts.

One of the strategy commonly employed is based on doping of TiO_2 with transition metal ions, like Co, Cr, Cu, Fe, Mo, V and W [83]. The presence of foreign metal species induces defects formation in the oxide structure, which produces as effect a variation in the number of the intrinsic charge carriers, so that substituted elements with higher valence number respect to Ti would increase the number of holes as charge carriers, conferring a p-type character to the semiconductor (holes as majority charge carriers), while elements with lower valence number would increase the number of electrons, n-type character (electrons as majority charge carriers). Most recently also anion-doped TiO_2 has attracted considerable attention due to its reported photocatalytic activity under visible light irradiation [84].

Doped TiO_2 results in band gap positions which shows a noticeable shift of light absorption towards the visible region [83]. At the same time, the nature of the dopants would strongly influence the photoactivity, depending on dopants energy levels and d-electron configurations [85]. Specifically, when TiO_2 is doped with 3d transition metals (i.e. V, Cr, Mn, Fe, or Co), the electrons are localized around each dopant. As the atomic number of the dopant increases the localized level shifts to lower energy. For example, in the case of Co dopants, it is situated at the top of the VB. In contrast, the electrons from the Ni dopant are rather delocalized, thus significantly contributing to the formation of the valence band with the O 2p and Ti 3d electrons.

Another route provides to couple TiO_2 with other materials. On one side through the deposition of metals which would act as co-catalyst and contextually as “electron trap sites” minimizing the charge carriers recombination probability in the TiO_2 substrate and improving the photoactivity (i.e. employing the “trap state electrons” in the reductions at the metal/electrolyte interface). On the other side the deposition of a suitable semiconductor that would be able to absorb light in visible region acting in tandem with the TiO_2 substrates [77].

3.2 Photoelectrochemical cell (PEC)

Figure 3.5, B shows a schematic representation of a photoelectrochemical cell based on n-type semiconductor at the equilibrium (i.e. dark conditions). As previously mentioned, the Fermi energy level of a semiconductor represents an energy level which has 50% probability of being occupied by an electron [76]. It is located near the middle of the band gap for undoped semiconductors, while it is near the conduction band for an n-type semiconductor (electrons as majority charge carriers), and the valence band for a p-type semiconductor (holes as majority charge carriers). In vacuum the Fermi energy level corresponds to the “Flat band” potential. When a semiconductor metal oxide is exposed to air, water molecules from the air can dissociatively adsorb on its surface, resulting in -OH surface termination which form new electronic surface states within the bandgap of the semiconductor (after the adsorption the symmetry of the bulk lattice at the semiconductor/air interface is broken). The energy levels of these new surface states are below the conduction band, so that free electrons from the semiconductor bulk moves to occupy these levels, leaving ionized donors which form a positive space charge layer (i.e. depletion layer – Figure 3.4, f). An electric field now forms, and the charge transfer from bulk to surface will continue until the potential barrier becomes too large for bulk electrons to cross it. At this point, a dynamic equilibrium establishes at which no net electron transport takes place (Figure 3.4, [86]).

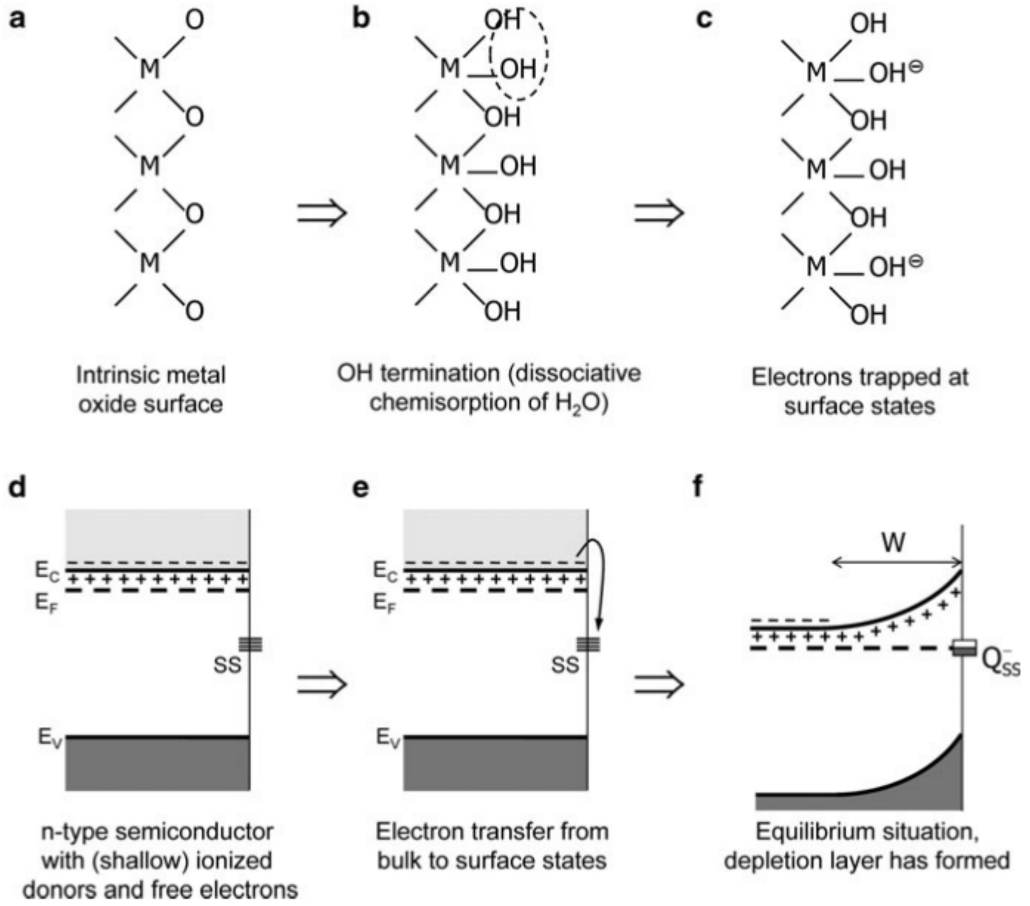

Figure 3.4 - Simplified illustration of the formation of a space charge region (SCR) at a metal oxide semiconductor surface when exposed to (humid) air. a, d) n-type semiconductor in vacuum; b, e) dissociatively absorption of water and c, f) new electronic surface states formation, [86].

In the same way, when the n-type photoanode (Figure 3.5, A) is immersed in the electrolyte a dynamic equilibrium is established in reason of the charge transfer across the semiconductor/electrolyte interface (Figure 3.5, B), and the Fermi energy level of the semiconductor shifts from the flatband potential to equalize the energy level of the redox couple (i.e. O_2/H_2O) in the electrolyte, giving rise to the “band bending” phenomenon. When the PEC cell is illuminated, the photogeneration of the hole-electron pairs in the semiconductor takes place, and the Fermi level varies decreasing the band bending, towards the flatband potential starting value.

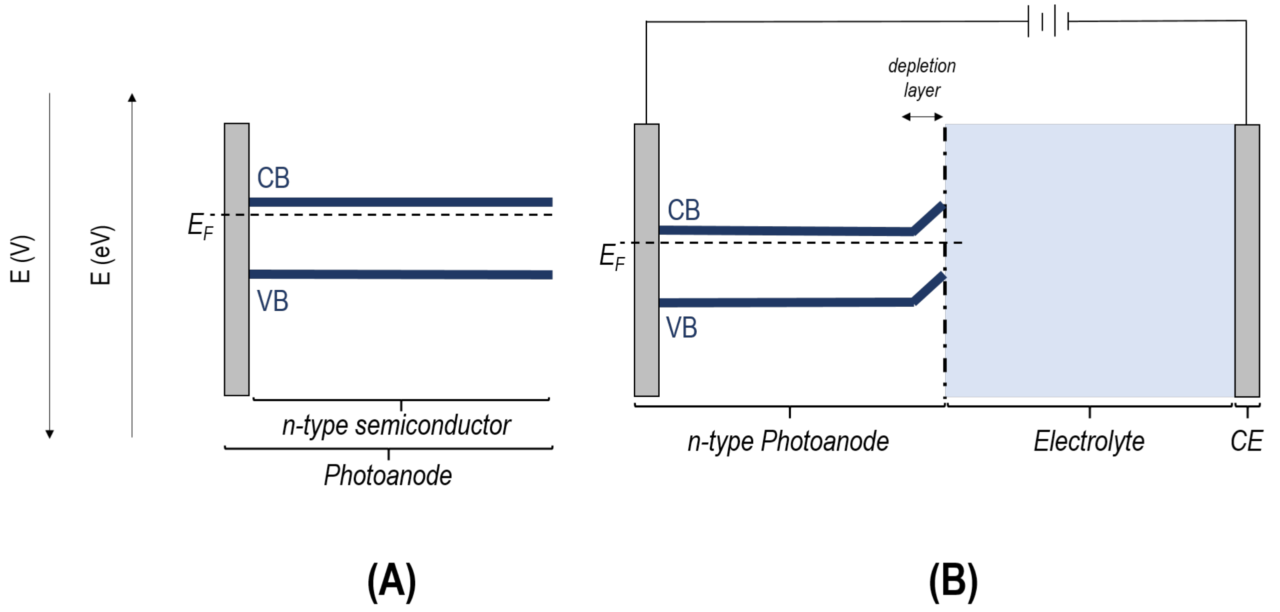

Figure 3.5 – Schematic representation of: A) n-type based photoanode; B) PEC cell employing n-type photoanode at the equilibrium, with depletion layer formation. VB and CB are the valence and conduction bands respectively, E_F is the Fermi energy level and CE is the counter electrode.

This “band flattening” under illumination, due to the variation of the charge carriers concentration (i.e. replacement of the electrons concentration in the depletion layer), is traduced in an internal photovoltage (ΔV_{photo}) generation (Figure 3.6), which is the driving forces of the electrochemical reactions in the PEC cell [87].

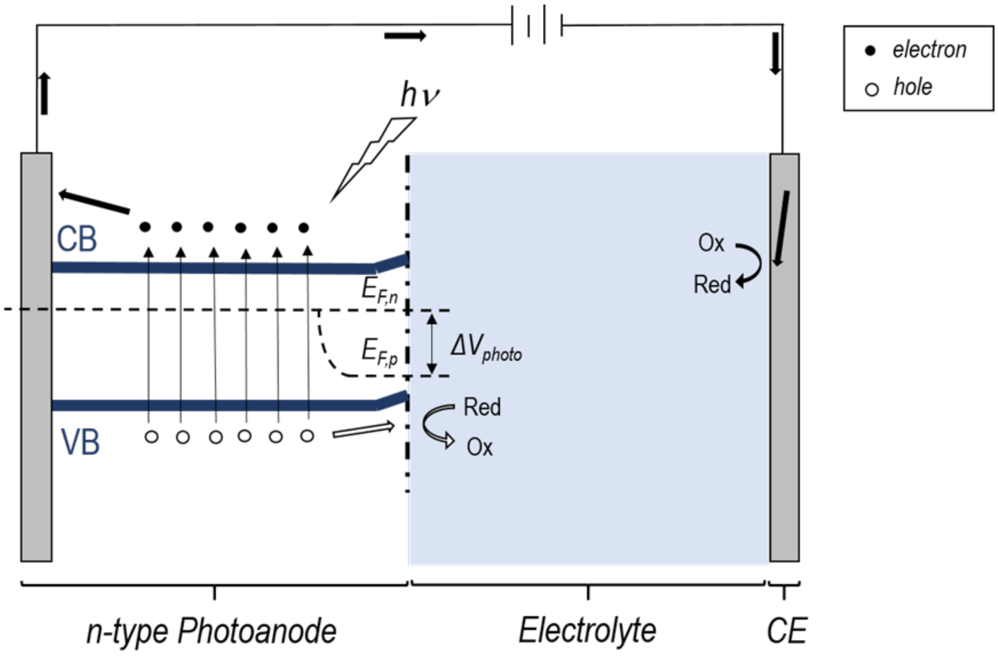

Figure 3.6 – Schematic representation of a PEC cell employing n-type photoanode under illumination. ΔV_{photo} is the potential difference between $E_{F,n}$ and $E_{F,p}$, which are the quasi Fermi level for the electrons and the holes respectively.

ΔV_{photo} drives the photogenerated electron flow from the semiconductor towards the counter electrode promoting the reduction reaction, while over the semiconductor electrode surface the holes promotes the oxidation reaction (Figure 3.6).

At this stage, since the system is no longer in equilibrium, the use of a single Fermi level is no longer appropriate, so that the concept of *quasi-Fermi level* (Figure 3.6, $E_{F,n}$ and $E_{F,p}$) would be more useful [88]. Considering the photovoltage it could be defined as the potential difference between the quasi-Fermi levels of electrons ($E_{F,n}$) and holes ($E_{F,p}$) under illumination, although the accuracy of this formalism, particularly in the vicinity of semiconductor-liquid interface, remains an active area of discussion within the PEC community [89]. Van de Krol defined it as a direct measure of the concentration of electrons and holes at a certain point *x* in the semiconductor bulk respect to the surface state at the semiconductor/electrolyte interface [90].

3.3 Strategy to enhance the light absorption in Titania based photocatalysts: Ti/TiO_2/Cu_2O electrodes synthesized through Cu_2O electrodeposition

Thanks to the unique characteristics that the nanotubular architecture confers in terms of electron percolation pathways for vectorial charge transfer between interfaces [29], n-TiO_2 NTs is one of the most studied and appealing photocatalysts.

Furthermore, NTs morphology enables light to be internally scattered, increasing the chances to have more photons absorbed [54]. Zhu et al. in particular calculated that the light harvesting efficiency of TiO_2 nanotubes is 20% larger compared to nanoparticle films used in dye sensitized solar cells [91].

Unfortunately, the limited light absorption to the UV region of the solar spectrum, due to the wide band gap of which this semiconductor is characterized [81], greatly reduces its performances in terms of photoconversion efficiency. This is why during the years different strategies have been adopted to improve the light absorption in Titania based photocatalysts [92]. As previously mentioned, these strategies includes the incorporation of dopants in TiO_2 lattice structure, useful to narrow the band gap [83], [93]–[95], and the formation of semiconductors heterojunction, achievable through the deposition of a suitable semiconductor able to absorb visible light [92], [96]–[98].

Although doping would be the first useful strategy to this goal, the main effect that produces is a shift in the band gap energy toward lower energy (i.e. , ranging from 2.4 to 3.1 eV, [93]), that are in some cases not so lower respect to the undoped Titania (i.e. approximately 3.2 eV, [29]), so that absorption respect to the visible light remains almost unchanged. Consequently, the deposition of a semiconductor able to absorb in visible seems to be a more promising strategy to extend the range of the light absorption towards the visible region. Cuprous oxide, which is a p-type semiconductor (Figure 3.2, B) characterized by a narrow band gap (i.e. ranging from 2.0 to 2.6 eV, [29], [99]), is one of the candidates to this latter purpose. It is a low cost, environmentally compatible and abundant metal oxide [100].

Traditionally, Cu_2O deposition techniques include the impregnation of nanostructured TiO_2 with a copper salt and subsequent calcination. These methods offer low control on deposited particles (e.g.: size, shape, composition), whose mainly determine the TiO_2-Cu_2O system activity [101].

Electrochemical deposition is one of the most versatile and cost effective methods to deposit semiconductor nanoparticles over Titania nanotubes [102], [103]. This method allows to have a facile control on sizes and morphology of the deposited particles by tuning the experimental conditions [102], [104]–[106].

Cu_2O electrodeposition is generally carried out employing Ti/TiO_2 substrates as working electrodes in alkaline electrolytes composed of copper (II) sulphate and lactic acid, which act as complexing agent for Cu [36], [107]–[110]. The Cu_2O electrodeposition employing copper sulfate based electrolytes occurs following the simultaneous reactions reported below [102]:

$$Cu^{2+} + e^- \rightarrow Cu^+ \qquad (3.1)$$

$$2Cu^+ + 2OH^- + 2e^- \rightarrow Cu_2O + H_2O \qquad (3.2)$$

In alkaline solutions the presence of lactic acid, which forms soluble copper lactate complex, is required to stabilize Cu^{2+} ions and prevent the precipitation of $Cu(OH)_2$ [111], [112]. As reported by Bijani et al., based on thermodynamic calculations, the predominant complex is CuLac2, and the electrochemical reduction of Cu^{2+} to Cu_2O involves the formation and dehydration of a CuOH intermediate [113]:

$$CuLac_2 + OH^- + e^- \rightarrow CuOH + 2Lac^- \quad (3.3)$$

$$2CuOH \rightarrow Cu_2O + H_2O \quad (3.4)$$

The electrodeposition strategy for TiO_2 enhancement above mentioned and the TiO_2 NTs production through anodization of titanium substrates, in addition to the advantage to give low cost and versatile electrochemical routes for the photocatalyst synthesis, offer the possibility to integrate the two steps of the production in a single unit which would be particularly appealing in a production process scalable perspective.

3.4 TiO_2-Cu_2O p-n heterojunction in photoelectrochemical (PEC) cells

The deposition of a suitable semiconductor over the Ti/TiO_2 NTs electrodes produces as result the formation of a heterojunction between semiconductors. This coupling, in addition to the range extension of the useful wavelengths to promote photoactivity, would lead to an increase in the photocatalytic efficiency also through the enhancement of the charge carriers separation due to the relative energy bands position which characterize the two different semiconductors, increasing the charge carriers lifetime.

Depending on the characteristic energy band position of the two semiconductors, three different configurations of the heterojunction can be possible (Figure 3.7).

Among them the configuration *Type II* reported in Figure 3.7, is the configuration which guarantees an efficient separation of the photogenerated charge carriers. Indeed, the conduction band of A side is less cathodic than the B side, while the valence band in B side is less anodic than in A side, so that under illumination the photogenerated electrons would be injected from B to A and the holes would migrate in the opposite direction, minimizing their recombination. This type of configuration would be representative for TiO_2 (A side) and Cu_2O (B side).

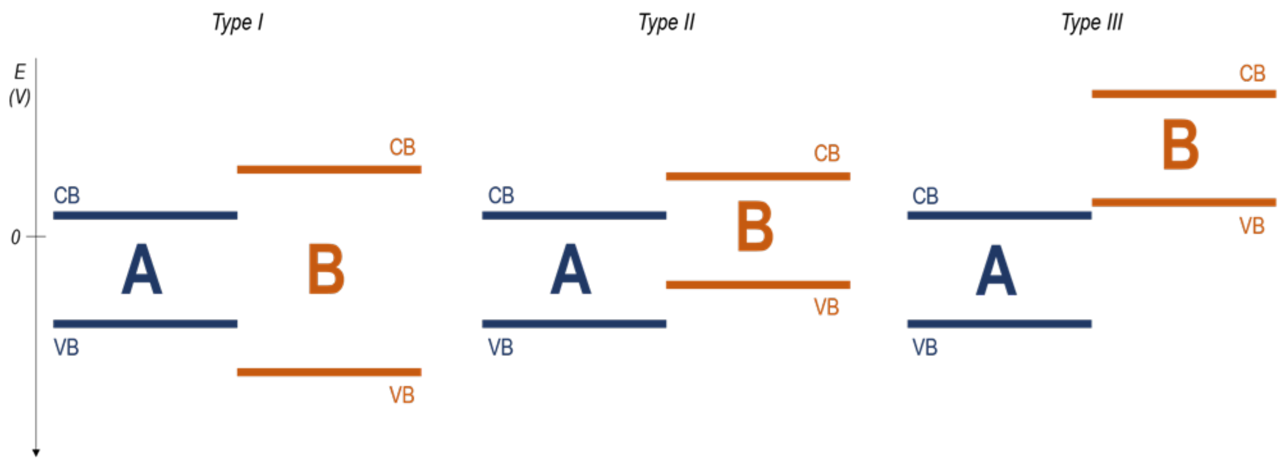

Figure 3.7 - Schematic representation of the relative energy bands position of the two semiconductors involved in the heterojunction in the three possible different cases (Type I, II and III). It Should be noted that this schematic representation is not representative of the established equilibrium when the heterojunction is formed but is representative only of the relative energy bands position of the two semiconductors before that equilibrium is established.

Besides that, the heterojunction behavior in terms of current flow in a PEC cell is strictly connected to the type of doping of the two semiconductors that are forming the junction. As mentioned in paragraph 3.2, when a semiconductor is exposed to air a space charge layer is formed in reason of the new electronic surface state deriving from the interaction of the semiconductor with the air. The same situation happens when the semiconductor being brought in contact with a metal or another semiconductor [114], where in reason of the different Fermi energy levels (i.e. different electronic state), a charge transfer between them occurs until a dynamic equilibrium is established, at which no net electron transport takes place [66]. The charge transfer is the results of the free electrons that move from the n-side toward the p-side. These electrons diffuse across the junction toward the p-side to combine with holes (i.e. acceptor atoms in the lattice structure of the p-type semiconductor) and form new negative ions, leaving positive ions in its back (i.e. donor atoms in the n-side). A space charge across the junction builds up, creating a depletion layer which inhibits any further electron transfer unless it is helped by a forward bias. As a consequence, a p-n heterojunction based photoelectrode can be described as a basic diode with the current which can flow in one direction (i.e. from *p* to *n* side; forward bias) but not in the other (i.e. from *n* to *p* side; reverse bias). This is why under illumination, in principle, a p-n heterojunction would act as photoanode in a PEC cell.

Composite Ti/TiO$_2$/Cu$_2$O electrode/electrolyte interface at the equilibrium is represented schematically in Figure 3.8 (I). In principle, the photogenerated electrons will flow from B to A and then through the ohmic contact toward the counter electrode were the reduction takes place, while the holes migrate from A to B promoting the oxidization over the composite electrode surface (Figure 3.8, II).

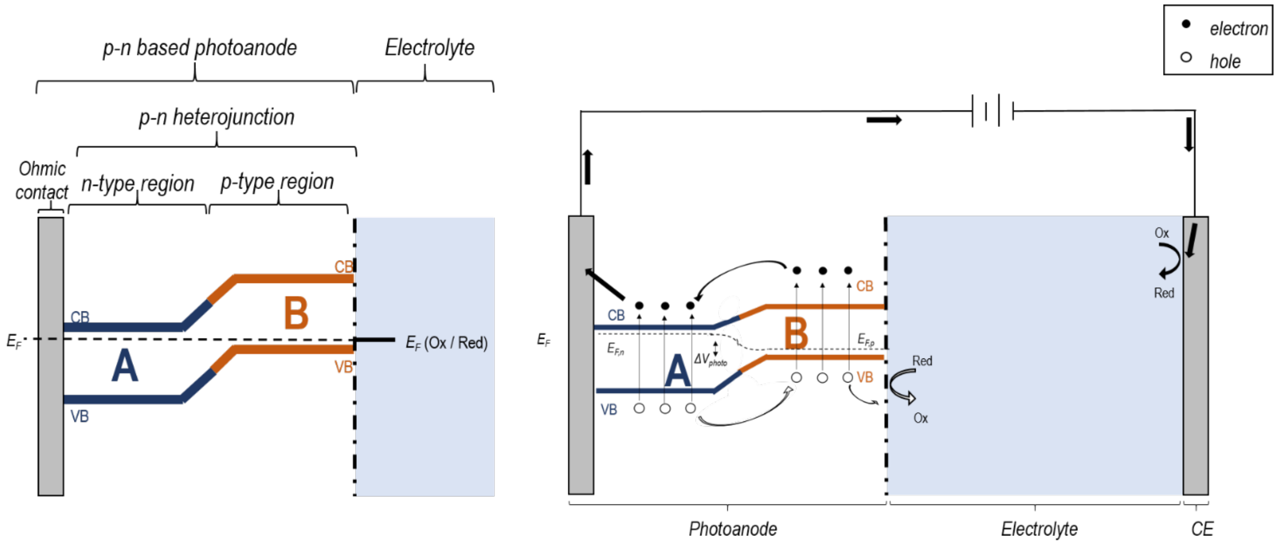

(I) **(II)**

Figure 3.8 - Schematic representation of a Ti/TiO$_2$/Cu$_2$O electrode in a PEC cell. A) electrode/electrolyte interface at the equilibrium; B) p-n photoanode under illumination.

Chapter 4

TiO_2-based electrocatalysts in Electrokinetic soil remediation

4 TiO_2-based electrocatalysts in Electrokinetic soil remediation

4.1 Electrokinetic technologies

Electrokinetic (EK) treatments are in-situ remediation processes employed in organic and/or inorganic contaminants removal from soils or other porous matrices (sewage sludge, fly ash, etc.), which exhibit a low permeability [115].

It consists of a direct current flow between two electrodes, placed in soils or porous matrixes, with the resulting electric field which promotes contaminants mobilization [116]. During the current flow transport phenomena like electromigration, electroosmosis and electrophoresis are involved (e.g. inorganic contaminants will be transported as ions through electromigration, while organic contaminants and uncharged inorganic species will be transported by electroosmosis towards the electrodes), with the current which act as "cleaning agent", while at the electrodes electrochemical reactions like electrolysis and electrodeposition take place [117].

Electrodialysis (ED) for soil remediation is a specific ex-situ Electrokinetic technology, developed for heavy metals removal from polluted soil, which combines the transport mechanisms involved during EK processes with the principle of electrodialysis [118]. ED systems are characterized by the presence of ionic exchange membranes, placed to separate the electrodic compartments from the treated soil matrix. This results in a three compartment (3C) cell (Figure 4.1), where cationic species move towards the cathode through a cation exchange membrane (CEM), while anions move towards the anode through an anion exchange membrane (AEM), so that their separation in concentrated solutions takes place [119], [120].

In addition to the transport mechanisms, considering the non-perfect selectivity of the AEM membrane respect to H^+ ions, some of them, during the current flow in the ED 3C cell, move towards the cathode implying the formation of an acidic front, which contributes to dissolve important amounts of contaminants from the soil [118], as well as the acidification and alkalization of anodic and cathodic compartments respectively takes place.

Unfortunately, the main factor which limits the real use of this technology in remediation treatments can be addressed to the energy costs related to the power supply and the stirring, with this latter which is a crucial factor in the contaminants mobilization [121].

A promising strategy to minimize the energy costs can be directly derived from the electrolysis reactions involved during the current flow. To minimize the overall ED treatment energy cost, the hydrogen evolved during the current flow can be recovered and stored or directly employed in a tandem Proton Exchange Membrane Fuel Cell (PEMFC) for in-situ energy production [122].

As reported from several authors among the available literature, ED remediation treatments are generally carried out employing commercial electrodes (metal and/or metal oxides based) [118], [123]–[125], while to our knowledge, it has not been reported yet the use of non-commercial high aspect ratio electrodes, like TiO_2 NTs based electrodes synthesized in this work. Besides that, the same literature analysis highlighted that ED cells employed are generally characterized by symmetric configurations, i.e. the same electrocatalyst for both anode and cathode, while it is well recognized that specific electrocatalyst for the oxidation and reduction reactions involved would be preferable. Even more considering that in reason of the AEM and CEM membranes the two electrodic compartments, during the current flow, undergo to operate in different pH ranges, and consequently the same electrocatalyst could result ineffective in one of the two compartments. These latter aspects would suggest the selection of specific electrocatalysts for each electrodic compartment (according to the reactions involved), in order to improve the overall process kinetic. Furthermore, respect to the Hydrogen production, a specific hydrogen evolution reaction (HER) electrocatalyst would mean an increase in hydrogen production rate which would contribute to minimize the overall process cost.

4.2 Electrodialytic cells in soil remediation

Electrodialytic (ED) processes for soil remediation are carried out in a three compartments (3C) cell (Figure 4.1), where the matrix to be treated is placed in the central compartment of the 3C cell, and is separated from anolyte and catholyte through ionic exchange membranes [123], as described in the previous section.

Electrodic materials employed are metals or metal oxides based commercial electrodes, generally in symmetric cell configuration (i.e. the same electrocatalyst for both anode and cathode).

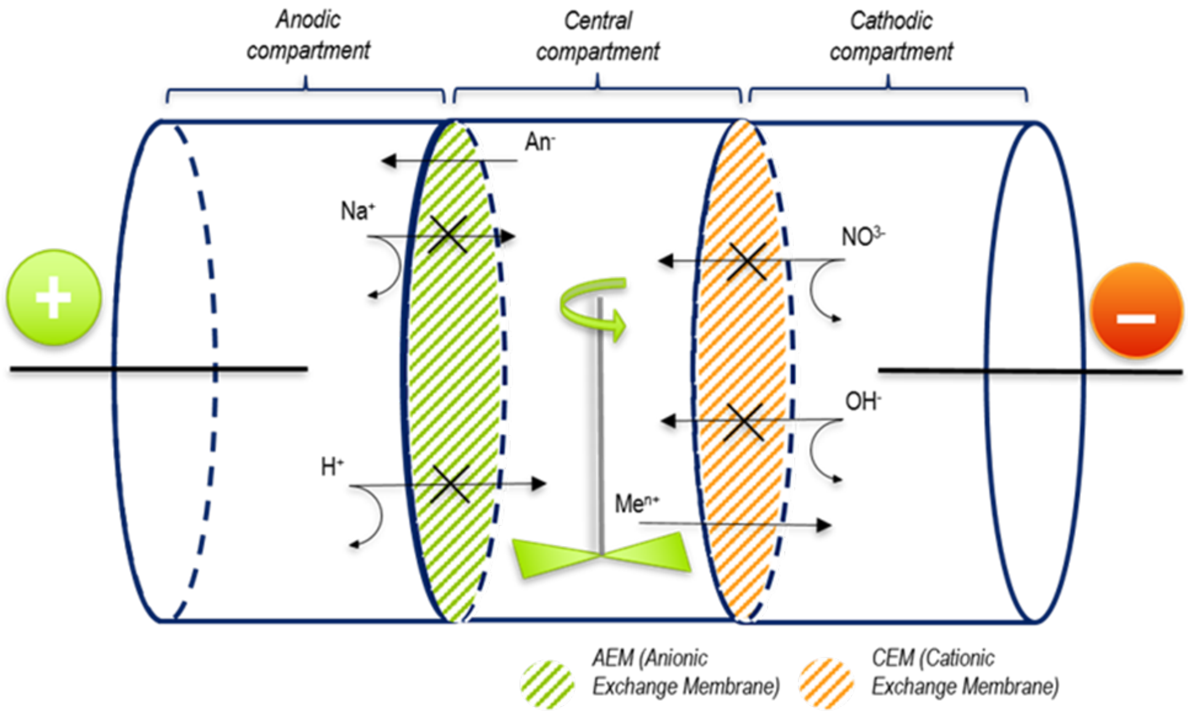

Figure 4.1 - Schematic representation of a 3C ED cell during current flow with $NaNO_3$ as both, anolyte and catholyte. It must to be highlighted that this representation doesn't take in account the non-ideal selectivity (< 100%) of the AEM membrane.

The main electrodic reactions involved during the current flow are the water electrolysis, at the anode:

$$2H_2O_{(l)} \rightleftharpoons O_{2(g)} + 4H^+ + 4e^- \tag{4.1}$$

while at the cathode:

$$2H^+ + 2e^- \rightleftharpoons H_{2(g)} \tag{4.2}$$

In 3C ED cell configuration, considering the presence of ionic exchange membranes, fast acidification and alkalization of anodic and cathodic compartments respectively occurs during the current flow [119], so that at the cathode reaction (4.2) is replaced by the water reduction reaction in alkaline medium:

$$2H_2O_{(l)} + 2e^- \rightleftharpoons H_{2(g)} + 2OH^- \tag{4.3}$$

Further reactions could be metals electrodeposition at the cathode, while in presence of chlorides at the anode chlorine gas evolution:

$$2Cl^{-} \rightleftharpoons Cl_{2(g)} + 2e^{-} \tag{4.4}$$

Considering that the real employment of such technology in soil remediation is mainly limited by the energy costs related to the stirring and power supply, a strategy to minimize that costs can be directly derived from the electrolysis. Respect to the process goal, oxygen (reaction 4.1) and hydrogen evolution (reaction 4.3) are secondary products. In this perspective the produced hydrogen would be a byproduct of great interest.

To better explain that strategy it is essential to take a step back. In conventional water electrolyzers crucial factors are the energy costs related to the overpotentials required to sustain the overall water splitting. This is why is, whenever possible, is preferable to operate under strongly acidic or alkaline conditions to minimize the overpotentials required. As consequence would be preferable that both electrocatalysts, for hydrogen evolution reaction (HER) and oxygen evolution reaction (OER), would operate in the same pH range. Unfortunately, considering also the costs related to the electrocatalysts, it should be taken into account that most of non-noble metal water splitting catalysts, could be highly active catalysts in acidic media nevertheless may be inactive or unstable in alkaline electrolytes, or vice versa [126], [127].

Connecting back to the strategy useful to minimize the costs related to ED technologies after this latter digression, should appear clear as the 3C cell configuration offers a great advantage respect conventional electrolyzers. Here in reason of the acidification and alkalization of the anodic and cathodic compartment respectively, which takes place during the current flow, the employment of different electrocatalysts that are most effective when operate in tandem in different pH ranges would be possible. In this way is possible to select electrocatalysts able to guarantee minimized costs related to the overpotentials and at the same time increased effectiveness in terms of produced hydrogen.

As consequence, in order to optimize the cost effectiveness of the overall ED technology, a first strategy would be to employ HER and OER electrocatalysts that could be most effective when operate in different pH range.

To date, the benchmark catalysts for OER are Ir/Ru-based compounds, while Pt-group metals are the most effective catalysts for HER [128]. The main limit to the widespread use of these electrodic materials is related to the high costs and low abundance of which are characterized. To answer this issue researcher efforts has been dedicated to the development of non-precious metal based and highly efficient electrocatalysts [129], [130]. Among them, nanostructured Titania based electrodes, like that synthesized in this work, are low cost water splitting catalysts [131]–[133], employed in electrolysis cells both, as HER [134]–[136] and OER electrocatalysts [137]–[139]. TiO_2 NTs based electrodes, besides to guarantee high surface to volume ratio, can be employed "alone" (i.e. electrodes composed by the bare TiO_2) or coupled with other metals (for HER) and/or metal oxides (for OER) which can improve the electrocatalytic activity.

An example of improved TiO_2 base HER electrocatalyst is the Black TiO_2. Authors report on improved performances due to the vacancy engineering achieved after the electrochemical reduction carried out for its transformation [140].

In addition, regard the TiO_2 NTs based electrodes synthesized in this work, these could be ad hoc modified with suitable metals or metal oxides through electrodeposition techniques, which would guarantee low costs and versatility.

Moreover, considering that one of the strategies suggested to minimize the overall ED process energy cost is based on the recovery of the evolved hydrogen, which would be employed in a tandem PEMFC (Proton Exchange Membrane Fuel Cell) for *in-situ* energy production [122], the development of a suitable most effective HER electrocatalyst would mean a further increase in hydrogen productivity and consequently in the costs effectiveness.

Aim of the work and outline

Aim of the work and outline

The aim of the present study has been the implementation of electrochemical synthesis strategies for nanostructured TiO_2 based photocatalysts and electrocatalysts production.

TiO_2 NTs synthesis is commonly carried by electrochemical anodization, following double-step processes with noble metal electrocatalysts as counter electrodes. In order to enhance the sustainability of the synthesis process, aim of the work at this stage has been the development of a novel "single-step" anodization method. This approach can allow reaching improved sustainability, guaranteeing two operation stages less than the conventional "double-step" processes, and avoiding, thanks to the symmetric cell scheme (i.e. use of titanium sheets as counter electrodes), the employment of noble metal electrocatalysts as counter electrodes.

One of the main difficulties addressed by this optimization study has been preventing the formation of an undesired nanograss at the top of nanotubes, due to the etching effect of the same electrolyte on the early stage formed oxide as a function of the anodization time. This situation doesn't allow having an accurate control on morphology and NTs length. Aim of the work, at this stage, has been thus the development of a post-treatment useful to guarantee improved control on top tubes morphology and consequently NTs length. At the same time, according to the anodization method developed which foresee the potentiodynamic behaviour of the cell voltage during the early stage of the process, to achieve reduced NTs length with an ordered free top tubes morphology, a further optimization of the experimental conditions has been performed.

Further electrochemical synthesis step, employing the synthesized NTs based electrodes, have been investigated according to the specific application showed.

In relation to the photocatalytic application, considering the limited light absorption characteristic of the titanium dioxide (only UV active; ~ 3% of the total sunlight radiation), one of the most implemented strategies to improve the TiO_2 light absorption, consist of the deposition of a suitable co-photocatalyst active in the visible region of the solar spectrum (~ 47% of the total sunlight radiation), as in the case of the Cu_2O electrodeposition. Electrodeposition techniques allow to effectively control sizes and morphology of Cu_2O nanoparticles which ultimately determine the activity of the synthesized electrode. According to this strategy, aim of the work at this stage has been the study of the Cu_2O electrodeposition onto TiO_2 NTs, evaluating the effect of the applied potential and electrodeposition time on sizes and morphology of the resulting Cu_2O NPs.

The photocatalytic tests performed employing the so synthesized electrodes, in contrast to the expectations and according to several previous studies, had evidenced as the TiO_2/Cu_2O electrodes exhibit photocatalytic performances in the UV + visible region lower as compared to the bare TiO_2 electrode. Consequently, at this stage the work has been devoted to the analysis of the mechanisms responsible for this unexpected performance. To this purpose, the influence of the morphology of the Cu_2O nanoparticles synthesized by electrodeposition and of the underlying TiO_2 nanotubes on the photocatalytic performances of the composite TiO_2/Cu_2O electrode has been evaluated. The results of this study have been exploited to develop a novel electrochemical post-treatment strategy of the composite electrodes, allowing to achieve improved photocatalytic performances in the UV + visible region as compared to the bare TiO_2 electrode.

A further electrochemical synthesis step has been investigated in the framework of the activities related to the *e.THROUGH* EU project (H2020-MSCA-RISE-2017-778045), aimed to the recovery of critical raw materials and sustainable soil remediation through electrokinetic (EK) technology, specifically, electrodialytic (ED) remediation. As reported in literature, ED processes are generally carried out in symmetric cell schemes, with commercial Ti/MMO (Mixed Metal Oxides; Ir-/Ru- based) electrodes for both anode and cathode. At the same time one of the proposed strategies to improve the sustainability of the process by cost minimization, foresee the hydrogen recovery as valuable byproduct. Consequently, to improve the effectiveness of this strategy, a specific cathodic HER electrocatalyst to boost the hydrogen production would be requested instead of Ti/MMO, which on the contrary is benchmark catalyst only for the anodic OER. Aim of the work at this stage has been thus the development of a specific HER electrocatalyst useful to increase the hydrogen production. To this purpose, a facile electrochemical reduction strategy, to synthesize “Black TiO_2” HER electrocatalysts starting from the amorphous TiO_2 resulting from the anodization has been followed.

Chapter 5

Materials and methods

5 Materials and methods

5.1 Electrodes synthesis

5.1.1 TiO_2 NTs synthesis through “single-step” anodization

The anodization processes are carried out in a two-electrodes jacketed cell, kept at room temperature (24.5 ± 0.5)°C and magnetically stirred. The two-electrodes are connected to a power supply (Aim-TTi CPX200DP DC Power Supply Dual Outputs, 2 x 60V/10A 180W) and are titanium planar electrodes (Alfa Aesar 99.5%, annealed, thickness 0.25mm), both the substrate to be anodized (anode) and the counter electrode (cathode). The electrolytes employed to carry out the process were Ethylene Glycol (Alfa Aesar, 99+%) based electrolytes, containing NH_4F (Alfa Aesar, 98% min.) and H_2O in different concentration ratios (Table 5.1).

Table 5.1 - NH_4F and H_2O Concentration Ratios in Different Ethylene Glycol Based Electrolytes

Electrolyte	**NH_4F [$\%_{wt}$]**	**H_2O [$\%_{v/v}$]**
EG1	0.1	0.5
EG2	0.1	1.0
EG3	0.1	2.0
EG4	0.3	0.5
EG5	0.3	1.0
EG6	0.3	2.0
EG7	0.3	6.0
EG8	0.3	10.0
EG9	0.3	15.0

Anodizations were carried out for different total durations, specified case by case in the discussion of the results in the next section.

Prior to anodization, the titanium electrodes were pretreated just by Acetone (VWR Prolabo Chemicals, 100%) in ultrasonic bath (Elma® S 10 Elmasonic, 220-240V∼, 30W, 50-60Hz), in order to degrease the electrodes surface.

The applied voltage (U) was imposed according two stages: a first linear growth (i.e. potentiodynamic anodization, equation 5.1) up to the anodization potential, reached which, it remains constant for different total anodization times (potentiostatic anodization). Following the potentiodynamic early stage regime equation:

$$U = k \cdot t_d \tag{5.1}$$

where U is the applied cell voltage during the potentiostatic anodization, k is the potential growth rate and t_d the duration of the potentiodynamic anodization.

Table 5.2 – Anodization methods (AM).

Method	$\boldsymbol{k}$ **[V/s]**	$\boldsymbol{U}$ **[V]**
AM1	0.5	20
AM2	0.5	40
AM3	0.5	60
AM4	0.05	60

5.1.2 Annealing treatment

Amorphous Titania resulting from anodization is thermally treated in a muffle furnace (Nabertherm B410, Tmax1100°C, 1.2KW), where the constant temperature of the specific treatment (T_A) is reached with a heating rate of 8°C min^{-1} (h). At the end of the treatment the samples were immediately cooled out of the furnace at ambient temperature. The experimental conditions of the different annealing treatment tested are summarized in Table 5.3.

Table 5.3 – Annealing methods (AN).

Method	h [°C/min]	T_A [°C]	t [min]
AN1	8.0	580	132.5
AN2	8.0	680	145.0
AN3	8.0	580	252.5
AN4	8.0	680	265.0

5.1.3 Cu_2O Electrodeposition for TiO_2 based photocatalyst synthesis

The electrodeposition tests were performed in a three electrodes jacketed cell, magnetically stirred and kept at room temperature. Ti/TiO_2 NTs electrodes annealed were employed as working electrode, a platinum gauze (Alfa Aesar 25 x 25 mm, 100 mesh woven from 0.0762 dia wire, 99.9% metal basis) was used as counter electrode, while an Hg/HgO as reference electrode. The applied potentials reported in the present study are instead all referred to Ag/AgCl saturated electrode. $CuSO_4 \cdot 5H_2O$ (Sigma Aldrich, ≥98%) reagent has been employed to prepare the electrolyte solution with Cu^{2+} content equal to 0.4 M in Lactic Acid 3.0 M (Alfa Aesar, ACS 85.0-90.0% aq. soln.). The pH of the solution has been successively adjusted to 11.0 by the addition of NaOH 5.0 M (Merck, ≥99.98%).

The electrodeposition tests were carried out with an IVIUMnSTAT potentiostat, following pulsed electrodeposition method based on the cyclic application of a first cathodic pulse (A period, t_{on}) followed by a zero-current time (B period, t_{off}), as reported in Table 5.4.

Table 5.4 - Pulsed Electrodeposition Methods (PED). E_A is the applied potential during the A period, t_{on} is the duration of the A period, I_B is the imposed current during the B period, t_{off} is the duration of the B period.

Method	E_A [V]	t_{on} [s]	I_B [mA]	t_{off} [s]
PED1	-0.6	0.5	0	5
PED2	-0.8	0.5	0	5
PED3	-0.9	0.5	0	5

In each test, the duration of the electrodeposition experiments was indirectly assigned fixing it in terms of overall transferred charge (Q), specified case by case in the discussion of the results in the next section.

5.2 Electrodes characterization

Morphological characterization of the electrodes was performed through a field emission scanning electron microscopy (FE-SEM Zeiss Auriga), equipped with an energy dispersive X-ray analyzer (EDX Bruker QUANTAX 123 eV) employed for the analysis of the elemental composition of the nanostructures. The software ImageJ was used to analyze FE-SEM images.

Optical properties of the semiconductor electrodes were investigated through Diffuse Reflectance Spectroscopy with a KONICA MINOLTA CM-2600d Spectrophotometer, in the wavelength range 360 - 740nm, and a SHIMADZU UV-2600 in the range 300 - 700nm.

A further DRS spectrophotometer (SHIMADZU UV-2450) was used for Black TiO_2 characterization during the experiments carried out at NOVA University of Lisbon in the wavelength range 360 – 700nm.

X-ray diffractometer (Bruker D8 ADVANCE) with a Molybdenum anode ($K\alpha$ = 0.71Å) was employed for the crystal phases identification, for Ti/TiO_2 electrodes before and after annealing treatment and for $Ti/TiO_2/Cu_2O$ electrodes. The diffractometer has a Bragg-Brentano focusing geometry which makes it suitable for thin films analysis using a reflection configuration. The experimental peak assignments were given by comparison to Crystallography Open Database references.

The surface atomic composition of the obtained samples was analyzed by X-ray Photoelectron Spectroscopy (XPS), using a modified Omicron NanoTechnology MXPS system. Experimental spectra were theoretically reconstructed by fitting the peaks to symmetric Voigt functions and the background to a Shirley or a linear function. XPS atomic ratios ($\sim$10% associated error) between relevant core lines were estimated from experimentally determined area ratios corrected for the corresponding theoretical cross sections and for a square root dependence of the photoelectrons kinetic energies. All the samples were mounted on a magnetic stainless steel tips with a conductive adhesive tape. The fit procedure has been optimized and peak assignments were given by reference to previous literature references.

5.2.1 Electrochemical characterizations

Prior to the electrodeposition tests a linear sweep voltammetry (LSV) in the electrodeposition solution was performed, employing the thermal treated Ti/TiO_2 electrodes as working electrodes in the same electrodeposition cell described above. The experiments were carried out starting from an applied potential of 0.0 V toward the cathodic range up to -1.2 V at a scan rate of 50mV/s.

To evaluate the electrode/electrolyte interfaces of the electrodes employed in ED experiments (Section 3.5), an Electrochemical impedance spectroscopy (EIS) study was performed. EIS analysis were carried out in a three-electrodes cell with TiO_2-based electrodes as working electrodes, Ag/AgCl as reference electrode and a Pt spiral wire as counter electrode, while the electrolyte employed was $NaNO_3$ 0.01 M (Carlo Erba Reagent, $\geq$ 99,5%). All the tests were performed with an IVIUMnSTAT potentiostat equipped with a frequency response analyser, set to AC amplitude voltage of 10 mV in a frequency range included between 10 kHz and 0.01 Hz.

The resulting Nyquist plots were then analysed through the IVIUM equivalent circuit analyser software based on a NLLS-fit for the equivalent circuit parameters estimation.

5.2.2 Photoelectrochemical characterization. Pulsed light LSV (PL-LSV)

The Ti/TiO_2/Cu_2O electrodes synthesized for photocatalytic applications were further characterized through linear sweep voltammetry performed under pulsed light irradiation (PL-LSV). This technique is commonly employed to define the photocurrent response of the analysed photoelectrodes as function of the potential range investigated.

Pulsed light LSV were performed in the potential range between -1.5 and 1.5 V employing Na_2SO_4 0,01M (Merck, ≥ 99.0%) as electrolyte, $Ti/TiO_2/Cu_2O$ electrodes as working electrodes, Pt spiral wire as counter electrode and Ag/AgCl as reference, with a scan rate of 10 mV s^{-1}.

The experiments were carried out in a "black box" (self-made, Figure 5.1) to guarantee no external light sources interferences and to prevent the operator exposure to direct UV light.

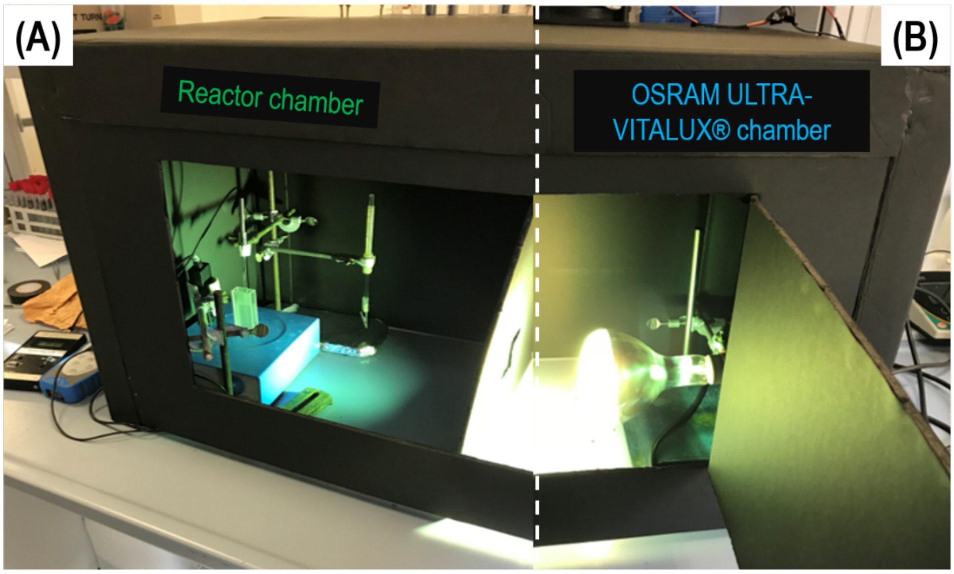

Figure 5.1 – Two chambers "Black box" employed in PL-LSV and photodegradation experiments: A) reactor chamber and B) light source (OSRAM ULTRA-VITALUX®) chamber.

The light source (OSRAM Ultra Vitalux 300W) was a sunlight-simulation lamp (Figure 5.2).

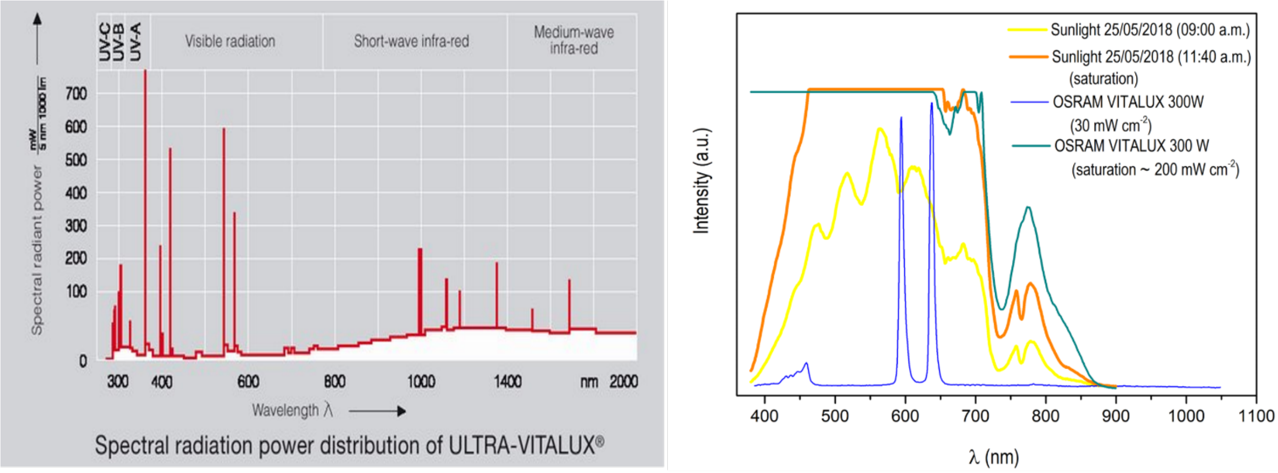

(A) **(B)**

Figure 5.2 – A) OSRAM ULTRA-VITALUX® Spectral radiation and power distribution reported in the technical datasheet of the producer. B) Experimental emission spectra collected under solar radiation (yellow and orange lines) and employing OSRAM ULTRA-VITALUX® (blue and green lines). The experimental spectra were collected through a portable spectrophotometer (SpectroVis® Plus Spectrophotometer, Vernier).

PL-LSV characterizations were carried out under an incident light power density of 100 mW cm^{-2}, characterized through a luxmeter (Gossen Mavolux digital).

The dark to light cycle was guaranteed by a mechanical shutter (self-made, Figure 5.3) directly controlled by the digital output of the potentiostat employed during the LSV analysis. The frequency of the shutter was set to 0,66 Hz.


(A) (B)

Figure 5.1 – "Black box" reactor chamber equipped with the mechanical shutter: A) Shutter opened, reactor chamber in dark conditions; and B) Shutter closed, reactor chamber under irradiation.

5.3 Photocatalytic tests

Photocatalytic activity was evaluated employing the synthesized electrodes as supported photocatalysts (i.e. titanium substrate act as supporting substrate instead as current collector in photoelectrochemical cells) in a quartz cuvette photochemical cell magnetically stirred. Photo-degradation experiments were carried out through the degradation of an organic dye, employing methylene blue (MB) (Alpha Aesar, 1%w/v) as degradation target. The experiments were carried out immersing the supported photocatalyst in 10 mL of MB solution with an initial concentration of 6.25 mg/L.

The mixture was first stirred for 30 minutes in the dark at room temperature to ensure that the adsorption equilibrium was reached. Then the photochemical was illuminated with a sunlight-simulation lamp (OSRAM Ultra Vitalux 300W) with an incident light density of 100 mW cm^{-2}, characterized with a luxmeter (Gossen Mavolux digital). The experimental apparatus was contained in a “black box” to ensure that no external light source would perturb the experiments.

Furthermore, the light source chamber (Figure 5.1, B) has been equipped with an air cooling system (Figure 5.4, B), useful to prevent the uncontrolled temperature increase due to the power of the light source employed (i.e. 300 W), in the reactor employed during the photodegradation tests (Figure 5.4, A).

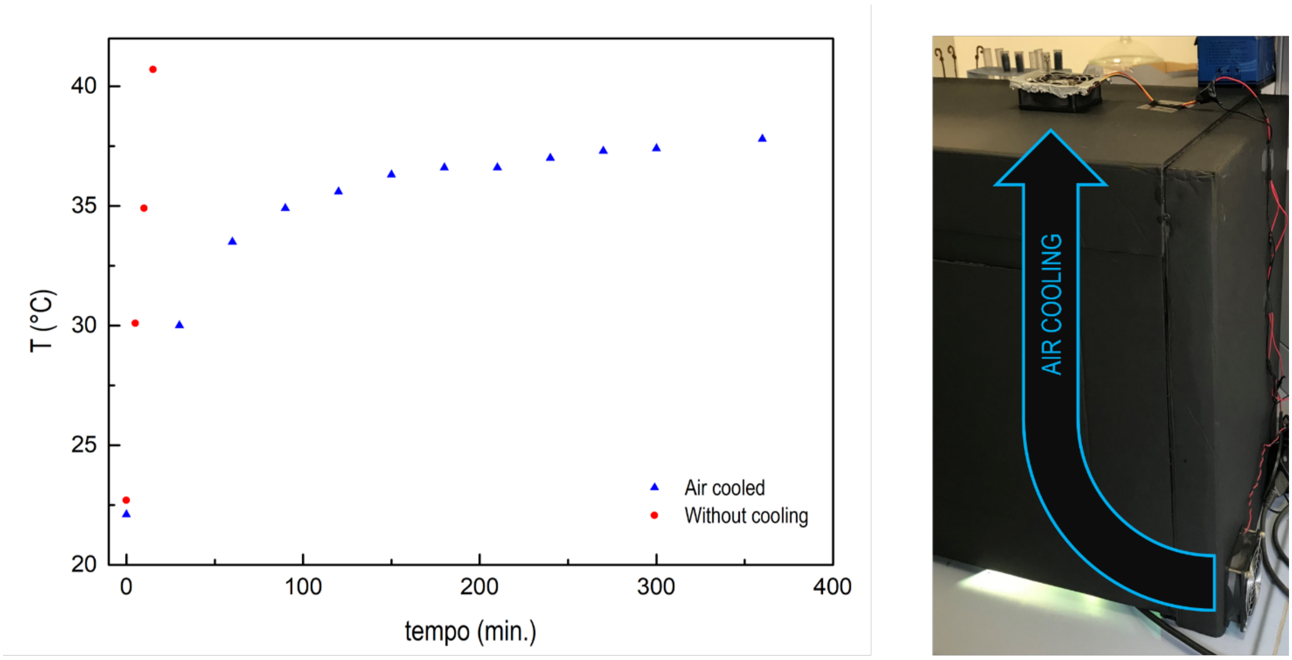

(A) **(B)**

Figure 5.2 – A) Temperature behavior in the photocatalytic reactor during the irradiation employing the OSRAM ULTRA-VITALUX ® light source: without cooling system (red dots) and in presence of the air cooling system (blue triangles). B) External view of the light source chamber of the “Black box” equipped with the air cooling system.

MB solution samples were collected at fixed time intervals to evaluate the concentration variations through UV–vis spectroscopy (Varian Cary 50 Scan spectrophotometer). The self-degradation of methylene blue under the same conditions of the photo-degradation experiments was also evaluated. A calibration curve (not shown here) of MB solution was obtained at 664.1 nm wavelength at different concentrations prepared.

5.4 Photoelectrochemical tests

Photoelectrochemical measurements were performed in a three electrodes jacketed cell (24.5 ± 0.05) °C, with electrolytic solution containing 0.01 M Na_2SO_4 under simulated sun-light irradiation (ASAHI SPECTRA HAL-320, 300 W Xe lamp, built in AM1.5G solar simulation filter), with an incident light density of 100 $mW \cdot cm^{-2}$, characterized with a luxmeter (Gossen Mavolux digital).

The synthesized photoelectrode, both the bare Ti/TiO_2 and $Ti/TiO_2/Cu_2O$, were alternatively tested as working electrodes (WE) in a three electrodes photoelectrochemical cell, with a platinum spiral wire as counter electrode (CE) and Ag/AgCl as reference electrode (RE). The photogenerated current was evaluated connecting the described photoelectrochemical cell to a potentiostat (SOLARTRON 1287 Potentiostat).

To evaluate the photogenerated current the cell was maintained at open circuit potential (OCP), measured in dark conditions, then the illumination was provided. Short duration photocurrent tests were carried out according to a pulsed light method, alternating cyclically light to dark conditions for fixed time intervals (30s). The tests carried out under only visible light irradiation were realized with the same solar simulator above mentioned equipped with an UV cut off filter ($\lambda < 400$nm).

5.5 Electrodialytic tests

The experiments were carried out at CENSE laboratories of NOVA University of Lisbon in a three compartment electrodialytic cell developed by CENSE researchers (Figure 5.5).

In this cell configuration anionic and cationic exchange membranes (Ionics: AEM-AR204 SZRA B02249C; CEM-CR67 HUY N12116B) are placed to separate the central compartment by the anodic and cathodic sides respectively. The cell was made of Plexiglas with an internal diameter of 8 cm, each compartment is characterized by a length of 5cm.

Anolyte and catholyte employed in all the ED tests described below were both $NaNO_3$ 0.01 M (Carlo Erba Reagent, $\geq$ 99,5%), 250.0 mL for each compartment. The same for the constant current flow that was fixed in all the ED experiments at a current density of 21,2 mA · cm^{-2}. The electrodes were placed at a distance of 12,5 cm and connected to a power supply (Hewlett Packard E3612A, Palo Alto, USA).

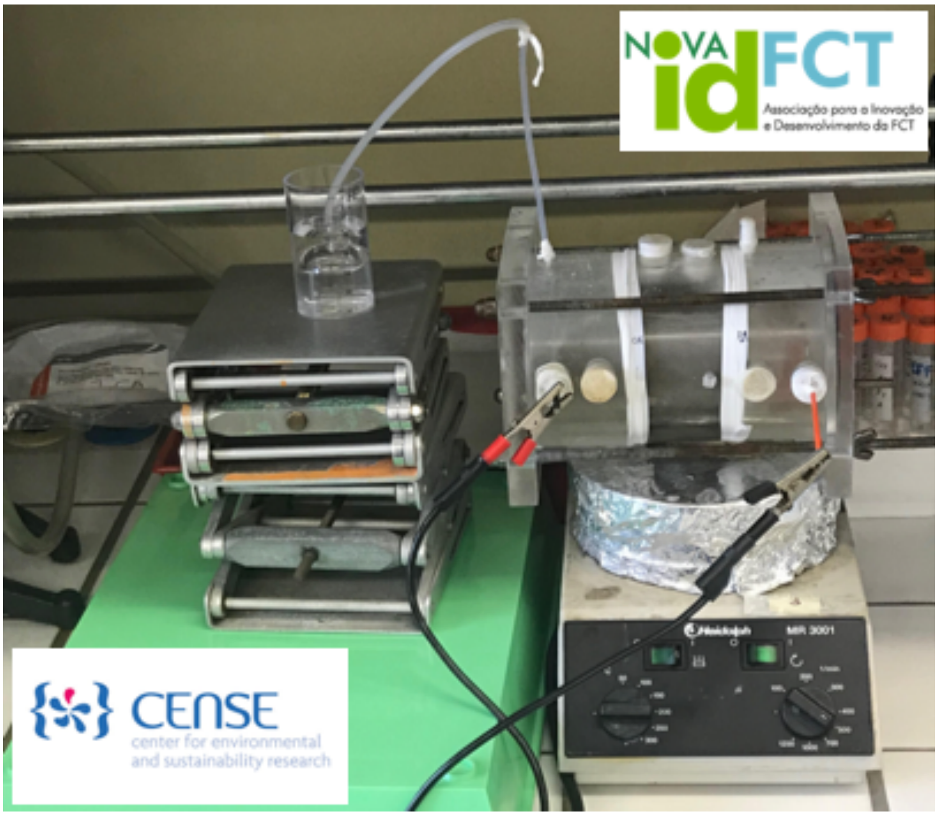

Figure 5.5 – Electrodialytic cell employed during ED remediation treatments. In this configuration the cathodic compartment is connected to a volumetric variation indicator employed for H_2 production rate estimation (beaker on the left of the picture connected to the ED cell on the right).

Commercial Ti/MMO rods (Titanium/Mixed Metal Oxides; 0.50 cm length; 0.03 cm dia.) were employed as anodes in all the ED cells configurations tested (Table 5.5).

Table 5.5 - ED cell configurations tested

3C ED cell configuration	Electrodes	
	Anode	Cathode
S	Ti/MMO	Ti/MMO
A	Ti/MMO	Anatase TiO_2
B	Ti/MMO	Black TiO_2

The cathodic materials tested were non-commercial TiO_2 based electrodes and commercial Ti/MMO rods.

TiO_2 based electrodes employed were synthesized following the anodization method AM4 (Table 5.2) in EG7 electrolyte (Table 5.1) for 27 min. Anatase TiO_2 were achieved after the annealing (AN1, Table 5.3) of the so synthesized electrodes, while Black TiO_2 were synthesized through an electrochemical post-treatment carried out at the end of the anodization and described below. The TiO_2 electrode resulting from the anodization were then employed as cathode in a two electrodes electrochemical cell, connected to a power supply (Aim-TTi CPX200DP DC Power Supply Dual Outputs, 2 x 60V/10A 180W), with a Ti sheet (Alfa Aesar 99.5%, annealed, thickness 0.25 mm) as anode in $NaNO_3$ 0,01 M (Carlo Erba Reagent, ≥ 99,5%), at a constant current density of 20,0 mA $\cdot$ cm^{-2} for 30 minutes.

In Electrodialytic water splitting experiments the central compartment was filled with tap water and 0,3 g of NaCl (Merck, Reag. Ph Eur). The experiments duration was fixed at 20 min and the experiments were carried out in two replicates. The H_2 production rate was evaluated connecting a volumetric variation indicator to the cathodic compartment, measuring the volume variation as function of time during the current flow. This set of experiments was carried out testing all the ED cell configuration reported in Table 5.5.

In soil remediation experiments Panasqueira mine residues from Covilhã, Portugal, named in the text as MTAW (Mine Tailings As W), 22,2 g of MTAW were dissolved in tap water, with a solid to liquid ratio of 1:9, and 11,0 g of NaCl were added. The duration of the experiments was set to 120 hours (5 days) and was performed in two replicates, both in configuration S and configuration B (Table 5.5).

At the end of each experiment liquid samples of the three compartments, named ANOLYTE, CATHOLYTE and LIQUID PHASE MTAW, were collected from the anodic, cathodic and central compartment of the ED cell respectively (data showed in Figure 6.47). The AEM and CEM membranes as well as the Ti/MMO anodes were leached in HNO_3 1,0 M (Panreac, Reag. Ph Eur) for 24 hours, at the end of which a liquid sample of the relative leach liquor was collected and named LEACH LIQUOR AEM, LEACH LIQUOR CEM and LEACH LIQUOR ANODE respectively (data showed in Figure 6.47). The MTAW was first filtered and then dried for 24 hours, after that was dissolved in 12 ml of aqua regia with a solid to liquid ratio of 1:24. After 48 hours on a skating table, a liquid sample was collected and named SOLID PHASE MTAW (data showed in Figure 6.47).

Total concentrations of As, Cu, Sn, and W, were determined by Inductively Coupled Plasma with Optical Emission Spectrometry (ICP-OES) (HORIBA Jobin-Yvon Ultima, Japan), equipped with generator RF (40.68 MHz), monochromator Czerny-Turner with 1.00 m (sequential), automatic sampler AS500 and dispositive CMA-Concomitant Metals Analyser.

Chapter 6

Results and discussions

6 Results and discussions

6.1 “Single-step” Anodization: Structural and Morphological Properties of the Ti/TiO_2 Electrodes

Anodization processes are generally carried out in two electrodes asymmetric cells, where the substrate to treat is titanium (anode), while the counter electrode is a noble metal catalyst with high aspect ratio (cathode), like Pt mesh. In this work the anodizations were carried out in symmetric cells where, both the substrate to anodize and the counter electrode are titanium sheets. With this configuration, a “double step” anodization method, is generally performed to synthesize an ordered array of TiO_2 nanotubes.

In this work a “one-step” anodization method was optimized to generate ordered arrays of TiO_2 nanotubes. The method includes the progressive and controlled variation of cell voltage during the early anodization stage (potentiodynamic control) followed by a period of anodization under constant cell voltage (potentiostatic control). Further, the anodizations were carried out in symmetric cells where both the anode and the cathode were titanium sheets, thus excluding the application of the costly Pt counter electrode.

Considering the possible applications of the electrode to synthesize, it must be taken into account that in many electrochemical reactions such as OER and HER, the electrolyte diffusion can be tuned by tailoring the pore size of the porous materials. In detail, Macroporous nanostructures (i.e. pore diameters > 50 nm) would provide facile transfer and diffusion of reactants and products in the reaction over the electrodes [39].

According to that, and taking into account that the tuning of the anodization parameters is a crucial factor for the resulting structural and morphological properties of the TiO_2 NTs array [26], [55], a first set of anodization experiments was carried out in order to evaluate the relationship between the experimental parameters (i.e. cell voltage, fluoride and water contents in the electrolyte and anodization time), and NTs characteristics (i.e. inner tube diameters and nanotubes length).

It is well known that the growth dynamics of the TiO_2 NT arrays are mainly dictated by the cell voltage (hereafter also referred to as potential) and the electrolyte composition, specifically in terms of fluoride content [49], [50].

The relation between pore diameters (d) and applied potential (U) in porous anodic oxides, is described through the following general equation [24], [141]:

$$d = k \cdot U \tag{6.1}$$

with k as growth factor of the specific porous anodic oxide. Lu and Jiao estimated for TiO_2 $k \approx$ 1.3 - 3.3 nm V^{-1} depending on the employed electrolyte [72].

TiO_2 NTs, unlike other porous oxides, are characterized by a nanotubular architecture instead of the porous honeycomb matrix. As consequence, NTs would be characterized by two different diameters (i.e. inner and outer).

While it can be assumed that in the close packed NTs array, outer diameters are barely exposed to the electrolyte, resulting mainly function of the applied potential [24], [50], it must be taken into account that inner tube diameters, on the contrary, are directly exposed to the electrolyte and are thus largely influenced by the fluoride etching effect of the same electrolyte on the formed oxide [49], (Equation 2.6).

It is worth underlined once more that inner tube diameters ultimately control the diffusion of the electrolyte species into the nanotubes and contribute to determine the specific surface of the TiO_2 array [39]. These would be aspects of interest for both, photocatalytic and electrocatalytic applications.

The first set of experiments was carried out in order to evaluate the relationship between outer NTs diameters and applied potentials. Anodization tests were performed maintaining constant the duration of anodization and the electrolyte composition (EG5, Table 5.1), while were varied the potential values imposed during the potentiostatic period, and equal to 20, 40 and 60 V (AM1, AM2 and AM3; Table 5.2). Otherwise, in order to evaluate the effect of the electrolyte composition on the inner tube diameters, anodization tests were then separately performed maintaining constant potential equal to 60 V (AM3, Table 5.2) and anodization time equal to 122 min while was varied the ratio between water and NH4F in the electrolyte (electrolyte compositions EG1-EG6, Table 5.1).

The results of the anodization tests performed with constant electrolyte composition by varying the potential are reported in Figure 6.1.

Cross sectional FE-SEM images of the TiO_2 nanotube arrays are displayed at the top of Figure 6.1, evidencing that the outer nanotube diameter and the nanotube length increases with increasing the anodization potential, while the derived outer diameters distributions are report at the bottom of the same figure.

The evolution of the mean outer diameters shows an increment as the potential is growing, with a comparable growth factor (k, equation 6.1), falling in the range 1.3 - 3.3 nm V^{-1}, which is in agreement with the findings previously reported by Lu and Jiao mentioned above.

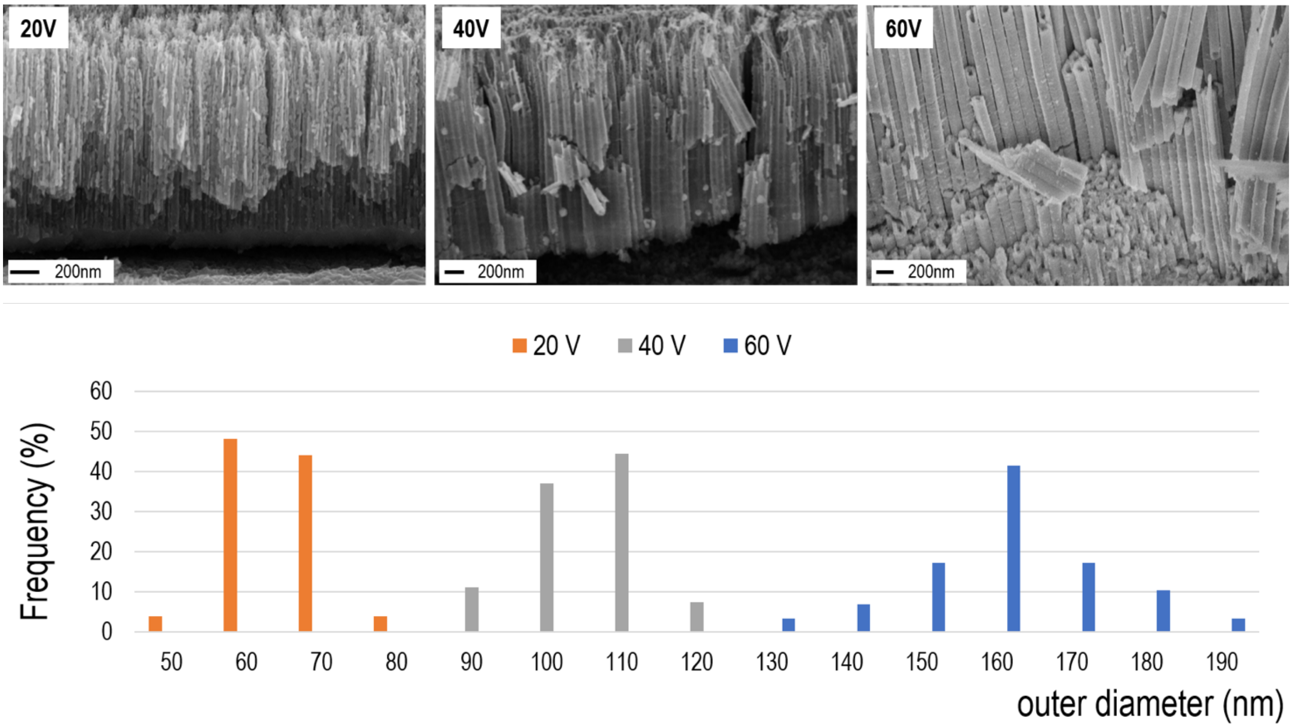

Figure 6.1 – FE-SEM images, cross sectional view of Ti/TiO_2 electrodes anodized for 32min in EG5 electrolyte at 20V, 40V and 60V and related outer diameter frequency distribution.

The results of the tests performed by varying the electrolyte composition are reported in Figures 6.2 and 6.3. Top-view and cross-sectional SEM images of the synthesized TiO_2 nanotube arrays are reported in Figure 6.2, while the evolution with water and NH_4F content in the electrolyte of the mean inner and outer nanotube diameter, as computed by the analysis of SEM images, is reported in Figure 6.3.

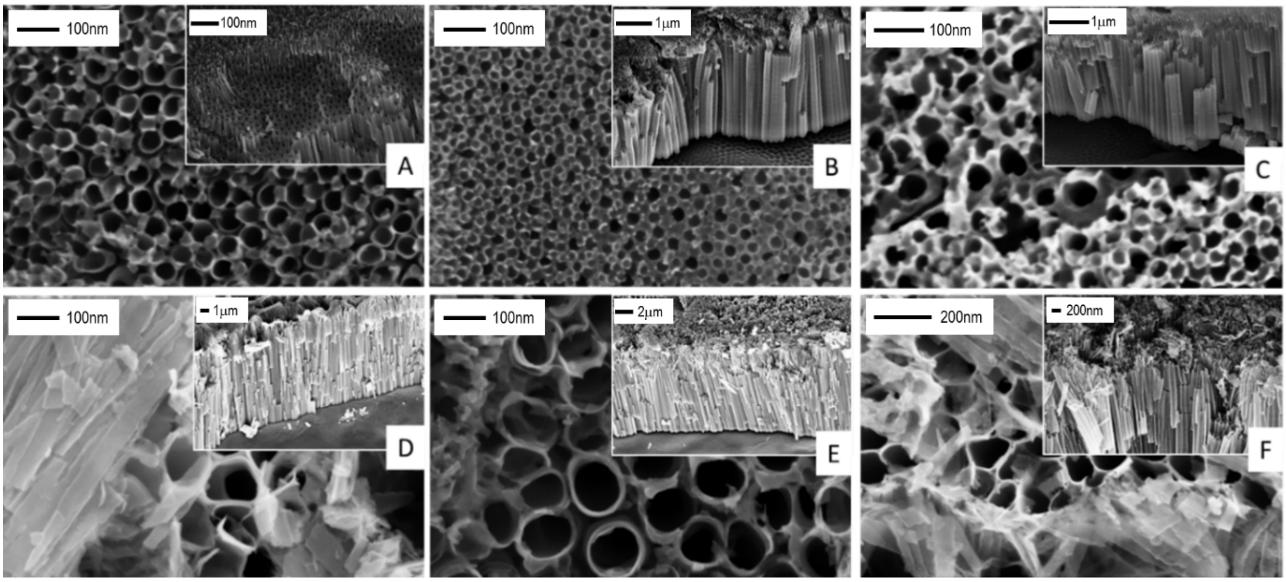

Figure 6.2 – FE-SEM images, Ti/TiO_2 electrodes anodized for 122 min at 60V in different electrolytes: A) EG1, $0.1\%_{wt}$ NH_4F – $0.5\%_{v/v}$ H_2O; B) EG2, $0.1\%_{wt}$ NH_4F – $1.0\%_{v/v}$ H_2O; C) EG3, $0.1\%_{wt}$ NH_4F – $2.0\%_{v/v}$ H_2O; D) EG4, $0.3\%_{wt}$ NH_4F –$0.5\%_{v/v}$ H_2O; E) EG5, $0.3\%_{wt}$ NH_4F – $1.0\%_{v/v}$ H_2O; F) EG6, $0.3\%_{wt}$ NH_4F – $2.0\%_{v/v}$ H_2O. The FE-SEM images insets show the corresponding cross-sectional views.

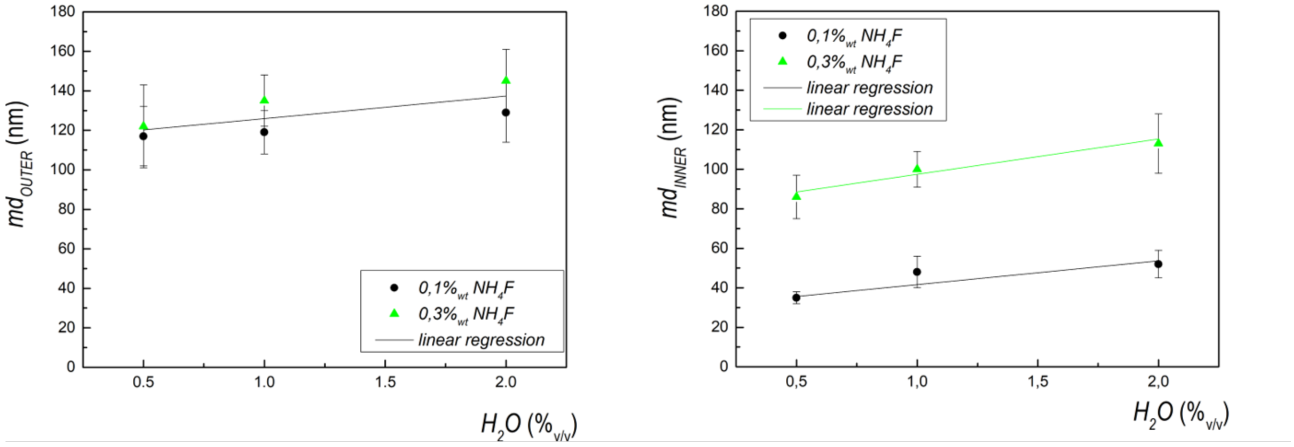

(A) **(B)**

Figure 6.3 - Mean diameter as a function of electrolyte concentration ratios. A) Outer tubes diameter (md_{OUTER}); B) Inner tubes diameter (md_{INNER}). In both diagrams the black circles correspond to $0.1\%_{wt}$ NH_4F while the green triangle to $0.3\%_{wt}$ NH_4F.

As it is apparent from Figure 6.3, no significantly statistical difference was found (statistical significance $p < 0.05\%$) between the mean outer diameters attained with the two selected NH_4F contents (Figure 6.3, A), while statistically different inner diameters were found (Figure 6.3, B). Particularly, the mean inner diameter varies from about 30 - 60 nm to 70 - 130 nm by modifying the NH_4F percentage from 0.1 to 0.3 %, respectively (Table 6.1). This confirms that the outer diameter is mainly influenced by the applied anodization potential, while the inner diameter is affected mainly by the electrolyte composition.

Table 6.1 - Effect of the Electrolyte Concentration Ratios on tubes diameter. md is the mean diameter and s the relative standard deviation.

Electrolyte	md_{OUTER} [nm]	s [nm]	md_{INNER} [nm]	s [nm]
EG1	122	21	35	3
EG2	135	13	48	8
EG3	145	16	52	7
EG4	117	15	86	11
EG5	119	11	100	9
EG6	129	15	113	15

The influence of the electrolyte composition on the mean inner diameter can be explained by the etching of TiO_2 by the fluorides in the electrolyte [26]. Specifically, increasing fluoride content increases the etching rate ultimately determining, in agreement with data reported (Figure 6.3, B; Table 6.1), larger inner tube diameters. This is confirmed by the data reported in Figures. 6.1 and 6.3. These data evidence that the mean outer diameter varied from about 160 nm, attained at 60 V with the EG5 electrolyte and 32 min of anodization (Figure 6.1), to about 120 nm attained under the same anodization conditions but 122 min of anodization (Figure 6.3, A). This result can be explained by observing that the top of the tubes is constantly in contact with the electrolyte, though most of the outer tube surface is not wet by the electrolyte. This determines the progressive thinning of the outer diameter at the top of the TiO_2 nanotube array during the anodization. The decrease in outer diameters as function of the anodization time corresponds to the “V-shaped” sidewall thickness profiles characteristic of TiO_2 NTs synthesized in fluoride based electrolytes [52].

In order to further characterize the mechanisms governing the growth dynamics of the TiO_2 nanotubes, the evolution of the nanotube length with the anodization time at 60 V and 0.3% NH_4F is shown in Figure 6.4.

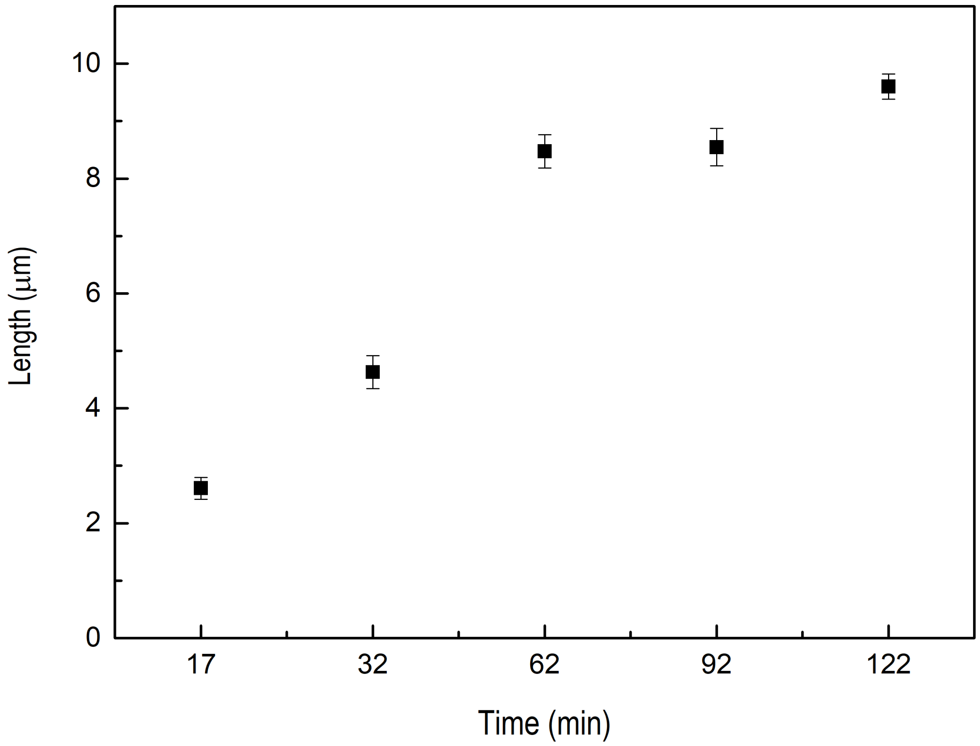

Figure 6.4 – NTs length of samples anodized in EG5 electrolyte at 60V for different durations (17min, 32min, 62min, 92min, 122min).

The nanotube length monotonically increases with the anodization time, an almost constant growth rate around 0.13 µm min^{-1} attained during the initial anodization hour. The growth rate is then decreased to about 0.01 µm min^{-1} and it remains up to two hours. This variation in the nanotube growth rate is determined by the interplay between oxide growth rate at the bottom of the nanotube, the etching reaction taking place at the TiO_2 nanotube internal surface and the diffusion of fluoride ions. Fluorides are transported by diffusion through the nanotubes simultaneously etching the TiO_2 generated by titanium anodization. Therefore, the concentration of the fluoride ions, and thus the etching rate, is larger at the top than at the bottom of the nanotubes.

Owing to the progressive thinning, nanotube sections closer to the top surface eventually collapse, which determines, in agreement with data reported in Figure 6.4, a reduction in the nanotube growth rate, confirming once more the V-shaped profile of the NTs cross section [52]. The progressive thinning of the top tube walls leads to the formation of a disordered layer which covers the underlying nanotubes, commonly named *nanograss* (Figure 6.5, A).

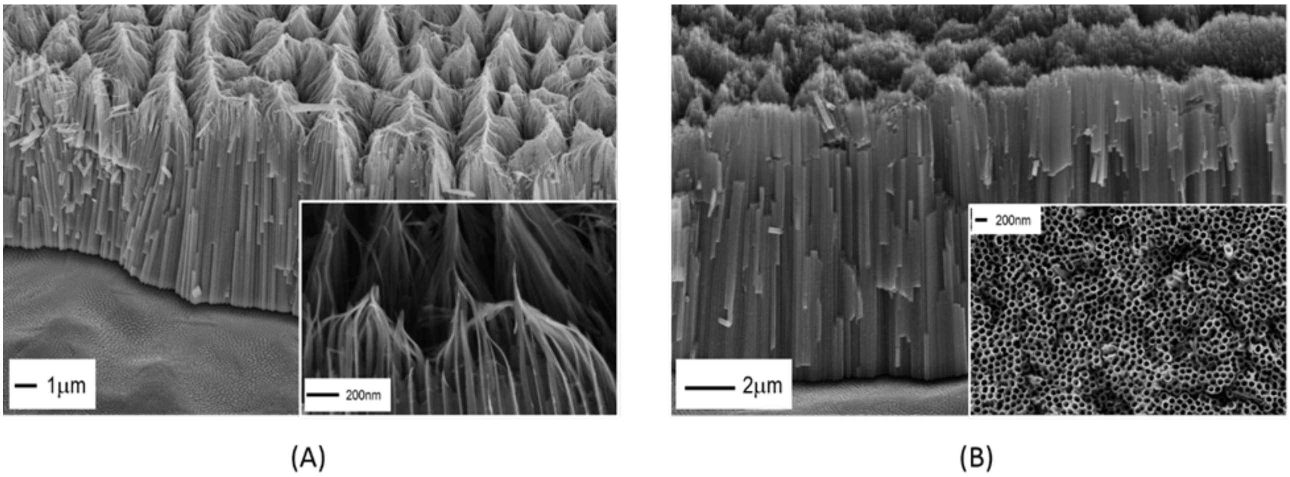

Figure 6.5 – FE-SEM images. A) Cross sectional view, nano-grass layer on sample anodized in EG5 electrolyte at 60 V (AM3); the inlet is a magnification of top tubes. B) Cross sectional view, free nano-grass morphology in sample anodized in EG5 electrolyte at 60 V (AM3) after sonication post-treatment; the inlet is a top view of the same sample.

Nanograss formation can negatively affect the performances of the TiO_2 NTs array in electrocatalytic applications by increasing the resistance to the transfer of reactants and products through the underlying nanotubes. On the other hand, the illustrated experimental analysis unequivocally demonstrates that nanograss formation can hardly be prevented if arrays nanotubes with length of the order of several μm are produced.

In order to produce NTs with length ≈ 10 μm, hereafter referred as “Long NTs”, with a free nano-grass top tube morphology, a post-treatment of the electrodes produced by one-step anodization was developed. To this purpose, electrodes obtained with EG5 electrolyte at 60 V and 62 min of anodization time were employed. The optimized post-treatment included: washing with acetone, drying 24 h and sonication in a water bath at ambient temperature for 20 minutes. The effect of the developed post-treatment is clearly illustrated by Figure 6.5. Here, FE-SEM images of NTs electrodes with length around 10 μm after anodization (Figure 6.5, A) and after the post-treatment (Figure 6.5, B) are reported. The comparison evidences the ability of the post-treatment to remove the nanograss formed during anodization.

On the other hand, depending on the targeted application, the synthesis of considerably shorter nanotubes may be needed. The synthesis of NTs arrays with length between 200 nm and 2 μm by one-step anodization was then evaluated.

Major obstacle to produce these TiO_2 nanotubes, according to the one-step anodization method (AM3, Table 5.2), is represented by the formation during the early stage of the anodization, of a tree-like oxide layer characterized by a large polydispersity of the diameter distribution (see the scheme reported in Figure 2.2, B - potentiodynamic period). This layer is a protective "mask" for the underneath NTs growth and is progressively dissolved during the anodization by the etching of the electrolyte. However, if a nanotube length around 2 µm is targeted, the anodization time must be decreased, according with the growth rate derived from data displayed in Figure 6.4. The reduced anodization time may cause the impossibility to attain the dissolution of the tree-like oxide layer.

This was verified by repeating the anodization with the EG5 electrolyte and 60 V potential and decreasing the anodization time to 17 min. FE-SEM images of the electrodes produced by this anodization are reported in Figure 6.6. As compared to the electrodes produced with the same electrolyte and potential, but longer anodization time as in Figure 6.5, an oxide layer with heterogeneous porous structure is extending over the ordered NTs array as clear also seeing to the FE-SEM cross sectional view in the insert of Figure 6.6.

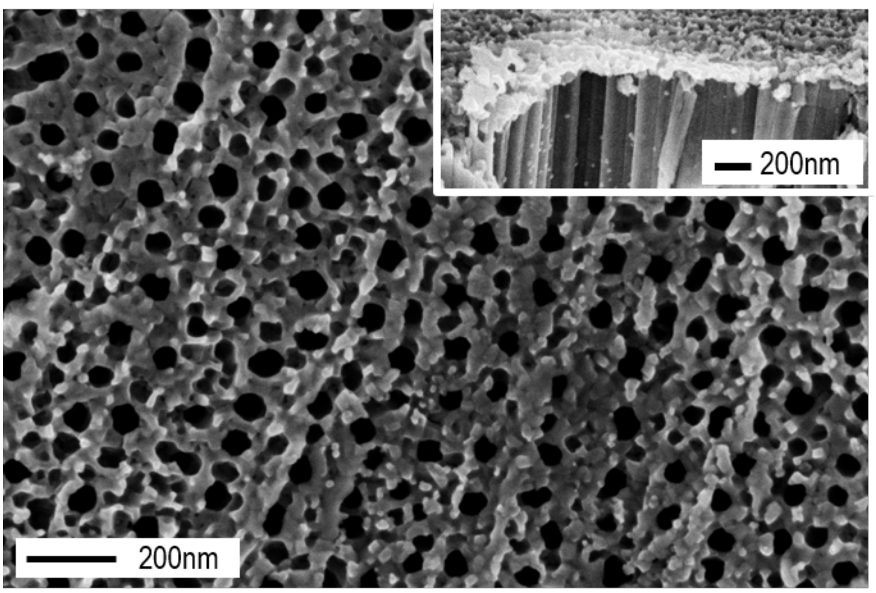

Figure 6.6 – FE-SEM image. Top view of a sample anodized in EG5 electrolyte (anodization method AM3) for 17 min. The insert represents a detail of the top tubes cross sectional view.

Therefore, in order to produce nanotubes with length between 200 nm and 2 µm and ensure dissolution of the tree-like oxide layer, a modification of the anodization conditions is needed.

The time needed to attain the complete dissolution of the tree-like oxide layer can be decreased by increasing the percentages of water and fluoride in the electrolyte. However, while this may allow attaining the dissolution of the tree-like oxide layer within shorter anodization time, it may simultaneously increase the growth rate and the disorder of the underlying nanotube structure. In order to overcome this limitation, an optimization was performed by increasing the concentration of water in the electrolyte, which allows faster dissolution of the tree-like oxide layer, and decreasing, at the same time, the growth rate of the potential during the early anodization period. Decreasing the potential growth rate decreases the average voltage applied during the potentiodynamic anodization period, thus preventing the increase in the growth rate and disorder of the underlying nanotubes that would be determined by the increased water content.

Figure 6.7 shows mesoporous “short” NTs (i.e. inner diameter > 50 nm; NTs length < 2 μm) produced by increasing the electrolyte water content (6 %v/v) and decreasing the potential growth rate to 0,05 V s^{-1} (i.e. anodization method AM4, Table 5.2). These NTs will be referred hereafter to as “short NTs”.

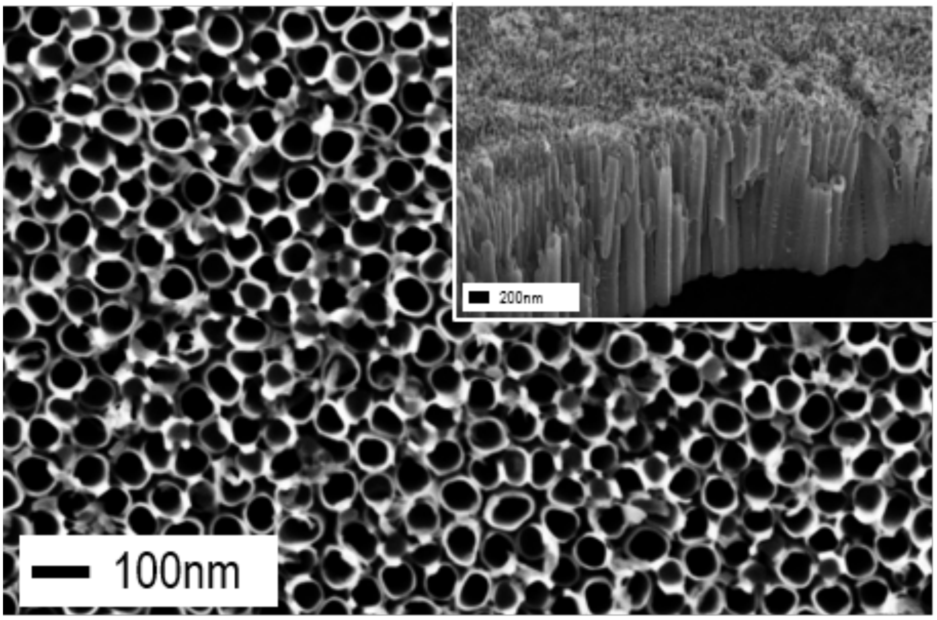

Figure 6.7 – FE-SEM image. "Short" NTS synthesized in EG7 electrolyte for 27min following anodization method AM4. The insert is the corresponding cross sectional view.

Further increase in water content (> 6 %v/v) exceedingly increased the etching rate and thus the disorder of the nanostructure (Figure 6.8, A and B), while a higher potential growth rate during the early anodization period did not allow to attain the dissolution of the tree-like layer (Figure 6.8, C).

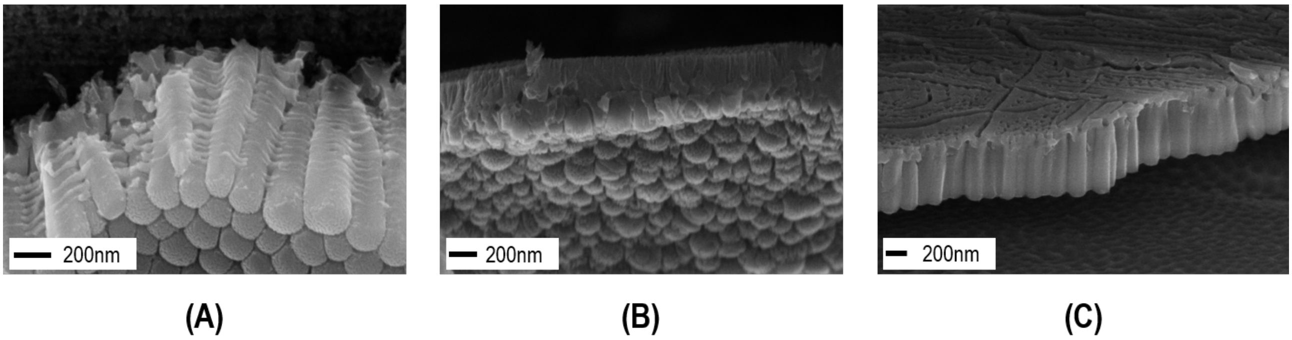

Figure 6.8 – FE-SEM image. A) NTs synthesized in EG8 electrolyte (10 %v/v water content), following anodization method AM3 for 17 min; B) NTs synthesized in EG9 electrolyte (15 %v/v water content) following anodization method AM3 for 17 min; C) NTs synthesized in EG7 electrolyte (6 %v/v water content) following anodization method AM3 for 9 min.

Among the electrodes synthesized during the tests above mentioned, two types of were selected for the rest of this study, which were synthesized by the optimized one-step anodization strategies described in Table 6.2.

Table 6.2 – Electrodes employed in this work after optimization of the anodization parameters.

Type	EG	AM	k [V s^{-1}]	U [V]	Overall anodization time [min]
"Long NTs"	EG5	AM3	0.5	60	62
"Short NTs"	EG7	AM4	0.05	60	27

6.2 Effect of the Annealing Treatment on the Ratio of the Crystal Phases

The TiO_2 NTs electrodes produced by the electrochemical anodization have amorphous structure. Therefore, thermal annealing was optimized to induce TiO_2 crystallization. Particularly, the influence of the thermal annealing parameters (e.g. duration, temperature) on the ratio of the two TiO_2 crystal phases, Rutile and Anatase, was analyzed.

Thermal annealing experiments were performed employing "Long" TiO_2 NTs (Table 6.2), under conditions described in Table 5.3. The samples were characterized through XRD analysis (Figure 6.9).

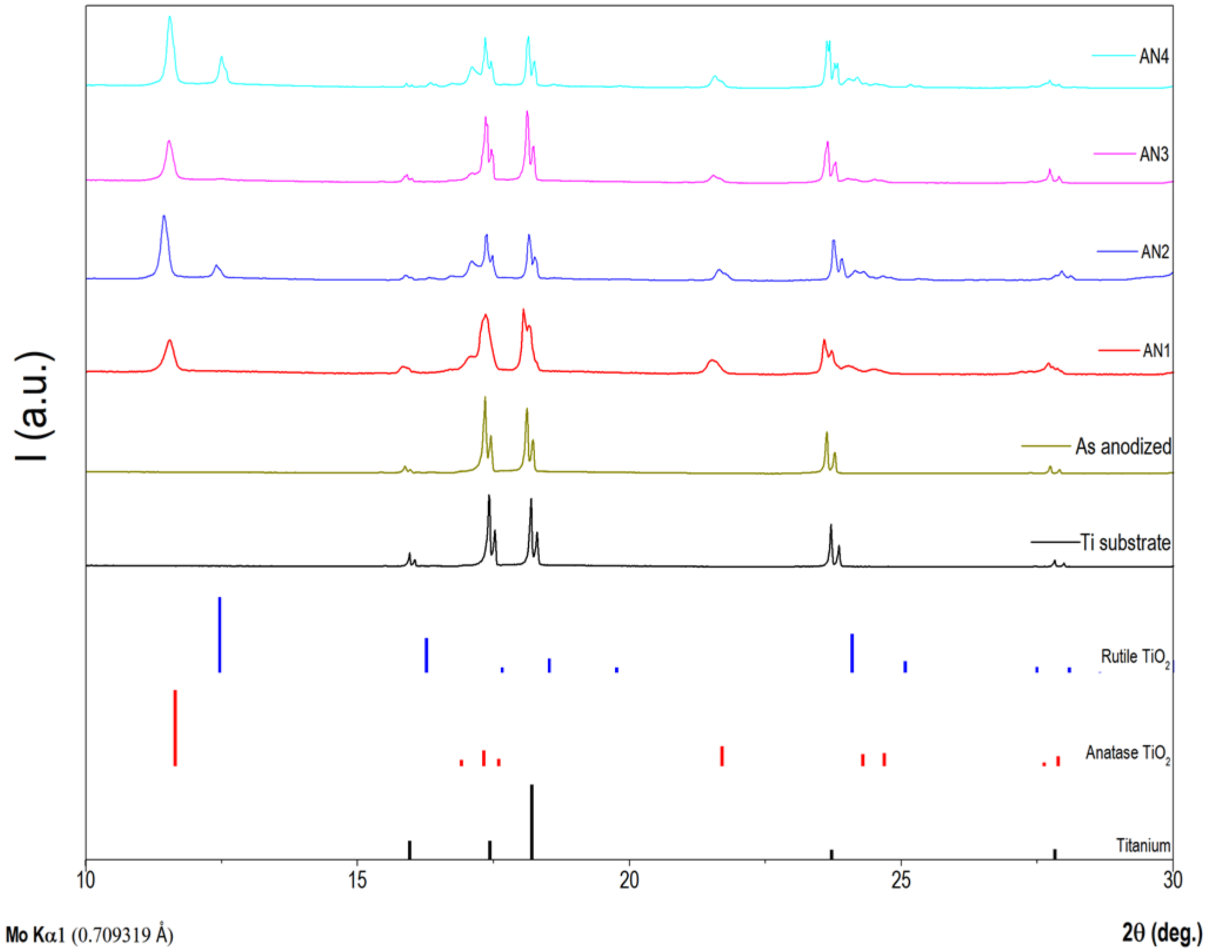

Figure 6.9 - XRD experimental spectra: Titanium electrode prior to anodization (black line); Ti/TiO_2 electrode after anodization (red line); Ti/TiO_2 electrode after annealing treatment AN3 performed at 580°C for 3 h (blue line); Ti/TiO_2 electrode after annealing treatment AN4 performed at 680°C for 3 h (green line). The bars at the bottom of the diagram are crystallographic database peaks related to Titanium (black bars); Anatase (red bars) and Rutile (blue bars) used for comparison with experimental spectra.

The Rutile/Anatase ratio was determined according to the method described by Ding et al. [142]:

$$\%Rutile = \frac{1}{\left[1+0.8\cdot\left({I_A}/{I_R}\right)\right]}\cdot 100 \qquad (6.2)$$

where I_A and I_R are the integrated intensity of Anatase (011) and Rutile (101), which are located at about 2θ = 11.5° and 2θ = 12.5°, respectively.

The diffractograms of the electrodes treated in the tests performed are reported in Figure 6.9, while the derived intensities of Anatase (I_A) and Rutile (I_R) ratio computed by Equation 6.2

are reported in Table 6.3. Rutile percentage increases with the temperature and duration of the treatment. Further, increasing the duration of the treatment increases the main peak intensities, which evidences an increase in the relative abundance of the two crystal phases.

Table 6.6 - Effect of Annealing treatment on the crystal phases Ratios.

Method	**I_A**	**I_R**	**I_A/I_R**	**%Rutile**
AN1	5795	---	---	---
AN2	23078	4990	4.6	21.3
AN3	24412	873	28.0	4.3
AN4	48833	19883	2.4	33.7

The percentage of rutile in the electrodes produced by the treatment AN1, as showed in Table 6.3 could not be estimated because of the negligible intensity of the (101) rutile peak. Therefore, it is possible to assume that, with the treatment AN1, the formed crystal phase is almost exclusively Anatase (%Rutile < 5 %).

Since Anatase is the most photoactive phase [143], the treatment AN1, unless otherwise specified, was then implemented to prepare the electrodes employed in the rest of the study related to the photocatalytic applications, for both Long and Short NTs.

6.3 Cu_2O Electrodeposition on Ti/TiO_2 Electrodes

$Ti/TiO_2/Cu_2O$ composite electrodes were produced by the electrodeposition of Cu_2O nanoparticles onto the surface of the TiO_2 NTs. In what follows, the mechanisms of Cu_2O nanoparticle formation are discussed by analyzing the results of the electrodeposition performed with the Long TiO_2 NTs (Table 6.2) thermally treated (AN1, Table 5.3).

Electrodeposition was performed by using a $CuSO_4$ solution containing lactic acid at pH values greater than 9. The alkaline pH is required to ensure the existence of a potential range characterized by thermodynamic stability of the solid Cu_2O phase, while the lactic acid ensures the formation of complexes with copper ions, thus preventing the precipitation of copper hydroxide [111], [112].

In order to evaluate the potential values effectively sustaining the electrodeposition of Cu_2O over Ti/TiO_2 electrodes, a linear sweep voltammetry (LSV) was initially performed with the employed electrolyte solution. The potential was varied from 0 to -1.2 V (Vs. Ag/AgCl) with a scan rate of 10 mV s^{-1}. The evolution of the recorded current with the potential is reported in Figure 6.10, A.

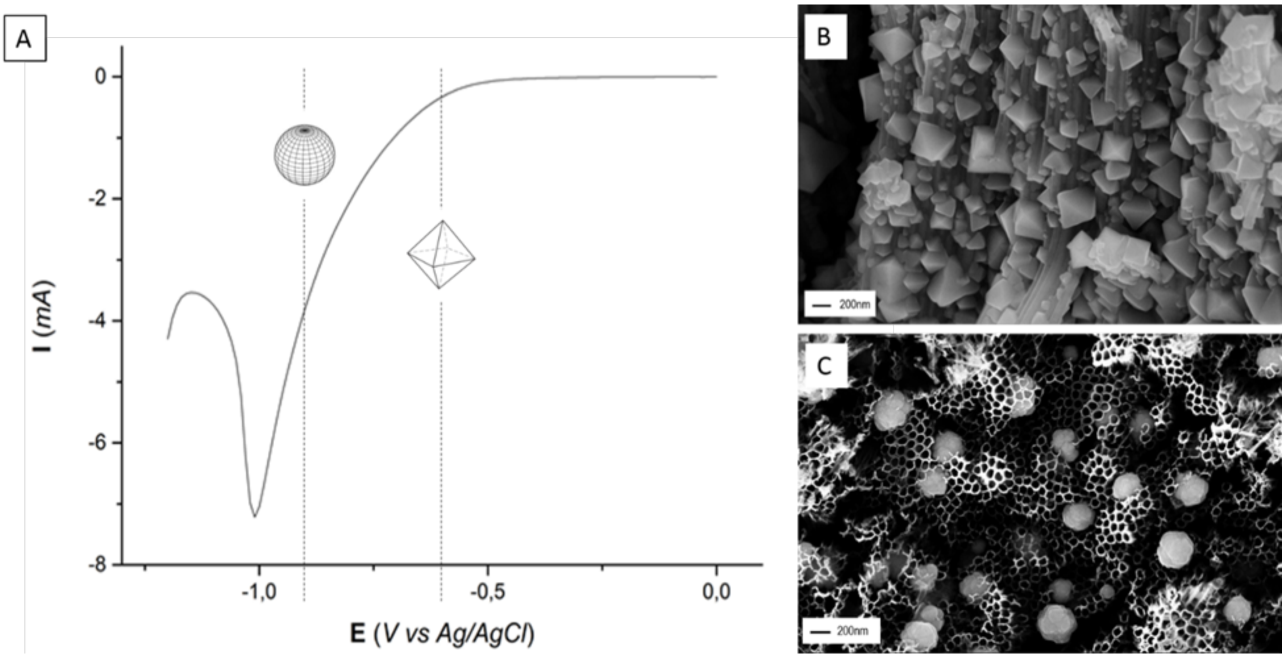

Figure 6.10 - A) Linear sweep voltammetry in electrodeposition solution ($CuSO_4$ 0.4M, Lactic Acid 3M, pH 11 - that concentrations are referred to the electrolyte before adjusting pH), scan rate 10 mV/s, employing Ti/TiO_2 Electrode as working electrode; B) FE-SEM images PED1, 120 0mC of transferred charge (cross sectional view); C) FE-SEM images PED3, 1200 mC of transferred charge (top view).

A non-negligible cathodic current is observed starting from -0.4 V, which marks the onset of copper ion reduction. A cathodic peak is successively attained at about -1.0 V following which the cathodic current progressively decreases. The cathodic current peak can be attributed to the establishment of a mass transfer electrodeposition regime. Under this condition, the characteristic time of copper ion reduction is much lower than the diffusion characteristic time and thus the cathodic current is only determined by the diffusion of copper ions to electrode surface. An increase in the cathodic current is successively detected at potential lower than -1.2 V, which can be attributed to water reduction. It is worth noticing that water reduction can decrease the faradaic efficiency of copper ion reduction, which can considerably lengthen the duration of the electrodeposition experiments that is required to attain a prescribed size of the Cu_2O nanoparticles.

The reported LSV evidences that copper ion reduction over TiO_2 nanotubes can be performed while maintaining a negligible water reduction by the application of potential values between -0.4 and -1 V. However, it is important to notice that the LSV cannot confirm that copper ions are exclusively reduced to Cu_2O over this potential range. Owing to the absence of separate cathodic peaks, which may be attributed to the two different reduction processes, a gradual transition to the formation of metallic copper could be attained by the application of increasing cathodic potential values (i.e. decreasing the negative potential).

In order to investigate the effect of the potential on morphology and crystal structure of the deposits, electrodeposition tests were performed by implementing the pulsed electrodeposition method illustrated in the previous chapter (see section 5.1.3), investigating cathodic potential values ranging between -1 and -0.4 V (Table 5.4).

A comparison between the morphologies of the deposits obtained at the different electrodeposition potentials is reported in Figure 6.10. The FE-SEM images of the deposits generated at -0.6 V (PED1, Figure 6.10, A) and -0.9 V (PED3, Figure 6.10, B) evidence that a morphological transition from octahedral to spherical Cu_2O NPs is observed, moving from less cathodic (PED1) to more cathodic (PED3) electrodeposition potential, respectively. FE-SEM images which clarify the effect of the transferred charge are reported in Figures 6.11 and 6.12. At any potential, increasing the transferred charge increases the size of the Cu_2O NPs (Figure 6.11 and 6.12).

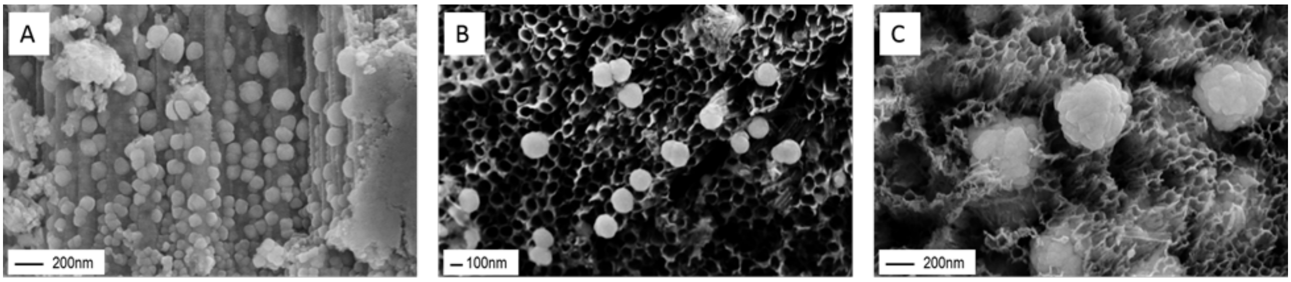

Figure 6.11 – FE-SEM images. PED3: A) 100mC (cross sectional view); B) 400mC (top view); C) 1200mC (top view).

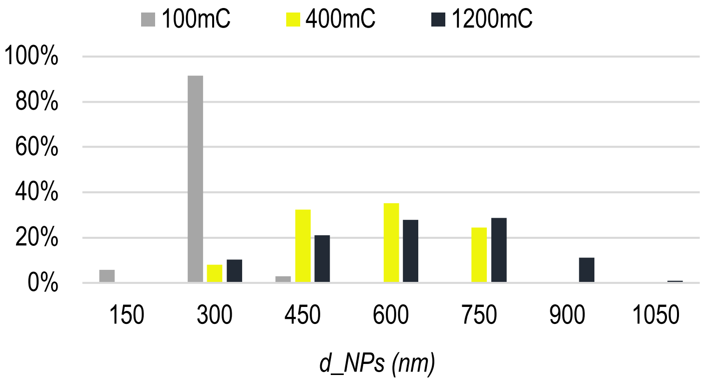

Figure 6.12 – Frequency distribution of the apparent diameter (d_NPs) estimated for the same samples reported in Figure 6.11.

The synthesized electrodes were characterized through XRD analysis, and the resulting spectra have been compared with the bare Ti/TiO_2 electrode annealed (AN1). All the composite electrodes show the appearance of new peaks which can be attributed to Cu_2O NPs and no significant differences have been found between the composite electrodes synthetized varying the applied potential (Figure 6.13).

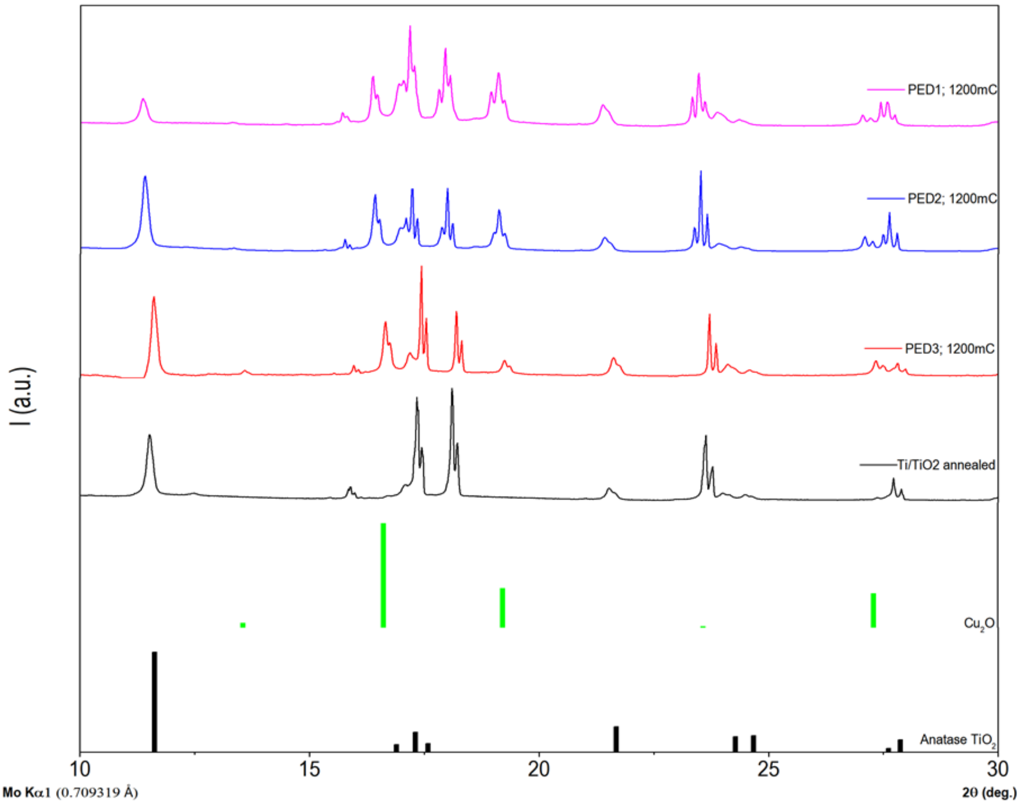

Figure 6.13 – XRD experimental spectra of the composite Ti/TiO_2/Cu_2O Electrodes: PED1, 1200 mC of transferred charge (blue line); PED2, 1200 mC of transferred charge (green line); PED3, 1200 mC of transferred charge (red line). The black line is the XRD pattern of Ti/TiO_2 electrode annealed (AN3). The bars at the bottom of the diagram are crystallographic database peaks related to Anatase (black bars), and Cu_2O (green bars) used for comparison with experimental spectra.

In accordance with the reported results, it can be concluded that copper ion reduction proceeds towards the formation of Cu_2O nanoparticles over the selected potential range.

The illustrated electrodeposition tests were repeated by employing “Short” nanotubes. As compared to the experiments with Long nanotubes, the overall transferred charge was decreased to leave almost unchanged the ratio between the transferred charge and the surface of nanotubes. With this approach, qualitatively comparable results were obtained confirming the morphological transition from octahedral to spherical electrodeposited particles with increasing the cathodic potential, and the formation of Cu_2O nanoparticles.

This indicates that the increased mass transfer resistance induced by increasing the length of nanotubes did not significantly influence the deposition process. It is conjectured that the absence of such an effect could be attributed to the implementation of the pulsed electrodeposition method. With this method, the cathodic potential sustaining electrodeposition is applied over very short time interval following which a potential preventing electrodeposition is applied which allows restoring the concentration of copper ions inside the nanotubes. Therefore, the absence of significant differences between the morphology and the surface density of the particles produced with long and short NTs can be attributed to the ability of this method to prevent the occurrence of an electrodeposition regime governed by diffusion.

6.4 Optical Characterization of the Electrodes

As in the electrodeposition tests, the optical characterization was performed on both series of synthesized electrodes, Long and Short NTs. Although here are showed the characterizations performed on Short NTs series, the same considerations reported below can be representative of the Long NTs series too.

Diffuse Reflectance Spectroscopy (DRS) was employed as characterization technique for the definition of the optical properties of the semiconductor-based electrodes and, particularly, to estimate the energy band gap (E_g). The result of the analysis is a Reflectance spectrum as function of wavelength (Figure 6.14, A), which can be converted into an equivalent absorption spectrum (Figure 6.14, B) through the Kubelka-Munk function. According to the Kubelka-Munk (K-M) theory, reflectance can be converted into the equivalent absorption coefficient (α) [110], [144], as follows:

$$F(R_\infty) = \frac{(1-R_\infty)^2}{2R_\infty} = \frac{k(\lambda)}{S(\lambda)} \sim \alpha \tag{6.3}$$

where $F(R_\infty)$ is the so called K–M function with $R_\infty = R_{sample}/R_{standard}$, $k(\lambda)$ is the absorption coefficient and $S(\lambda)$ is the scattering coefficient for the measured sample [145]. In equation 6.3, assuming the scattering coefficient wavelength independent the K-M function ($F(R_\infty)$) would be approximately proportional to the absorption coefficient (α).

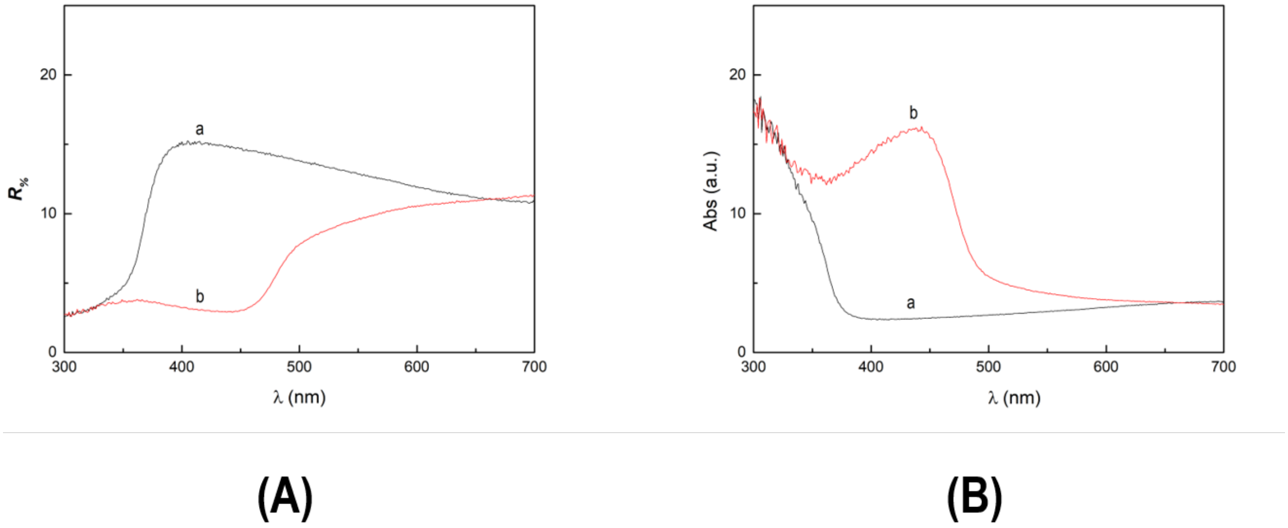

Figure 6.14 – Examples of DRS spectra: A) Reflectance spectra achieved for Short Ti/TiO$_2$ annealed electrode (a, black line) and Short Ti/TiO$_2$/Cu$_2$O electrode (b, red line); B) Equivalent absorption spectra achieved for Short Ti/TiO$_2$ annealed electrode (a, black line) and Short Ti/TiO$_2$/Cu$_2$O electrode (b, red line).

The band gap estimation starting from DRS measurements has been performed by two different methods.

The first and simpler method, according to Radecka et al. [146], can be applied directly to the Reflectance curve, plotting its first derivative ($dR/d\lambda$) as function of the wavelength (λ), (red dots, Figure 6.15 A). The optical band gap is calculated substituting the wavelength corresponding to the maximum point of the differential reflectance curve in the following equation:

$$E_g = \frac{hc}{\lambda} \tag{6.4}$$

where h is the Plank's constant and c is the speed of light.

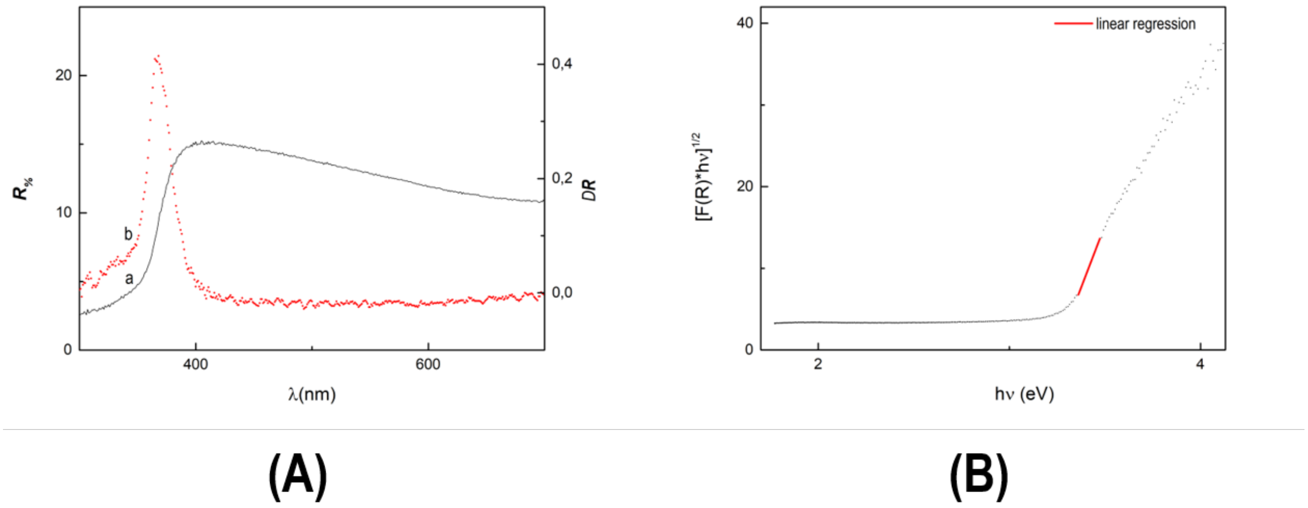

Figure 6.15 - Energy band gap estimation starting from DRS spectra: A) Radecka method. Short Ti/TiO₂ annealed electrode Reflectance spectrum (a, black line) and its 1st derivative (b, red dots); B) Transformed equivalent absorption product ($[F(R_\infty)\cdot h\nu]^{1/n}$) for n = 1/2 (black dots) and straight intercept with energy axes (red line), obtained for the same Short Ti/TiO₂ annealed electrode.

The Tauc plot method is the other and more extensively implemented estimation method [147]. It assumes that the absorption coefficient (α) is related to the energy band gap (E_g) by the following equation:

$$\alpha h\nu = A\left(h\nu - E_g\right)^n \tag{6.5}$$

where A is a proportionality constant and n is a power index related to the electronical transition, which may assumes the values 1/2 or 3/2 for direct electronic transition, allowed and forbidden respectively; and 2 or 3 for indirect electronic transition, allowed and forbidden respectively [93]. In the case of equivalent absorption derived from DRS measurements, substituting equation 6.3 into equation 6.5 gives:

$$[F(R_\infty) \cdot h\nu]^{1/n} = A\left(h\nu - E_g\right) \tag{6.6}$$

The application of the method then proceeds by the construction of a plot reporting the absorption product ($[F(R_\infty) \cdot h\nu]^{1/n}$) versus the photon energy $h\nu$. The energy band gap is estimated extrapolating the intercept between the linear part of the plot and the photon energy axis (Figure 6.15, B).

As reported from Wang et al., it is well established that bulk Cu_2O has a direct allowed band gap (i.e. optical Eg) of 2.62 eV [100]. In Table 6.4 the energy band gaps estimated for Cu_2O in composite $Ti/TiO_2/Cu_2O$ and the bare TiO_2 annealed (AN1) electrodes are summarized.

Table 6.4 - Energy band gap estimation. $E_{g,R}$ energy band gap estimated through Radecka method; $E_{g,T}$ energy band gap estimated through Tauc plot method for n = 1/2 (direct allowed band gap), with s the relatives standard deviations. All the electrodes employed for the analysis are Short TiO_2 annealed based.

Electrode	**PED method**	**$E_{g,R}$ [eV]**	**s [eV]**	**$E_{g,T}$ [eV], n=1/2**	**s [eV]**
Ti/TiO_2	---	3.37	0.01	3.36	0.01
$Ti/TiO_2/Cu_2O$	PED1 (120mC)	2.58	0.03	2.53	0.04
$Ti/TiO_2/Cu_2O$	PED2 (120mC)	2.60	0.05	2.56	0.06
$Ti/TiO_2/Cu_2O$	PED3 (120mC)	2.58	0.03	2.55	0.03

It is important to remark at this stage that the presence of TiO_2 nanotubes unavoidably influences the estimation of the Cu_2O band gap. This influence can be evidenced by comparing Cu_2O based electrodes achieved in the same experimental conditions (i.e. PED method) but different durations (i.e. different quantity of transferred charge, Q). In Figure 6.16 are showed the equivalent absorption spectra achieved for $Ti/TiO_2/Cu_2O$ electrodes synthesized increasing the electrodeposition time. It is evident that increasing the transferred charge, which correspond to increased amount of Cu_2O and increased dimensions of the deposits, determines an increase in the absorption across the visible region ($\lambda > 400$nm).

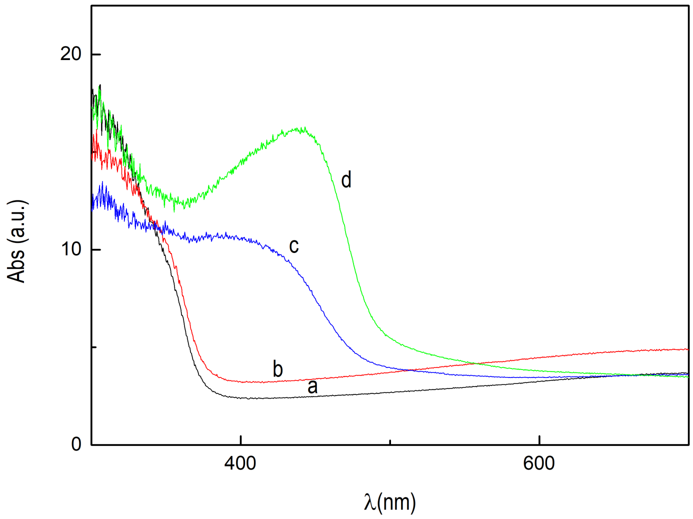

Figure 6.16 – Equivalent absorption spectra achieved for $Ti/TiO_2/Cu_2O$ electrodes synthesized following the electrodeposition method PED1 for different amount of transferred charge: 1 mC (b, red line); 10 mC (c, blue line) and 120 mC (d, green line). For comparison is reported also the bare Ti/TiO_2 annealed electrode (a, black line).

While this increase reflects improved performances in visible light absorption, which can be attributed to the deposition of Cu_2O, different absorption profiles are found, which lead to determine, with the implemented estimation methods, different band gap estimates for the same compound in the visible region (Cu_2O contribution), as well as in the UV region (TiO_2 contribution). Therefore, the Eg estimated in the visible region should be intended to provide an optical characteristic of the Cu_2O electrodeposited onto the Ti/TiO_2 nanotubes rather than of the Cu_2O pure crystal phase. On the other hand, it should be noticed that the estimated band gaps for the electrodes synthesized with transferred charge Q = 120mC are in agreement with the band-gap values reported in the literature for Cu_2O alone. Accordingly, it can be assumed that for the electrodes synthesized at 120mC, the relative abundance of the two oxides is comparable and the Eg estimations could be representative of the separate compounds that compose the electrode.

This hypothesis is supported by the FE-SEM images of the samples synthesized with transferred charges Q equal to 1 mC (Figure 6.17, A) and 120 mC (Figure 6.17, B).

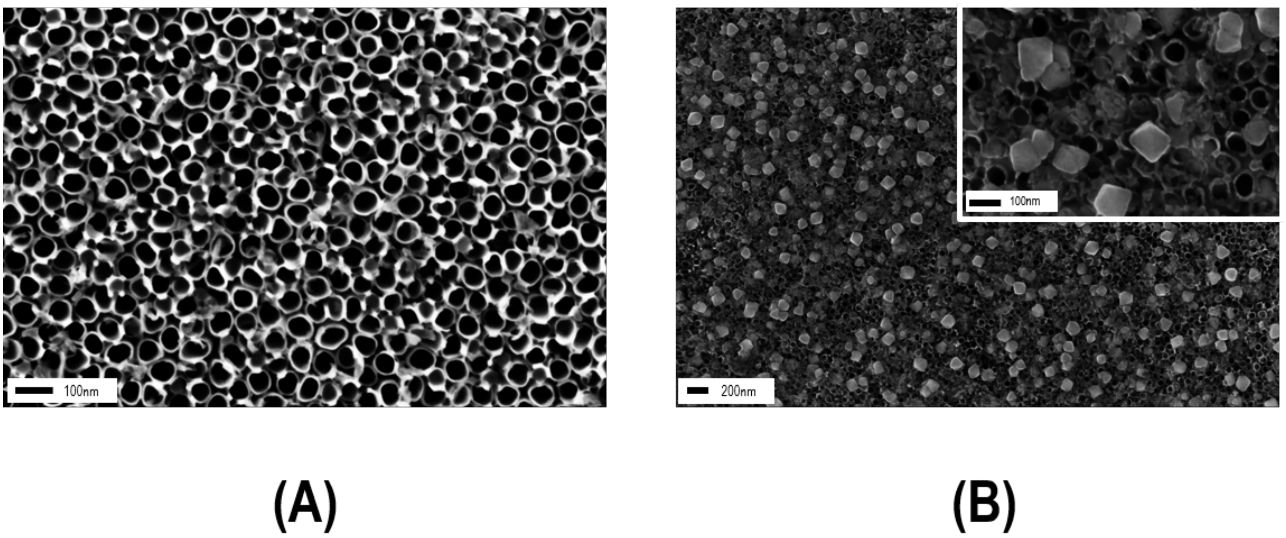

Figure 6.17 – FE-SEM images. Ti/TiO_2/Cu_2O electrode synthesized setting: A) 1 mC and B) 120 mC.

6.5 Analysis of the photocatalytic performances

6.5.1 Methylene blue photo-degradation tests

The photo-activity of the synthesized electrodes was preliminarily evaluated by analyzing their ability to catalyze the photo-degradation of methylene blue (MB). The photo-degradation experiments hereafter described were performed by employing as supported catalyst in the photocatalytic cell the Long TiO_2 NTs electrodes with and without electrodeposited Cu_2O particles.

The diagrams reported in Figure 6.18 describe the evolution of the MB concentrations observed employing the bare Ti/TiO_2 electrodes and the composite Ti/TiO_2/Cu_2O under UV + visible light irradiation (100 mW cm^{-2}). The self-degradation of MB is also reported, and the activity is estimated as the ratio between the final (C) and initial MB concentration (C_0).

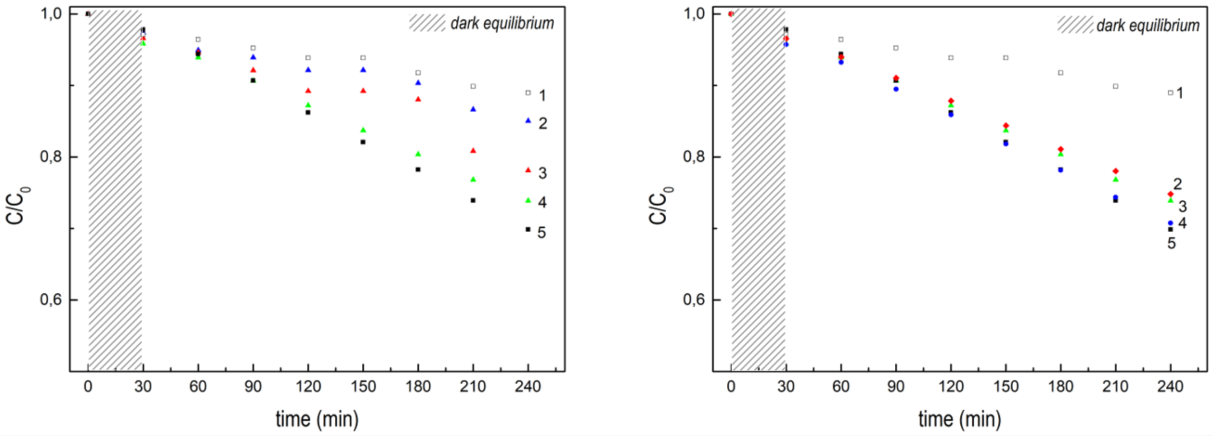

(A) **(B)**

Figure 6.18 - MB photo-degradation tests [148]. *A) Comparison between electrodes synthetized for fixed electrodeposition potential (PED2, -0.8 V), increasing the amount of transferred charge: (1) no electrode (self degradation); (2) Q = 1200 mC; (3) Q = 400 mC; (4) Q = 100 mC; (5) Q = 0 mC (bare Ti/TiO_2 electrode). B) Comparison between electrodes synthetized for fixed amount of transferred charge (Q = 100 mC), varying the electrodeposition potential: (1) no electrode; (2) PED3 (-0.9 V); (3) PED2 (-0.8 V); (4) PED1 (-0.6 V); (5) bare Ti/TiO_2 electrode. All the potential reported are Vs Ag/AgCl.*

The results of the experiments evidence that the bare Ti/TiO_2 electrodes ensure faster photodegradation of the MB as compared to the Cu_2O based electrodes. This result is not in line with expectations. The deposition of Cu_2O should allow to improve the absorption of light across the visible range, which cannot be attained with the bare TiO_2 electrode, which instead absorbs only in the UV range. Accordingly, an improved photoactivity of the composite Ti/TiO_2/Cu_2O electrodes was expected, in contrast with the results reported in Figure 6.18, as compared to the bare Ti/TiO_2 electrodes [149].

Remarkably, data reported evidence that Cu_2O based electrodes synthesized at the same electrodeposition potential but varying the Cu_2O content from 100 to 1200 mC (Figure 6.18, A), show a decrease in the photoactivity increasing the mass of the electrodeposited Cu_2O. In Figure 6.19 top-view and cross-sectional FE-SEM images of the composite electrodes employed to perform that photodegradation tests are reported. Here, according to DRS measurements (Figure 6.16), the increased sizes Cu_2O particles observed increasing the transferred charge, should have led to increased absorption across the visible range instead of the opposite behavior registered.

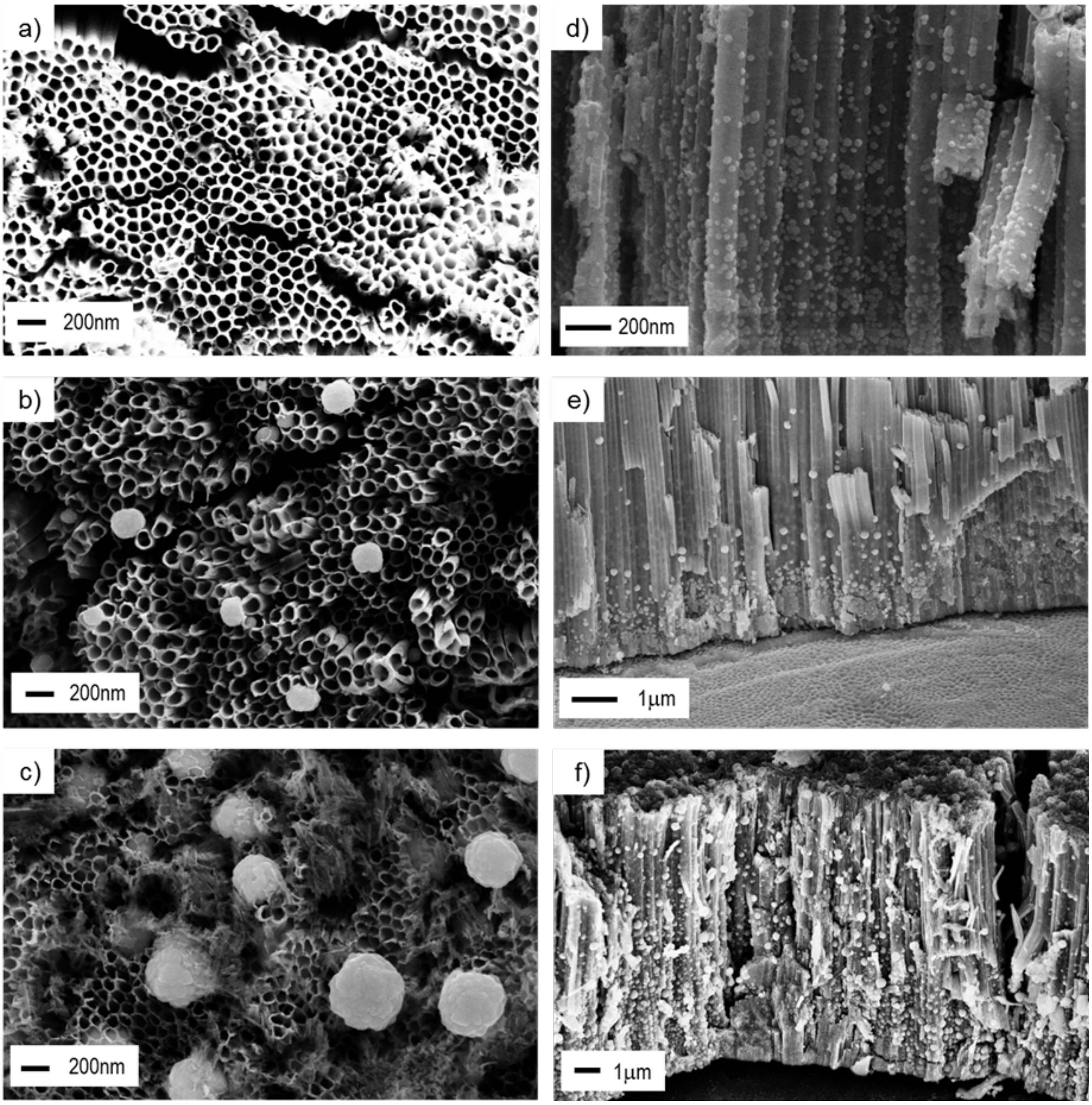

Figure 6.19 - FE-SEM images. Composite Ti/TiO$_2$/Cu$_2$O electrodes synthesized through the electrodeposition method PED2 for different amount of transferred charge: a) and d) 100 mC; b) and e) 400 mC; c) and f) 1200 mC. The images on the left are top views (a, b and c), while on the right are reported the cross sectional views (d, e, and f).

The influence of the electrodeposition potential on the photo-activity of the produced electrodes was separately investigated. The electrodes employed to perform the photo-degradation tests were synthesized fixing the amount of transferred charge and varying the electrodeposition potential from -0.6 to -0.9 V, which corresponds to the morphological transition from octahedral to spherical Cu$_2$O nanoparticles previously described in Figure 6.10. In accordance with the results of the photo-degradation tests reported (Figure 6.18, B), the transition from octahedral to spherical Cu_2O particles which is induced by increasing the cathodic potential is accompanied by a decrease in the photo-activity of the electrodes.

The results of the performed photo-degradation tests can then be summarized as follows:

- The octahedral morphology of the Cu_2O particles ensures improved photo-activity as compared to the spherical morphology;
- Increasing the Cu_2O particle size progressively deteriorates photo-degradation performances;
- Under UV + visible irradiation, the bare TiO_2 electrodes invariably exhibit improved performances as compared to the composite $Ti/TiO_2/Cu_2O$ electrodes.

A possible explanation for the reduced performances of the composite electrode is the exceedingly large size of the electrodeposited Cu_2O particles. Particularly, on the top of the TiO_2 nanotubes, Cu_2O particles with size up to 300 nm are found with transferred charge during electrodeposition equal to 1200 mC. These particles cover the underlying TiO_2 nanotubes and thus reduce the rate at which holes and electrons are photogenerated in the TiO_2. This effect is more pronounced with increasing the size of the Cu_2O particles, i.e. with increasing the transferred charge, which is in agreement with the results of the photo-degradation tests (Figure 6.18, A). The reduced photoactivity of TiO_2 nanotubes may be not compensated by the photoactivity of Cu_2O if the size of the Cu_2O particles is exceedingly large. Increasing the size of deposited Cu_2O particles decreases indeed the fraction of the holes and electrons photogenerated in Cu_2O which are effectively employed to sustain the degradation process. The diffusion length of Cu_2O has been estimated to be of the order of 100 nm [36]. Therefore, the electrons photogenerated in the bulk of the deposited 200 - 300 nm Cu_2O particles cannot reach the TiO_2/Cu_2O interface.

An additional element which may contribute to lower the performances of the composite electrode is represented by the “downwards bending” consequent to the establishment of Cu_2O/electrolyte interfaces (Figure 6.20). This bending contributes to drive the electrons towards the electrolyte interface and the holes in the opposite direction. The bending of the energy bands at the Cu_2O/TiO_2 interface is, in contrast, expected to drive the electrons from Cu_2O to TiO_2 and the holes from TiO_2 to Cu_2O (Figure 6.20). In this respect, the energy band bending taking place at the Cu_2O/electrolyte interface can be thought to configure an energy barrier to the flow of the charge carriers induced by the TiO_2/Cu_2O heterojunction, which may ultimately enhance the recombination kinetics, thus deteriorating electrode performances.

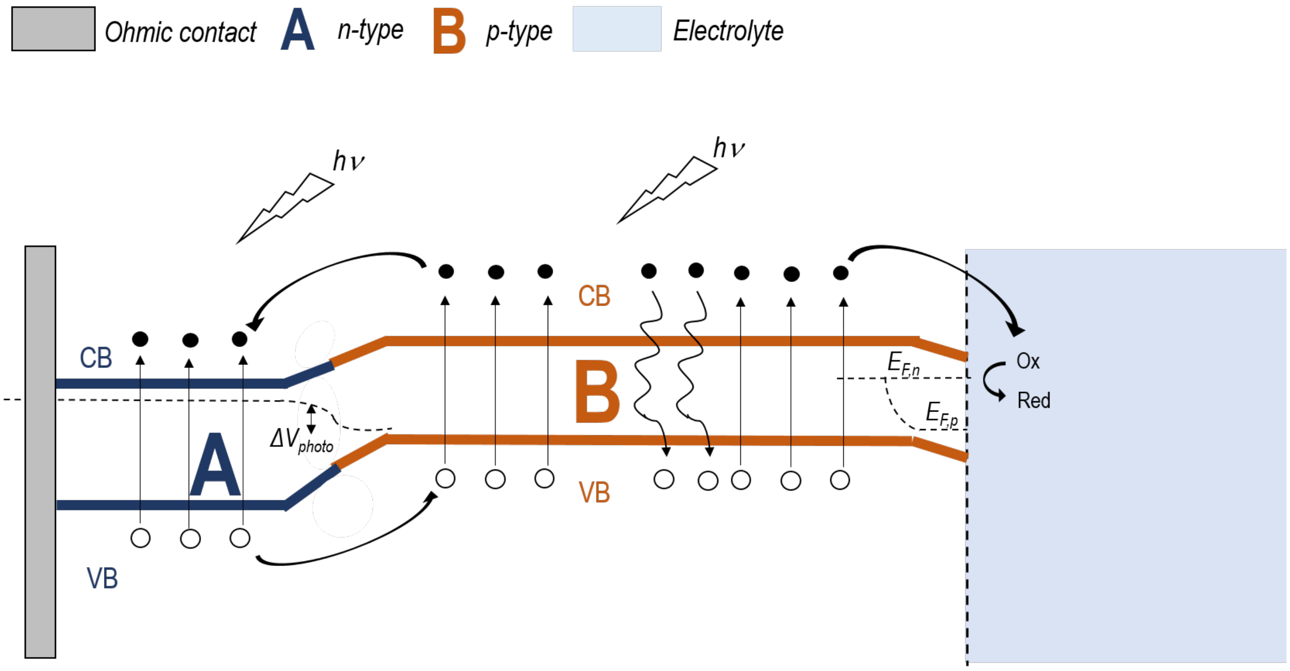

Figure 6.20 - Schematic representation of p-n photocatalyst under illumination supposing "bulk effect" due to the exceedingly large size of Cu_2O NPs.

It is important to remark at this stage that very few previous studies have demonstrated the possibility to improve the photo-catalytic performances under UV + visible light of supported Ti/TiO_2/Cu_2O. Among the available literature on Ti/TiO_2/Cu_2O systems most of the authors investigate the photoelectrochemical performances employing them as photoanodes in PEC devices [33], [150]. Furthermore, in some of these works the Cu_2O deposition is not achieved through electrodeposition, as reported by Sang et al. which deposited the Cu_2O NPs in autoclave [151]. Besides that, it is often not full clarified if the improved performances are directly attributable to the Cu_2O deposition rather than to the doping achieved during the annealing process on TiO_2 NTs (prior to the Cu_2O deposition), which could allow, alone, to achieve TiO_2 sensitization across the visible region. As for the above mentioned works ,where Authors recall previous report for TiO_2 NTs synthesis, and the performed annealing guarantees the contextual

TiO_2 doping and consequently an increased absorption in the visible region for the bare Ti/TiO_2 [152], [153].

In order to investigate the mechanisms responsible for the progressively deteriorating performances of the Ti/TiO_2/Cu_2O electrodes with increasing amount of electrodeposited Cu_2O, the photocatalysts were employed in a PEC cell as photoanodes. The results of this study are discussed in the following paragraph.

6.5.2 Photoelectrochemical tests

The synthesized electrodes were employed in a PEC cell as photoanodes in order to evaluate the photocurrent generated under UV + visible and only visible irradiation.

Separate experiments were performed under chopped light irradiation (i.e. periodically alternating dark and irradiated conditions) to emphasize the differences between the different response of the PEC cell with and without irradiation. All the experiments were performed employing as photoanodes the Short NTs electrodes (Table 6.2) with and without electrodeposited Cu_2O particles.

Prior to analyse the results of the performed photoelectrocatalytic experiments, it is here worth to clarify a fundamental difference between the application of the synthesized electrodes in a PEC cell and in the photo-degradation process analysed in the previous subsection. In the photo-degradation process, both the reduction and the oxidation reactions take place onto the electrode (Figure 6.21, B), whereas, in PEC cells, the electrode can work either as anodes or cathode, meaning that only one of the two half-reactions (i.e. reduction and oxidation) takes place over the electrode surface.

Specifically, the synthesized Ti/TiO_2 (n-type) and Ti/TiO_2/Cu_2O (p-n heterojunction) electrodes, according to the semiconductors characteristics, act as photoanodes and thus water oxidation takes place onto the photoelectrode surface, while proton reduction, with hydrogen evolution, takes place at the cathode (Figure 3.8), generally a platinum spiral wire, as used in the present study.

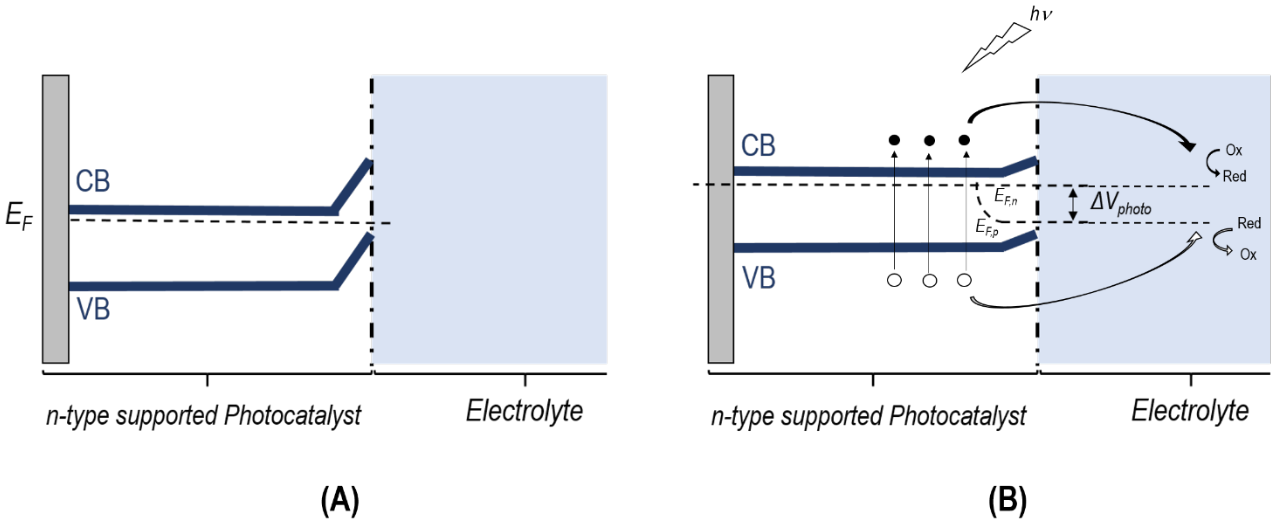

Figure 6.21 - Schematic representation of n-type photocatalyst: A) dark conditions (dynamic equilibrium) and B) under illumination.

PEC devices which employ p-Cu_2O alone, on the contrary, would show under illumination cathodic photocurrents. Here, the downward bending of the conduction and valence energy bands at the interface with the electrolyte drives the photogenerated electrons towards the electrolyte, thus promoting reduction, while the counter electrode promotes the oxidation.

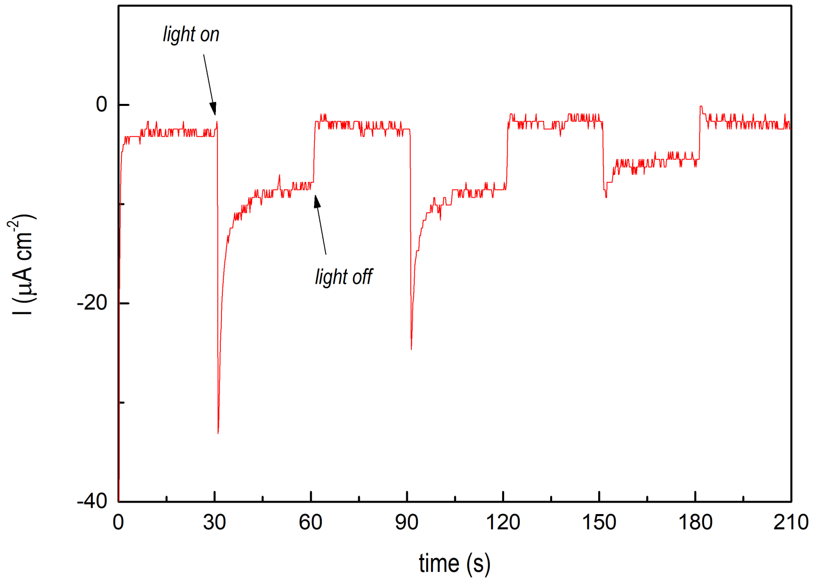

Figure 6.22 - Cathodic photocurrent registered for Cu/Cu_2O electrode under UV + visible chopped light irradiation. This electrode was been ad hoc synthesized to verify the p-type character of the Cu_2O NPs achieved through the electrodeposition method adopted in this work for the Ti/TiO_2/Cu_2O electrodes synthesis.

Figure 6.22 describes the cathodic photocurrent registered under chopped UV + visible light irradiation, for a Cu/p-Cu_2O electrode ad hoc synthesized through electrodeposition onto a

Cu planar electrode with the same electrodeposition method implemented to electrodeposit Cu_2O onto the Ti/TiO_2 electrode. Furthermore, this evidence proves the p-type character for the electrodeposited Cu_2O.

On the other hand, when Cu_2O is coupled to the n-type TiO_2 semiconductor, a p-n heterojunction is formed. It can be described as a basic diode with the current which can flow in one direction (i.e. from *p* to *n* side; forward bias) but not in the other (i.e. from *n* to *p* side; reverse bias). This is why under illumination, in principle, a p-n heterojunction would act as photoanode in a PEC cell. Furthermore, it is worth noting at this stage the role of the Ti substrate of the synthesized photoelectrodes in relation to their employment in photocatalytic cells rather than in PEC devices. In photoelectrocatalytic applications (i.e. PEC devices), it has the role of current collector, thus, according to the configuration described above, electrons will flow to the counter electrode and no trap state effects are expected [154], as instead in photocatalytic degradation tests, where the Ti substrate is not connected to the external circuit and both reactions take place over the p-n heterojunction based catalyst surface. Here, the electrons that flow prom *p* to *n* and then to the Ti substrate cannot flow in an external circuit neither promote directly the reduction (Ti substrate not exposed to the electrolyte), thus the recombination phenomena probability (with the photogenerated holes in the n-side, at the solid interface Ti/TiO_2) increases, contributing to deteriorate the overall performances.

The synthesized electrodes were firstly characterized through a pulsed light linear sweep voltammetry (PL-LSV), which consists of a classic LSV carried under chopped light irradiation.

Figure 6.23 shows the evolution of the current with potential recorded during the PL-LSV under UV + visible light irradiation with the bare Ti/TiO_2 (a, black line) and the Ti/TiO_2/Cu_2O (b, red line) electrode in Na_2SO_4 0.01 M.

Both the employed electrodes show the characteristic behavior of photoanode under illumination. Over the cathodic range from -1.5 to around -0.8 V (Figure 6.23, inset), the irradiation does not affect significantly the generated current, which is mainly determined by the application of the cathodic potential. This is apparent by the absence of differences between the current values generated during the dark and the irradiated period. This can be explained by noticing that the application of these cathodic potential values increases the built-in potential difference across the interface between the two semiconductors, implying that the heterojunction is operated under reverse bias [90].

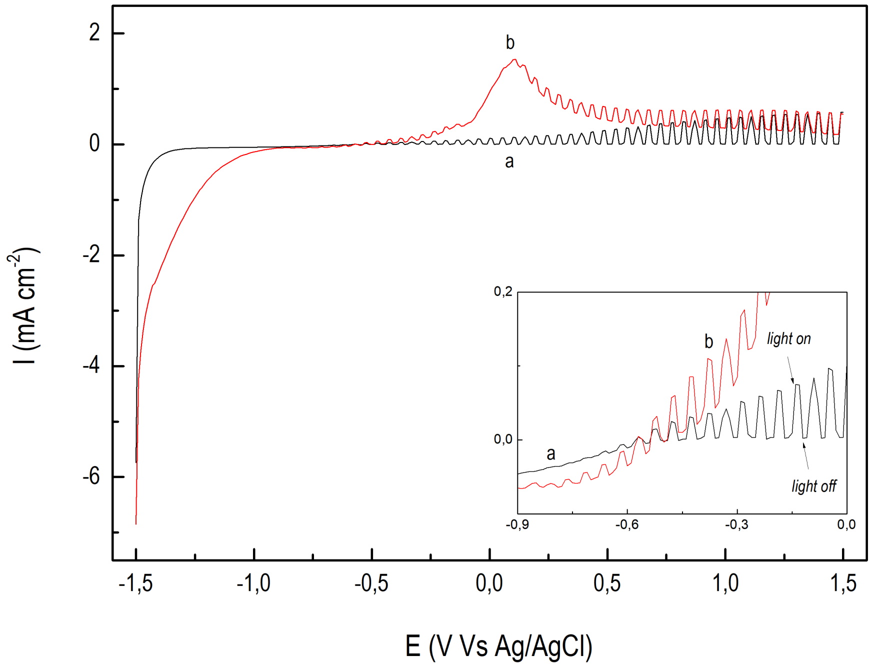

Figure 6.23 – PL-LSV carried out under UV + visible light irradiation (100 mW cm^{-2}), employing as working electrodes: a) Ti/TiO_2 (black line) and b) Ti/TiO_2/Cu_2O (red line). The insert is a magnification of the potential range corresponding to the transition from cathodic to anodic currents.

Moving towards more anodic potentials the effect of the irradiation becomes noticeable. The anodic current densities registered show an increase in correspondence of each light pulse. Comparing the two electrodes, Ti/TiO_2/Cu_2O is characterized by a higher anodic photocurrent in the entire potential range investigated, thus apparently exhibiting improved performances respect to the bare Ti/TiO_2. The anodic photocurrent generated with the bare Ti/TiO_2 monotonically increases as the potential increases above the short-circuit value (~-0.55 V), i.e. with increasing the applied forward bias. For the Ti/TiO_2/Cu_2O, the anodic current reaches, in contrast, a maximum value around 0,1 V and then decreases, eventually approaching the anodic photocurrent generated with the bare Ti/TiO_2 electrode. The anodic current peak attained with the Ti/TiO_2/Cu_2O electrode, as supported by several authors [101], [109], [155], could be attributable to corrosion processes promoted by the synergistic effect of the photogenerated holes (h^+) and the applied potential (direct bias lead to an increase in the charge carriers concentration):

$$Cu_2O + 2OH^- + 2h^+ \rightleftharpoons 2CuO + H_2O \tag{6.7}$$

$$Cu_2O + H_2O + 2OH^- + 2h^+ \rightleftharpoons 2Cu(OH)_2 \tag{6.8}$$

The PL-LSV experiment was performed also employing as irradiation source only visible light (Figure 6.24). As expected, the bare Ti/TiO$_2$ electrode doesn't produce any significant anodic photocurrent as compared to the same electrode under UV + visible irradiation (Figure 6.23). Ti/TiO$_2$/Cu$_2$O allows generating, in contrast, an anodic photocurrent, which can be attributed to the ability of Cu$_2$O to absorb the radiation energy across the visible range. However, with Ti/TiO$_2$/Cu$_2$O electrode, the photogenerated current is significantly lower than that observed under UV + visible light. This indicates that the number of photogenerated charge carriers is strongly influenced by the TiO$_2$ contribution.

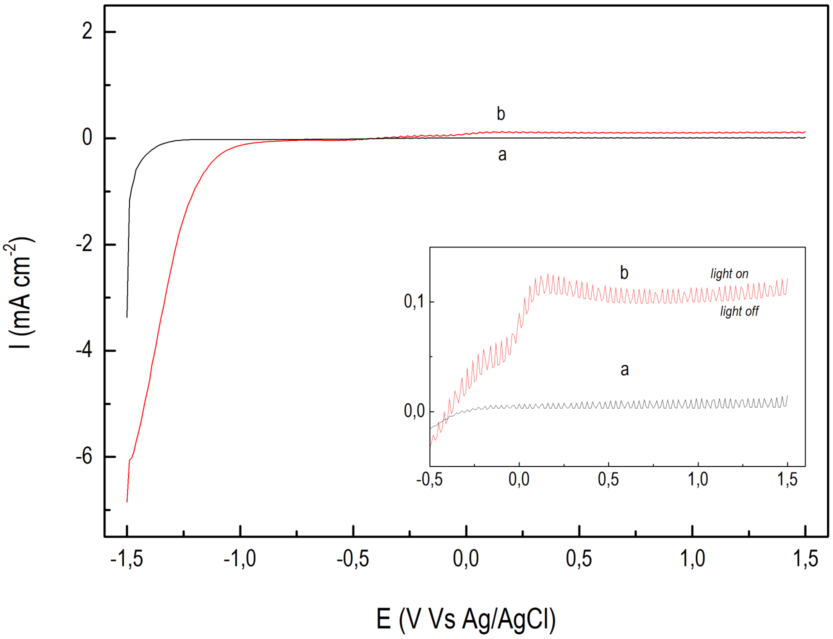

Figure 6.24 - PL-LSV carried out under only visible light irradiation (100 mW cm^{-2}), employing as working electrodes: a) Ti/TiO$_2$ (black line) and b) Ti/TiO$_2$/Cu$_2$O (red line). The insert is a magnification of the potential range corresponding to the transition from cathodic to anodic currents.

A maximum in the anodic photocurrent is, again, attained under visible light only around 0.1 V, as previously found under UV + visible light (Figure 6.23). Following the maximum, the photocurrent slightly decreases to a current value which is maintained constant at larger potential values. The different photocurrent maxima attained at identical potential values under UV + visible light (Figure 6.23) and visible light only (Figure 6.24) suggest that the photo-corrosion process (Equations 6.7 and 6.8) could be mainly influenced by the number of photogenerated charge carriers in TiO_2 rather than by the applied potential.

Electrode performances were successively analyzed by photocurrent tests performed at imposing a constant potential equal to the open-circuit potential (i.e. zero current), attained under dark conditions. With this approach, the contribution to the photocurrent generated by the application of a potential bias (i.e. forward or reverse bias) is excluded.

The temporal evolution of the photocurrent generated with the bare Ti/TiO_2 and the composite Ti/TiO_2/Cu_2O electrode under UV + visible and only visible chopped light irradiation are compared in Figure 6.25. The analysis confirms the photo-inactivity of TiO_2 under only visible light irradiation.

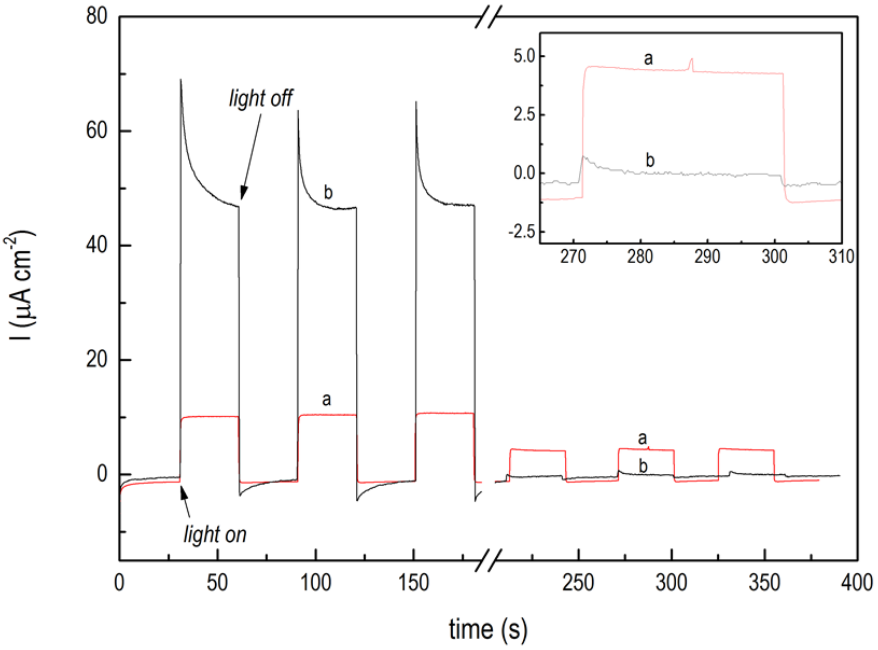

Figure 6.25 - Photocurrent registered during chopped light irradiation (100 mW· cm^{-2}) for Ti/TiO_2 electrode (a, black line) and composed TiO_2/Cu_2O Electrode (b, red line). After the axis break (t > 200 s) an UV cut-off filter was used (only visible irradiation). The insert is a magnification of the photocurrent registered under only visible irradiation.

The composite Ti/TiO_2/Cu_2O electrode, in contrast, allows to generate an anodic photocurrent under visible irradiation. This ability confirms that the composite p-n heterojunction allows effectively separating photogenerated charge carriers, with electrons driven from Cu_2O to TiO_2. The anodic photocurrent generated with the composite electrode increases under UV + visible light (Figure 6.25, before the axis break), which can be attributed to the contribution of TiO_2 induced by the UV irradiation. However, under UV + visible light irradiation, the photocurrent density with the composite electrode is lower than the photocurrent generated with the bare TiO_2 electrodes.

6.5.2.1 Analysis of the mechanisms justifying the lower performances of the composite electrodes

It is important to remark at this stage that the composite electrodes are developed to improve the photoelectrochemical performances as compared to the bare TiO_2 electrodes under sunlight irradiation, i.e. UV + visible light. Therefore, the ability to generate an anodic photocurrent over the visible light range, where the TiO_2 is photo-inactive, cannot be considered sufficient to justify the application of the synthesized composite electrode in place of the bare Ti/TiO_2 electrode. Remarkably, this analysis is in contradiction with most of the previous studies analyzing the photocatalytic application of composite Ti/TiO_2/Cu_2O electrodes generated by electrodeposition onto TiO_2 nanotubes [33], [150]. In these latter studies, improved performances of the composite electrodes as compared to the bare TiO_2 electrode have been frequently claimed based on the only analysis of the photocatalytic performances under visible light only [98], [110], [144], [156]–[158].

Only few studies critically compared the performances of the composite and the bare TiO_2 NT electrodes over the UV + visible light, evidencing the difficulty to get improved performances by the electrodeposition of Cu_2O over TiO_2 NTs, [36], [101], [151], [159]. Some authors proposed that the lower performances of the composite electrode under UV + visible light may be attributed to the relative position of the Cu_2O energy bands with respect to the potentials of reduction of copper species, assuming that the Cu_2O "self-degradation" in aqueous solution takes place [36]. However, with this hypothesis, the occurrence of photo-corrosion should determine a progressively varying photocurrent, which is not the case of the present study, where a stable photocurrent was observed with the composite electrodes during any light pulse (Figure 6.25). The hypothesis of photo-corrosion would be consistent with electrodes showing improved performances with respect to the bare TiO_2 but progressively deteriorating under irradiation [36]. Furthermore, the PL-LSV characterization performed with the composite electrodes synthesized in this work (Figures 6.23 and 6.24) indicated that photo-corrosion processes are promoted by the synergistic effect of the photogenerated charge carriers and the applied potential (i.e. forward bias), whereas the photocurrent tests (Figure 6.25) were performed at the OCP attained under dark conditions, i.e. without any potential bias. Likewise, Zhao et al. attribute the deteriorating performances to the role played by the p-Cu_2O/electrolyte interface with increasing the Cu_2O particle size [160].

Other authors attribute the lower performances of the composite electrode to an increased recombination rate of the photogenerated hole-electron pairs, which would be determined by the morphology and size of the deposited particles. These authors propose that the coupled semiconductor may act as a recombination center rather than promoting the charge carrier separation [99], [161]. This latter explanation may be consistent with the results attained in this work, considering that, in the photo-degradation experiments described in the previous section, a progressive decrease in the performances is observed with increasing the Cu_2O NPs size.

The influence of the Cu_2O particles size can be explained considering that while the energy bands bending taking place at the Cu_2O/TiO_2 interface drive electrons from the Cu_2O to TiO_2 and holes into the opposite direction, a downwards bending of the energy bands takes simultaneously place at the Cu_2O/electrolyte interface (Figure 6.20). This latter bending, as widely discussed in the previous section (paragraph 6.5.1) configures an energy barrier to the flow of electron and holes in the directions determined by the energy band profiles across the Cu_2O/TiO_2 interface, which can ultimately decrease the photocatalytic performances of the composite electrode as compared to the bare Ti/TiO_2 electrode. According to that, if the particles size would be sufficiently small, the space charge layer at the Cu_2O-electrolyte interface would be “covered” by the space charge layer at the Cu_2O-TiO_2 interface and as consequence becomes negligible.

An alternative explanation for the lower performances of the composite electrode could be derived by the analysis of the composition of the deposited particles. In accordance with the XRD analysis, Cu_2O is the only crystal copper phase identified in the composite electrode (Figure 6.13). On the other hand, other copper species may be present exhibiting an amorphous structure, which cannot thus be identified by XRD. In order to evaluate the possibility that amorphous solid phases are formed during electrodeposition, along with the crystal Cu_2O, it is useful analyzing the temporal evolution of the current recorded during the copper pulsed electrodeposition onto TiO_2 nanotubes. As representative example, the current generated by the implementation of the PED1 method (Table 5.4) is reported in Figure 6.26. With this electrodeposition method, a constant potential is imposed during ton period to electrodeposit copper, while a zero current is maintained during the toff period to restore the copper ion concentration into the TiO_2 nanopores. During this latter t_{off} period, the applied potential is the open circuit potential.

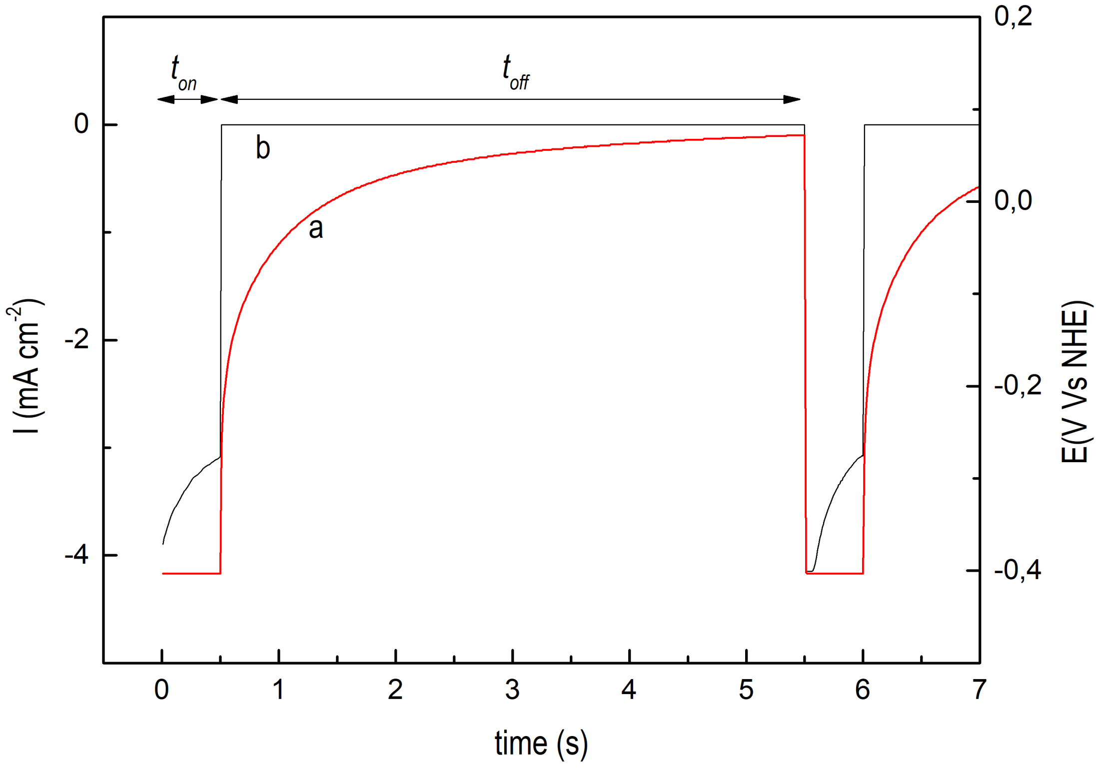

Figure 6.26 – Characteristic behaviour (early stage) of the pulsed electrodeposition method (PED1), employed for the $Ti/TiO_2/Cu_2O$ synthesis. Two characteristic period are highlighted: t_{on} period corresponds to the cathodic pulse, while t_{off} period is the "zero-current" time. The current signal corresponds to the curve b (black line), while a is the potential (red line).

Figure 6.26 evidences that this potential progressively increases during the t_{off} period towards more anodic values, which can be associated to a modification of the electrode surface. This modification could be attributed to the precipitation of $Cu(OH)_2$, which is photo-inactive and could thus deteriorate the performances of the synthesized electrode. While the formation of a photo-inactive phase unavoidably decreases light harvesting and can thus deteriorate the electrode performances, few authors have reported that coupling TiO_2 with $Cu(OH)_2$ particles may improve the performances as compared to the bare TiO_2 electrode.

Yu et al. reported improved performances achieved with $Cu(OH)_2$ cluster-modified TiO_2 powder, employed to sustain the unassisted photocatalytic hydrogen production in aqueous ethylene glycol [162]. The authors report that the photoactivity decreases with increasing the $Cu(OH)_2$ cluster size: It should be taken into account that the early photogenerated electrons, providing the partial reduction of Cu^{2+} to Cu^0, lead to the formation of $Cu(OH)_2/Cu$ core-shell clusters. In this configuration the effective co-catalyst would be Cu instead of $Cu(OH)_2$, so that increased dimensions of the core-shell $Cu(OH)_2$ based clusters would lead to the ineffectiveness of the Cu co-catalyst [162].

Dang et al. investigated the same $Cu(OH)_2/TiO_2$ combined system using TiO_2 nanotubes [163]. They observed that for $Cu(OH)_2$ content below 8 $\%_{wt}$ the photocatalytic hydrogen generation increases significantly with increasing $Cu(OH)_2$ content (due to its effective dispersion on the surfaces of the TiO_2 nanotubes), while, the further increase (> 8 $\%_{wt}$) corresponds to a decay in the photoactivity. The decay is attributed to the excessive cluster dimensions which would inhibit the TiO_2 light absorption (decreased photoactive surface).

Although these latter works don’t help to clarify if the surface composition of the deposited particles could be the reason of the decrease in the photoactivity, both $Cu(OH)_2/TiO_2$ systems [162], [163] and Cu_2O/TiO_2 systems [36], [160], show the same performance decay respect the increase in the dimensions of the deposited species.

6.5.2.2 XPS characterization of the electrodes

In order to verify this assumption on the formation of $Cu(OH)_2$, and taking into account that bulk composition of the deposited particles would correspond to crystalline Cu_2O (XRD data,

Figure 6.13), a further investigation was carried out by means of XPS, in order to verify the surface composition of the deposited particles.

In Figure 6.27 are reported the Cu 2p spectra for the bare Ti/TiO_2 (A) and the composite electrode (B), both measured as synthesized. As expected, in the binding energy range 930 - 965 eV only the composite electrode spectrum shows peaks. The peak analysis highlighted the presence of both Cu(I), ~ 932.5 eV (Figure 6.27 B, component 1), and Cu(II), ~ 935 eV (Figure 6.27 B, component 2, to which the satellite lines in the range 940 - 950 are associated).

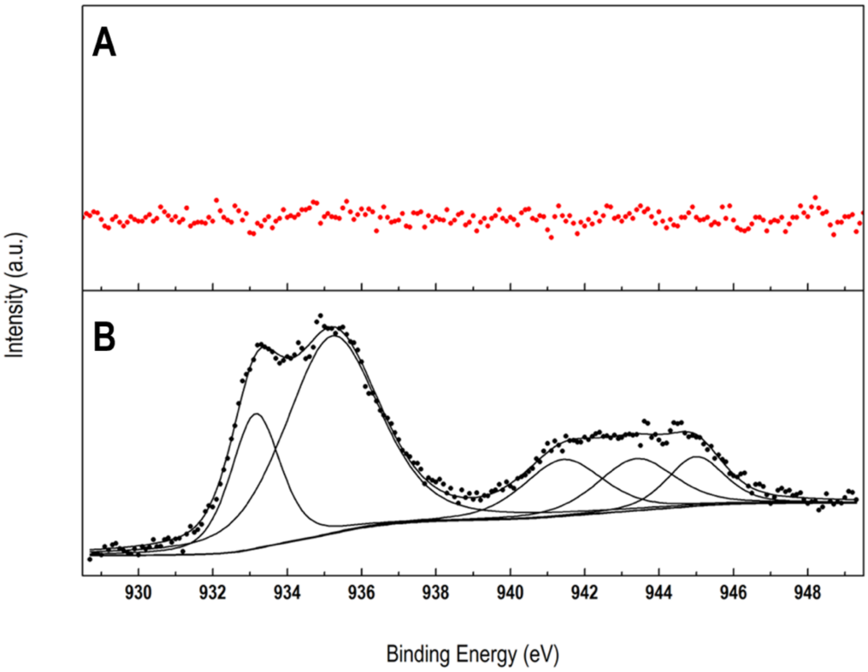

Figure 6.27 - XPS spectra in the Cu 2p region for Ti/TiO_2 electrode (A, red dots) and composite electrode (B, black dots).

This first evidence confirms a surface modification of the deposited particles. To understand if the Cu(II) is due to CuO or $Cu(OH)_2$, the region O 1s and C 1s (Figure 6.28, A and B respectively) were also investigated.

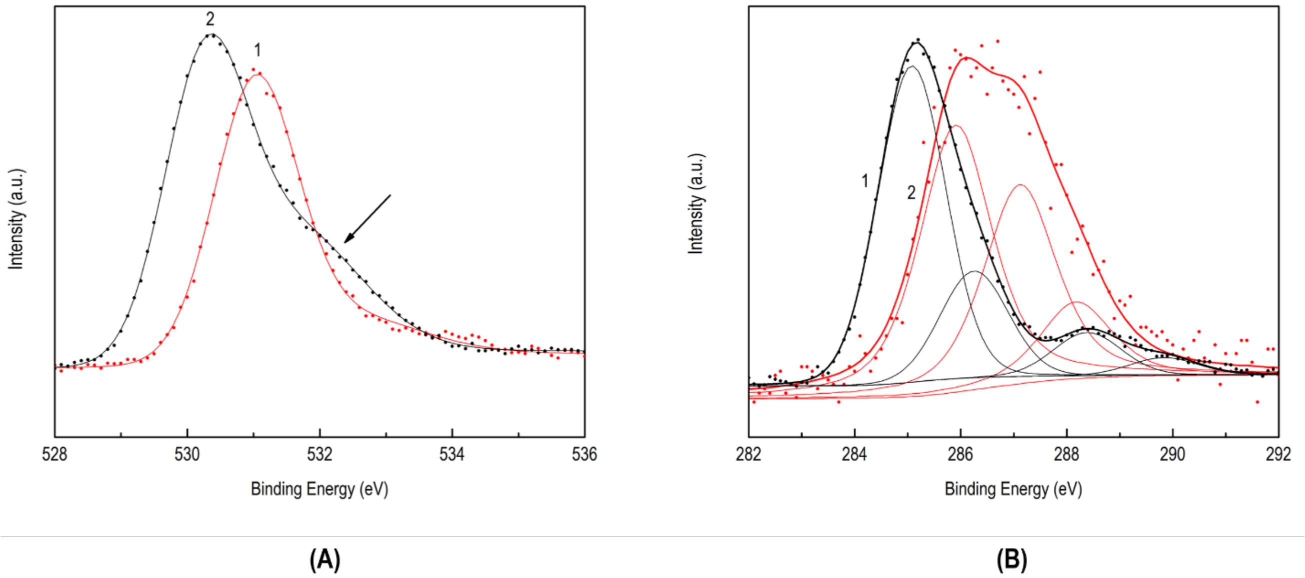

Figure 6.28 - XPS spectra of the O 1s (A) and C 1s region (B). A) bare Ti/TiO₂ (1, red line) and composite electrode (2, black line); B) bare Ti/TiO₂ (2, red line) and composite electrode (1, black line). It should be highlighted that the black line (1) in spectrum B is normalized to the intensity of the other peaks for qualitative comparison on peaks shape and position.

The O 1s spectrum for the bare Ti/TiO_2 electrode (Figure 6.28 A, 1) shows a signal (~ 531 eV) due to TiO_2, while for the composite electrode (Figure 6.28 A, 2), the peak due to the metal oxides (both TiO_2 and Cu_xO) falls at lower binding energies (~ 530 eV), and a second signal due to hydroxide appears (Figure 6.28 A, 2, black arrow). The C 1s region spectra were also analyzed. As showed in Figure 6.28 B, for the bare Ti/TiO_2 electrode (2, red line) there is a weak and wide signal related to carbon (the red line (2) in spectrum B is normalized to the intensity of the other peaks for qualitative comparison on peak shapes and positions), while for the composite electrode there is a majority component due to C=C ligands (~ 285 eV), a second one related to C-O-H (~ 286 eV) and a third one related to O-C=O groups (~ 288 eV). These results, highlighted in the deconvoluted peaks of Figure 6.29, are in good agreement with data reported from Zhu et al. for Cu_2O deposited in similar electrodeposition conditions [164]. The same Authors, consistently also to Baklanov et al., identify in the region attributable to hydroxide a further weak signal, which they assign to CO_3^{2-} (~ 289 eV) and related to the presence of Cu(II) carbonate which normally stabilize $Cu(OH)_2$, in agree with the composition of the employed electrodeposition electrolyte [165]. These evidences would corroborate the hypothesis of decreased photoactivity due to the $Cu(OH)_2$ "coverage effect" which could inhibit the Cu_2O light absorption.

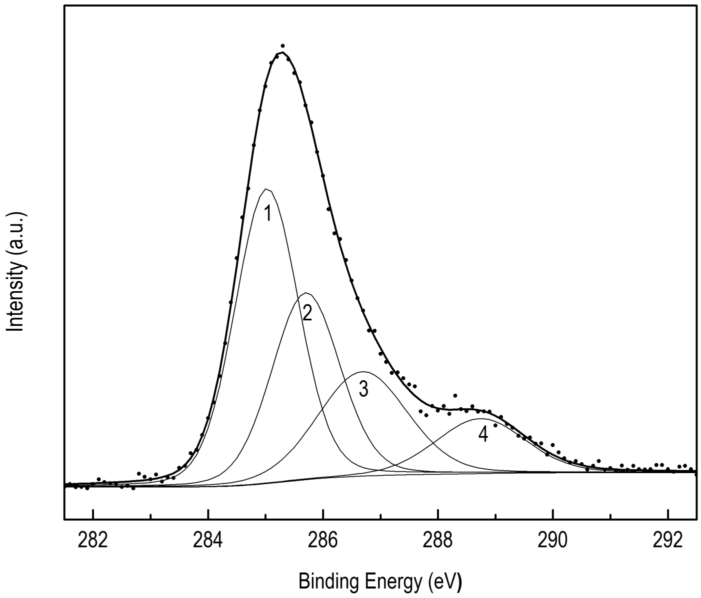

Figure 6.29 - XPS spectrum of the C 1s region. Peaks deconvolution related to the Ti/TiO_2/Cu_2O electrode reported in Figure 6.27, B.

6.5.2.3 Improving the performances of the composite under UV + visible irradiation by electrochemical post-treatment

In accordance with the illustrated analysis, the lower performances of the composite electrodes as compared to the bare Ti/TiO_2 electrodes under UV + visible irradiation may be explained by the large size and/or the surface composition of the deposited particles. A strategy to improve the performances of the composite electrode would be then modifying the electrodeposition strategy and parameters to decrease, at any prescribed transferred charge Q, the size and the surface density of the electrodeposited particles, and to prevent the formation of the copper hydroxide phase. For what concerns the size control, it must be noticed that the electrodeposition technique hardly allows distributing the amounts of electrodeposited copper per surface unit targeted by the present study among nanoparticles with size below 100 nm. The main reason is that, as the transferred charge is increased, the reduced species are favorably attached to the previously deposited particles and unlikely contribute to form new nuclei, which has been recently referred to as the "Gordian knot" of electrodeposition [166].

The idea followed in the present study to overcome this limitation is to perform a controlled polarization of the electrode covered by electrodeposited Cu_2O particles in an electrolyte solution not containing the precursor copper metal ion, starting in the cathodic range towards anodic potentials. Under this condition, within the cathodic range, copper electrodeposition cannot take place but phenomena allowing to purposefully modify the morphology of the previously electrodeposited particles covering the electrode can be induced. This approach is motivated by recent studies of recrystallization phenomena induced by electrode polarization. It has been demonstrated that the application of sufficiently large cathodic potentials in electrolyte solutions not containing the precursor metal ion can induce the detachment of nanoclusters from the previously electrodeposited particles [166]. These nanoclusters can diffuse over the electrode surface and then form new particles, thus allowing decreasing the size and increasing the surface density of particles.

Furthermore, it has been previously reported that the polarization under illumination of Cu_2O based electrodes in solutions not containing the copper ion precursor can induce a recrystallization triggering a morphological transition to thin planar nanostructures and nanoflakes [109].

Inspired from these experimental evidences, an electrochemical post-treatment of the synthesized composite electrodes was developed to modify the morphology of the electrodeposited Cu_2O particles. The post-treatment consists of a linear sweep voltammetry (LSV) with the potential varying from cathodic to anodic values, performed in the same electrochemical cell employed to run the photoelectrochemical tests but using an electrolyte not containing the precursor copper ion. The main idea is to promote the recrystallization by the application of a sufficiently large cathodic potential, thus partially reducing the surface copper oxide species, and then progressively re-oxidizing the copper deposit to ensure the formation the Cu_2O photoactive phase. Two LSVs were separately evaluated in dark and under irradiation, which will be hereafter referred to as dark and lighted LSV, respectively. A third post-treatment was successively evaluated including the sequence of the dark and of the lighted LSV (1st scan dark, 2nd scan lighted), which will be referred to as double LSV.

The evolution of the photocurrent generated during the dark and the lighted LSV by scanning the potential with rate equal to 20 mV s^{-1} from -1.5 to 1.5 V (vs. Ag/AgCl) are reported in Figure 6.30.

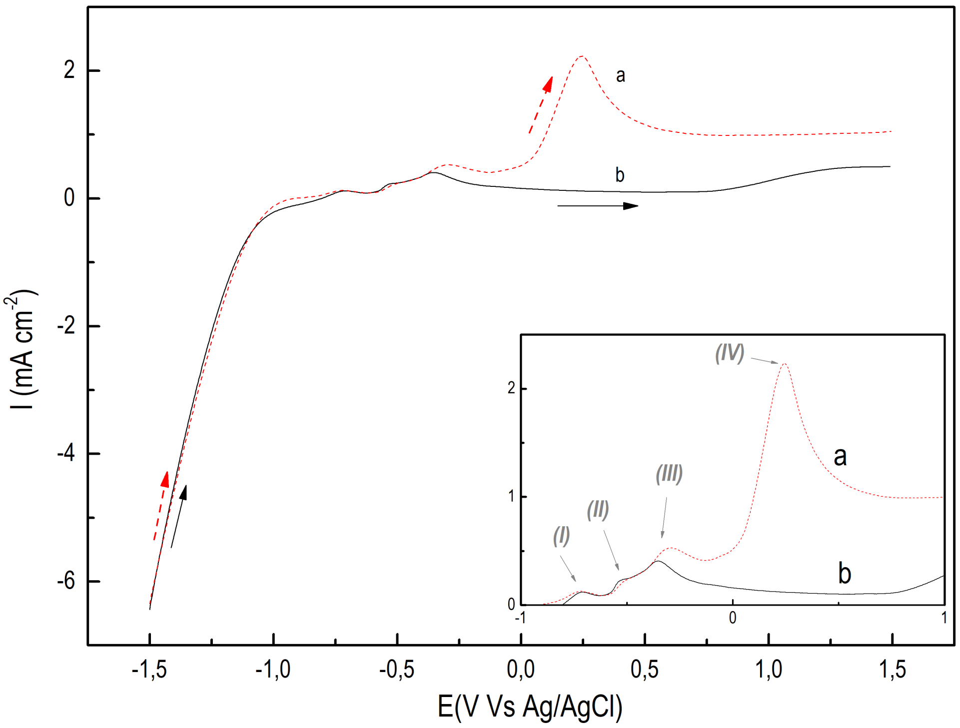

Figure 6.30 - LSV with composed electrodes (Ti/TiO_2/Cu_2O) as WE. a) dark condition (black line); b) under UV + visible irradiation (red dashed line). The insert is a magnification of the oxidation peaks (I, II, III, IV).

The cathodic current observed upon the application of the initial cathodic potential can be imputed to the water reduction (equation 6.9), and to a partial reduction of the Cu(I) to Cu(0) (equation 6.10):

$$2H_2O + 2e^- \rightleftharpoons H_2 + 2OH^- \tag{6.9}$$

$$Cu_2O + H_2O + 2e^- \rightleftharpoons 2Cu_{(s)} + 2OH^- \tag{6.10}$$

As the potential is increased, three oxidation peaks (Figure 6.30, insert I, II, III) appears for both LSV treatment (dark condition and lighted scan). The possible oxidation reactions that can justify these peaks are described as follows:

$$Cu_2O + H_2O + 2e^- \rightleftharpoons 2Cu_{(s)} + 2OH^- \tag{6.11}$$

$$2CuO + H_2O + 2e^- \rightleftharpoons Cu_2O + 2OH^- \tag{6.12}$$

$$CuO + H_2O + 2e^- \rightleftharpoons Cu + 2OH^- \tag{6.13}$$

$$2Cu(OH)_2 + 2e^- \rightleftharpoons Cu_2O + H_2O + 2OH^- \tag{6.14}$$

$$Cu(OH)_2 + 2e^- \rightleftharpoons Cu + 2OH^- \tag{6.15}$$

$$Cu^{2+} + 2e^- \rightleftharpoons Cu_{(s)} \tag{6.16}$$

$$Cu^+ + e^- \rightleftharpoons Cu_{(s)} \tag{6.17}$$

A fourth oxidation peak around 0.2 V is found for the lighted scan only under UV + visible irradiation (Figure 6.30, insert IV). This oxidation was observed also during the PL-LSV characterization, and as previously mentioned would be attributable to corrosion processes promoted by the synergistic effect of the applied potential and the photogenerated holes (h^+), (equations 6.7 and 6.8).

FE-SEM analysis was performed to evaluate changes in the morphology of the deposited particles at the end of the LSV treatments (Figure 6.31). After the dark LSV, a change in the morphology of the deposited particles is observed as compared to the original composite electrode (Figure 6.17, B): the octahedral shape is no longer present while spherical rounded particles appear (Figure 6.31 A). It is conjectured that the loss of the polyhedral particle geometry could be attributed to the partial surface reduction of the copper oxide and by the oxidation reactions determining the peaks (I)-(III) in Figure 6.30.

Following the lighted LSV, the appearance of rounded particles is again observed. However, along with these rounded particles, differently from what observed after the dark LSV, new larger tetrahedral clusters are found (Figure 6.31, B). In order to identify the process responsible for this larger clusters, it must be remarked that the only qualitative difference between the photocurrent evolutions recorded during the lighted and the dark LSV (Figure 6.30) is represented by the oxidation peak IV. This suggests that the appearance of these new larger clusters, which are not produced with the dark LSV, could be attributed to the photo-corrosion process taking place around the peak IV.

The last treatment tested consists of the sequence of the two LSV, dark first and then lighted. The FE-SEM images taken after this treatment (Figure 6.31, C) evidence relevant differences as compared to the electrodes generated by dark and lighted LSV (Figure 6.31 A, B). Indeed, the small rounded particles (Figure 6.31 A, B) are not yet visible, while the surface of the nanotubes layer is covered by the same large tetrahedral clusters appeared after lighted LSV. Further, the appearance of large planar clusters is found (Figure 6.31 C).

As reported by several authors, the tetrahedral morphology of the new clusters formed is coherent with CuO presence [167], [168]. Absorption spectra registered for the same treated samples (Figure 6.32), exhibit an increase in the absorption towards the visible region (i.e. lower energy band gaps [99]), which further support the hypothesis on CuO formation.

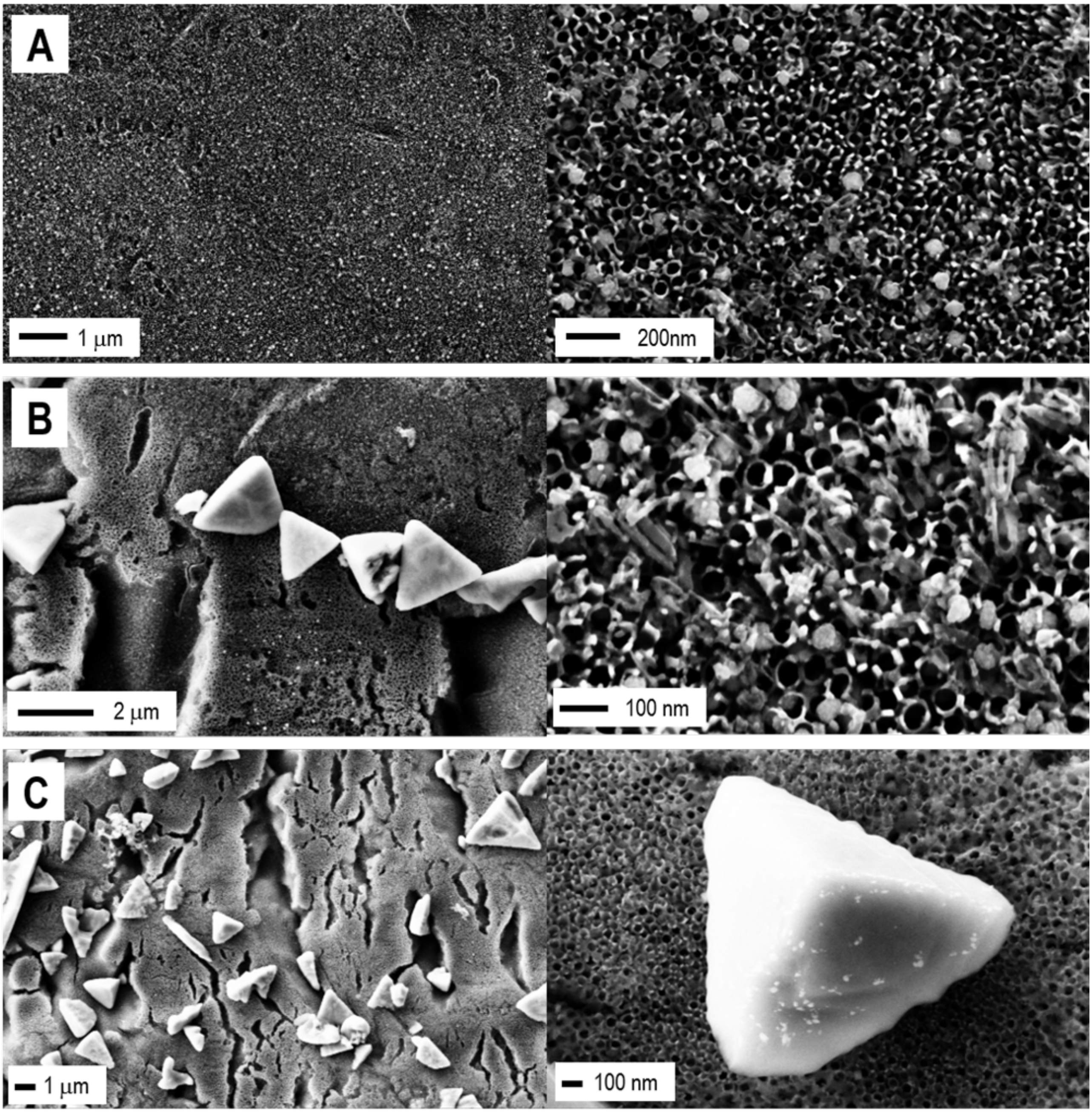

Figure 6.31 - FE-SEM images of Short composite electrode (Ti/TiO_2/Cu_2O) after LSV post-treatment: A) dark LSV; B) lighted LSV; C) double LSV (1st scan dark, 2nd scan lighted).

To evaluate the effectiveness of the treatments in terms of photocurrent density, the treated electrodes, characterized by the presence of a mixture of Cu_xO species (Figure 6.32), were then employed as photoanodes in a PEC cell. Photo-electrochemical experiments were performed under chopped light UV + visible irradiation by maintaining the potential equal to the OCP measured under dark conditions.

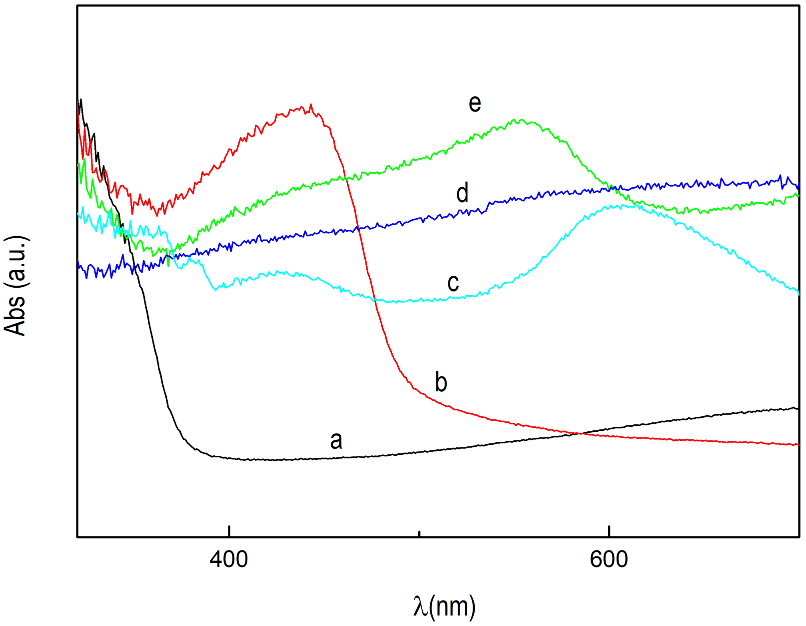

Figure 6.32 - Equivalent absorption spectra registered after LSV post-treatments: Ti/TiO$_2$ electrode not treated (a, black line); composite Ti/TiO$_2$/Cu$_2$O electrode not treated (b, red line); dark LSV treated (e, green line); lighted LSV treated (d, blue line); double LSV treated (c, cyan line).

Irrespective of the previously implemented post-treatment (i.e. dark, light and double LSV), a progressive variation of the OCP in dark was observed during the experiment. This variation was marked by the onset of a cathodic current during the dark period (Figure 6.33). Therefore, in order to evaluate the OCP variation effect on the photogenerated current, this set of experiments were carried out by periodically interrupting the illumination after a fixed number of dark/light cycles, measuring the OCP of the electrode in dark and then restarting the photoelectrochemical test with the potential equal to the new OCP value (Figure 6.33 A). This procedure was repeated until the photocurrents generated during the dark cycles were no longer appreciably deviating from the zero current value, thus evidencing stability of the electrode surface.

The progressive variation of the OCP during the experiment indicates that the electrode is undergoing a modification owing to effect of the light irradiation. This is confirmed by the evolution of the absorption spectra reported in Figure 6.33 B, which were recorded at the end of each series of dark/light cycle with constant potential. Specifically, as it is shown in Figure 6.33 B, at the end of the dark LSV treatment, a new absorption peak attributable to CuO appears towards lower band gap values in the visible region (before 1st cycle), while, during the photocurrent experiments, this peak disappears (before 4th cycle). Particularly, the evolution of the absorption spectra suggests that the electrode could eventually recover (before 6th cycle) the initial condition prior post-treatment.

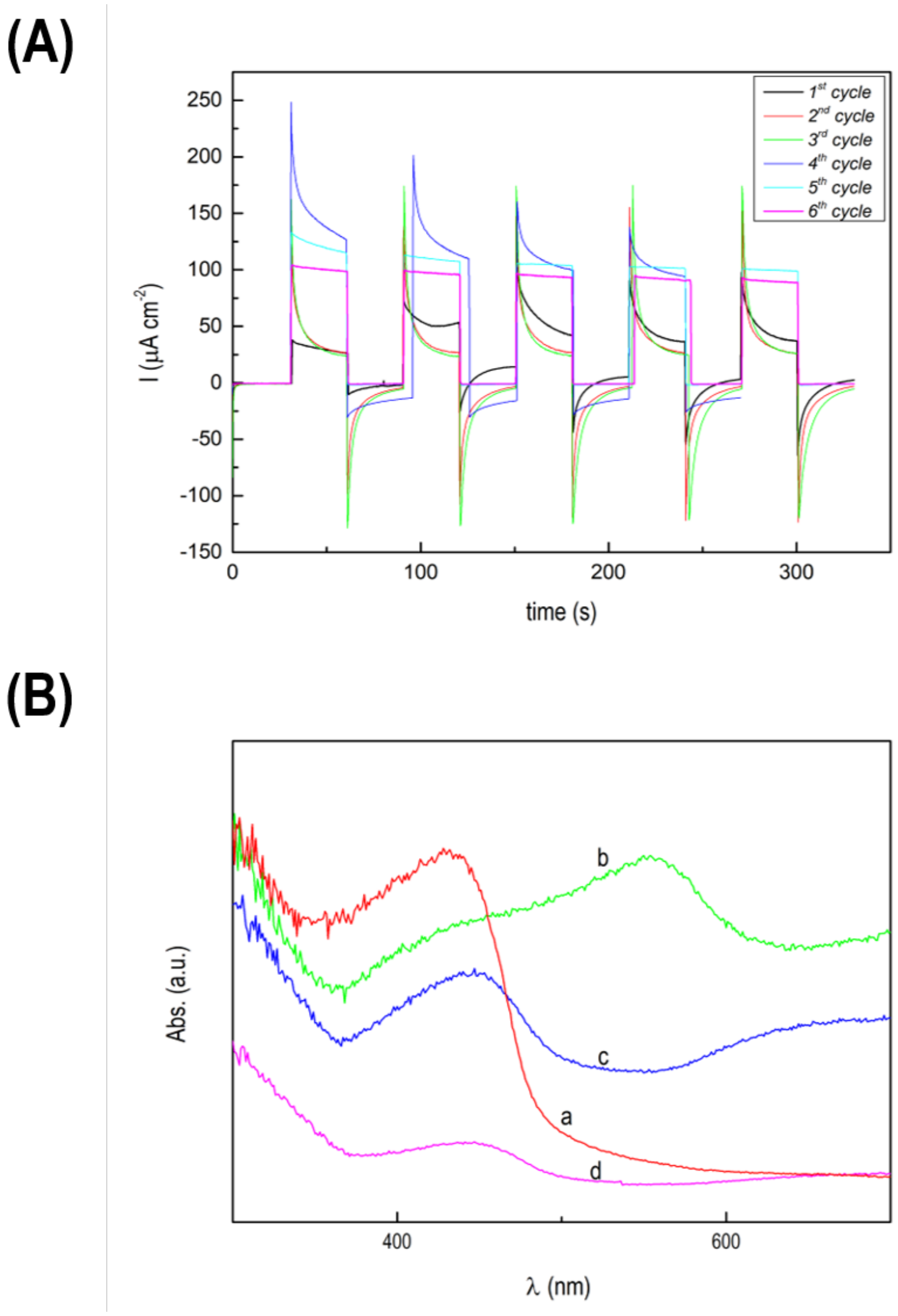

Figure 6.33 - OCP stabilization for dark LSV treated sample: A) Photocurrent registered during the different chopped light cycles (100 mW·cm^{-2}) under UV + visible irradiation. B) Equivalent absorption spectra of: Ti/TiO$_2$/Cu$_2$O as synthesized (a, red line); Ti/TiO$_2$/Cu$_2$O after dark LSV treatment (b, green line); Ti/TiO$_2$/Cu$_2$O dark treated after 3 photocurrent cycles (c, blue line); Ti/TiO$_2$/Cu$_2$O dark treated after OCP stabilization (d, magenta line).

Once the OCP stability was reached, the measured photocurrents were compared with the photocurrents generated with electrodes that were not post-treated (Figure 6.34). The electrodes produced by the post-treatment exhibit, after OCP stabilization and irrespective of the performed LSV (dark, lighted or double) larger photocurrents with respect to both the bare Ti/TiO_2 and to the as synthesized Ti/TiO_2/Cu_2O. Further, comparable photocurrents are attained with different post-treatments.

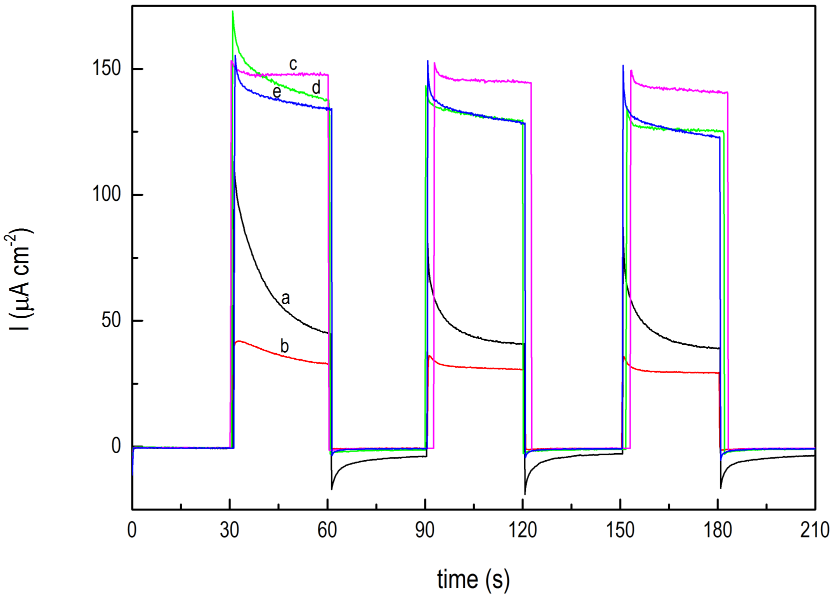

Figure 6.34 - Photocurrent registered after OCP stabilization, under chopped light irradiation (100 mW·cm^{-2}) for LSV treated composite electrode. All the photocurrent tests were performed under UV + visible irradiation. Ti/TiO_2 electrode not treated (b, red line); composite Ti/TiO_2/Cu_2O electrode not treated (a, black line); composite electrode dark LSV treated (e, blue line); composite electrode lighted LSV treated (d, green line); composite electrode double LSV treated (c, magenta line).

The FE-SEM images and the absorption spectra of the treated electrodes after OCP stabilization are reported in Figures 6.35 and 6.36, respectively. The absorption spectra show a similar trend for all the post-treated samples after the OCP stabilization. As previously mentioned for the samples treated by dark LSV, although the absorption spectra at the end of the treatment would indicate the formation of Cu_xO species, with a concomitant improved absorption in the visible region, after the OCP stabilization, the original absorption spectrum is recovered, where the visible absorption can be attributed to the electrodeposited Cu_2O (Figure 6.36). Hence, the formation of Cu_xO species cannot justify the improved performances of the post-treated electrodes.

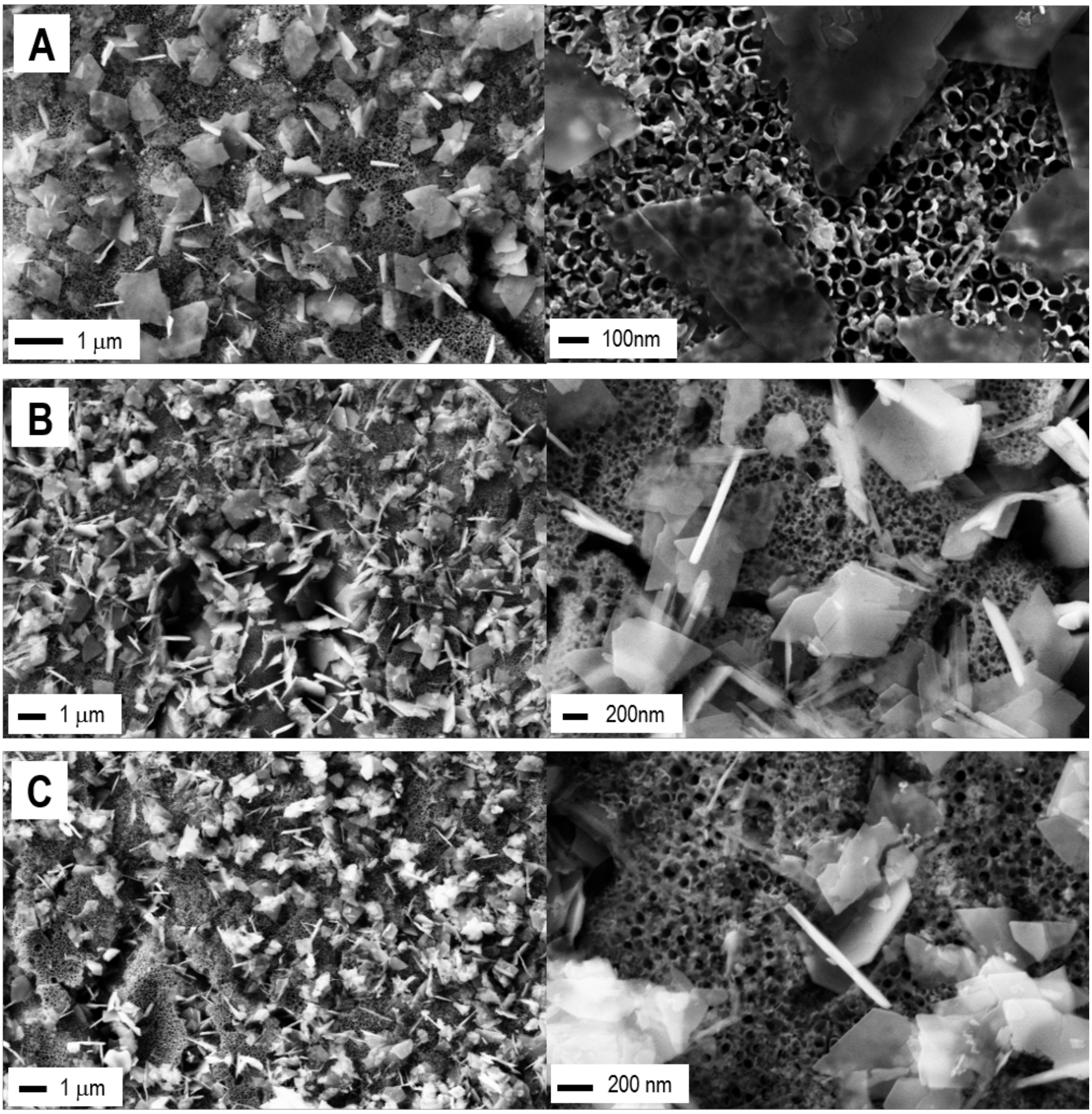

Figure 6.35 - FE-SEM images of composite electrodes (Ti/TiO$_2$/Cu$_2$O) after LSV post-treatment and OCP stabilization: A) dark LSV; B) lighted LSV; C) double LSV (1st scan dark, 2nd scan lighted).

Valuable insight into the mechanisms determining the improved performances can be derived by the analysis of FE-SEM images taken after the photocurrent experiments. As shown in Figure 6.35, for all the post-treated electrodes, a new leaf-like morphology appears after OCP stabilization, with the planar leaf apparently characterized by a thickness of few nanometers. This corroborates the hypothesis that the main effect of post-treatment is to enable the transition to deposits characterized by reduced thickness.

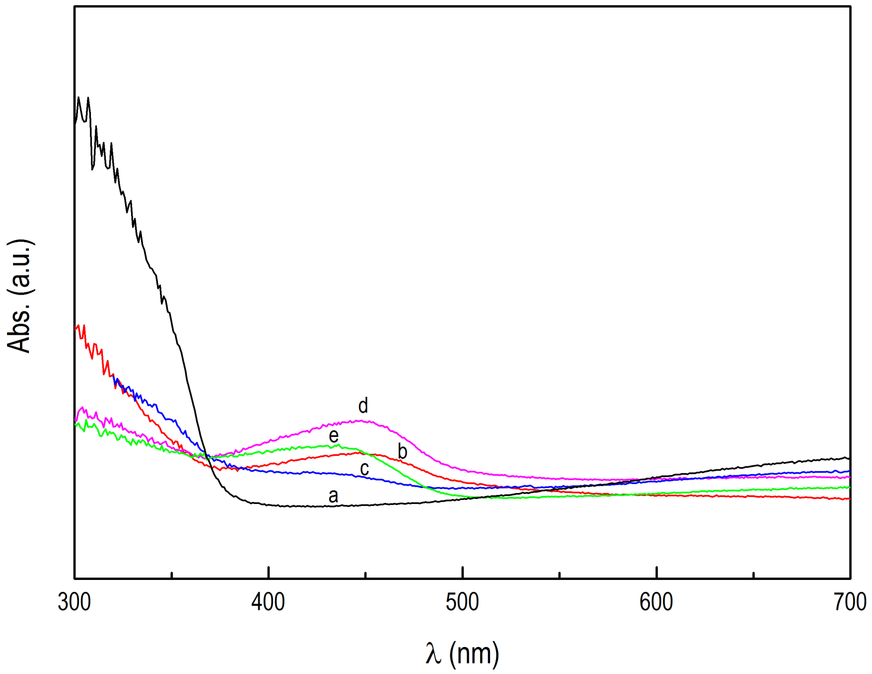

Figure 6.36 - Equivalent absorption spectra after photocurrent tests. Ti/TiO_2 electrode annealed (a, black line); Ti/TiO_2/Cu_2O electrode not treated (b, red line); Ti/TiO_2/Cu_2O electrode dark LSV treated (d, magenta line); Ti/TiO_2/Cu_2O electrode light LSV treated (c, blue line); Ti/TiO_2/Cu_2O electrode double LSV treated (e, green line).

In accordance with the discussion reported in section 6.5.1, this reduced thickness can allow decreasing the energy barrier at the interface between Cu_2O and TiO_2. In addition, it can increase the contact area between the TiO_2 and the Cu_2O, which can enhance the separation of photogenerated electrons and holes. This analysis corroborates the hypothesis that the lower performances of the composite electrode as compared to the bare Ti/TiO_2 electrode could be attributed to the exceedingly large size of the electrodeposited Cu_2O particles.

6.5.2.4 Analysis of the mechanisms governing the formation of Cu_2O leaf-like structures: influence of potential and illumination

Tsui and Zangari reported on the formation of similar leaf-like structures during the cyclic voltammetry (CV) of p-Cu_2O electrodeposited onto an Au foil under UV + visible light [109]. In this latter study, the morphology transition was explained by the Cu_2O tendency (under illumination) to expose the more stable facets via surface diffusion [109]. During tests based on repeated CV cycles under UV+visible light, they observed an increase in the photogenerated currents up to 20 CV cycles, while further CV cycles decreased the photocurrent to the initial values. It is interesting to notice that, during the repeated CV experiments, they didn’t observe differences between the oxidation peaks of the voltammograms generated under light irradiation and under dark conditions. This is in contrast with the present study where a fourth oxidation peak, undetected during the dark LSV, was generated by potential scanning under UV + visible light, i.e. during the lighted LSV (Figure 6.30). This difference could be partly justified by the different substrate employed in the present study as compared to ref. [109]. In the present study, the p-Cu_2O forms a p-n heterojunction with the TiO_2 substrate and, as discussed above, on the basis of the PL-LSV carried out under UV + visible and only visible irradiation (Figure 6.23 and 6.24), we attributed the fourth oxidation peak arising under UV+Visilble light to the synergistic effect of applied potential and photogenerated holes, specifically, the holes photogenerated in the n-TiO_2 side transferred through the heterojunction to Cu_2O.

Inspired by the study performed with Cu_2O on the Au substrate by Tsui and Zangari [109], in order to get further insight into the mechanisms driving the transition to leaf-like structures, the effect of repeated CV and LSV on the morphology of the synthesized Ti/TiO_2/Cu_2O electrodes was here analyzed. The repeated LSV was performed to directly evaluate the effect of the successive potential scans on the electrode morphology as compared to the previously analyzed lighted, dark and double LSV, which included a unique potential scan. In order to analyze the role played by electrode polarization and irradiation on the transition to leaf-like structures, CV experiments were separately performed in dark and under illumination.

The first set of repeated CV was carried out in dark over the potential range investigated by Tsui and Zangari [109], i.e., between -0.5 and 0.5 V (vs. Ag/AgCl). This can allow comparing the results with data reported by Tsui and Zangari [109], and thus evaluating whether the TiO_2 NTs substrate employed in the present study, which was absent in ref. [109], could contribute to the formation of Cu_2O leaf structures.

In Figure 6.37, the current-potential curves and the FE-SEM image generated by 70 successive CV cycles of a composite electrode (Short NTs; 120 mC) starting from 0 V (Vs. Ag/AgCl) in Na_2SO_4 0,01 M are shown.

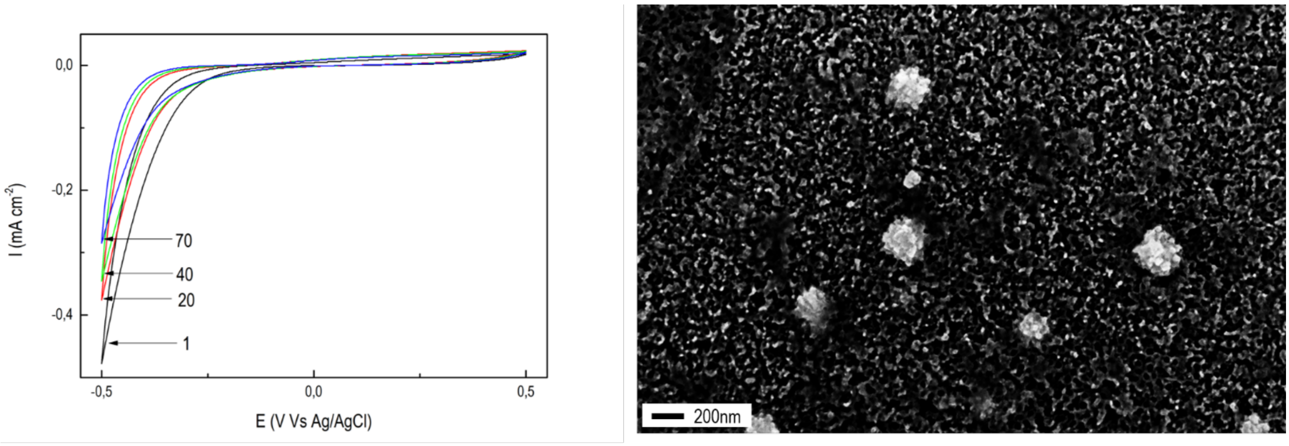

(A) **(B)**

Figure 6.37 – A) Repeated CV (70 cycles); B) FE-SEM image of the treated sample after 70 cycles.

As the FE-SEM image shows (Figure 6.37, B), the main effect of the CV in dark is a transition from octahedral NPs to new clusters characterized by increased dimensions. The eroded spherical morphology of these clusters can be attributed to the Cu_2O rearrangement during the recrystallization. However, no evidence of leaf-like structure formation is observed, in contrast with the results reported by Tsui and Zangari [109].

In order to further characterize the effect of potential cycling, the performed CVs were repeated in dark over a wider potential range (Figure 6.39). Particularly, the potential range previously selected to perform lighted, dark and double LSV was selected, i.e. between -1.5 and 1.5 V (vs. Ag/AgCl). The investigation was carried out varying the number of performed CV cycles.

FE-SEM images reported in Figure 6.38, A, B and C, show the Cu_2O deposit morphologies after 20, 40 and 70 CV cycles, respectively. Again, no evidence of the transition to leaf like structures is observed. The main evidence is the Cu_2O rearrangement from NPs (Figure 6.38 A and B) to agglomerates of 1D nanorods (Figure 6.38 B and C).

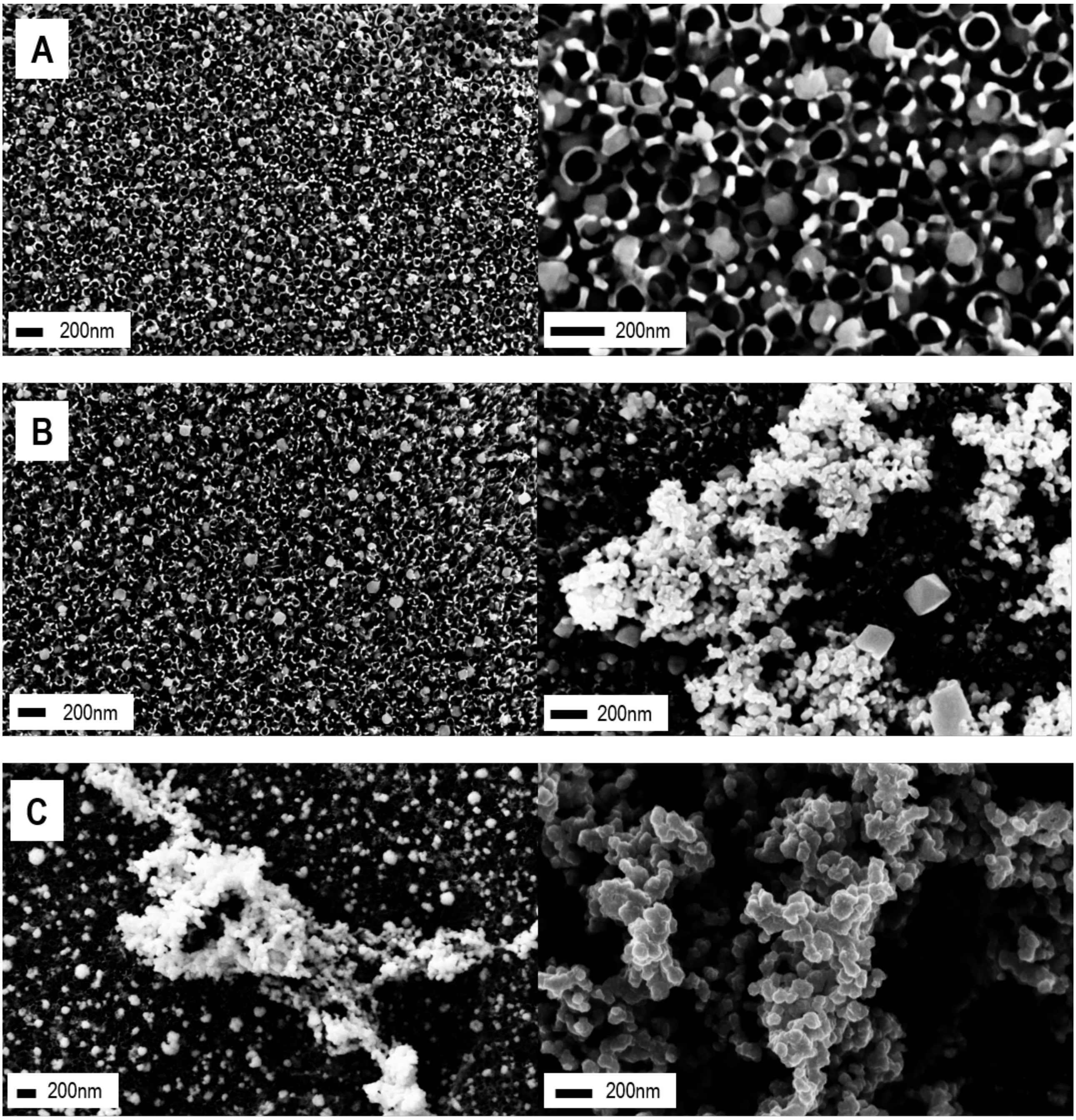

Figure 6.38 – FE-SEM images of the samples treated through repeated CV. A) 20 cycles; B) 40 cycles and C) 70 cycles. Each treated sample is represented at two levels of magnification.

This analysis suggests that the transition of Cu_2O particles to leaf like structured may be, on TiO_2 nanotubes, strictly connected to the effect of the irradiation, specifically, to the photogenerated charge carriers, as it was previously evidenced during the PL-LSV (Figure 6.23) carried out in the present work.

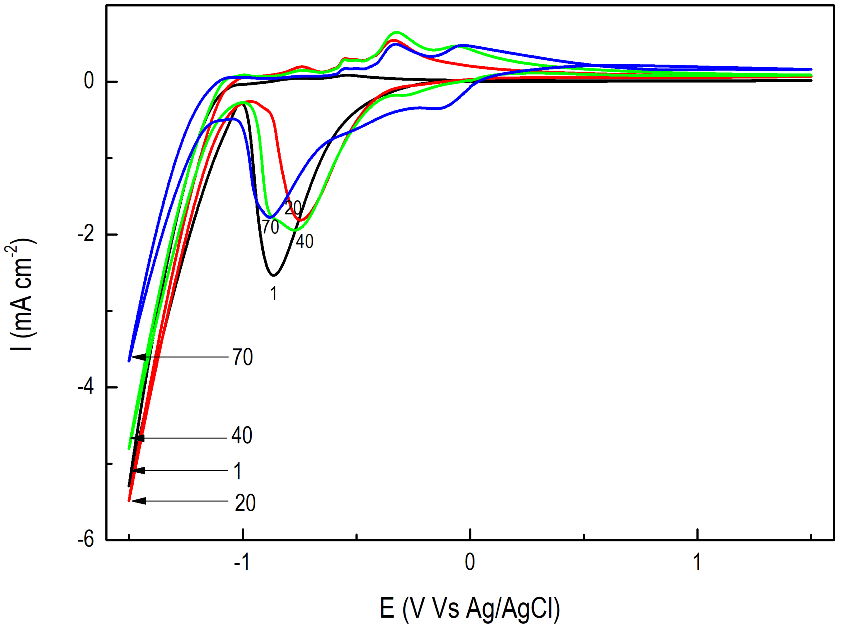

Figure 6.39 – Repeated CV related to a sample treated for 70 cycles.

To verify this hypothesis, samples employed in PL-LSV photoelectrochemical characterization, which was performed under UV + visible (Figure 6.23, b) and only visible irradiation (Figure 6.24, b), were characterized by FE-SEM analysis (Figure 6.40).

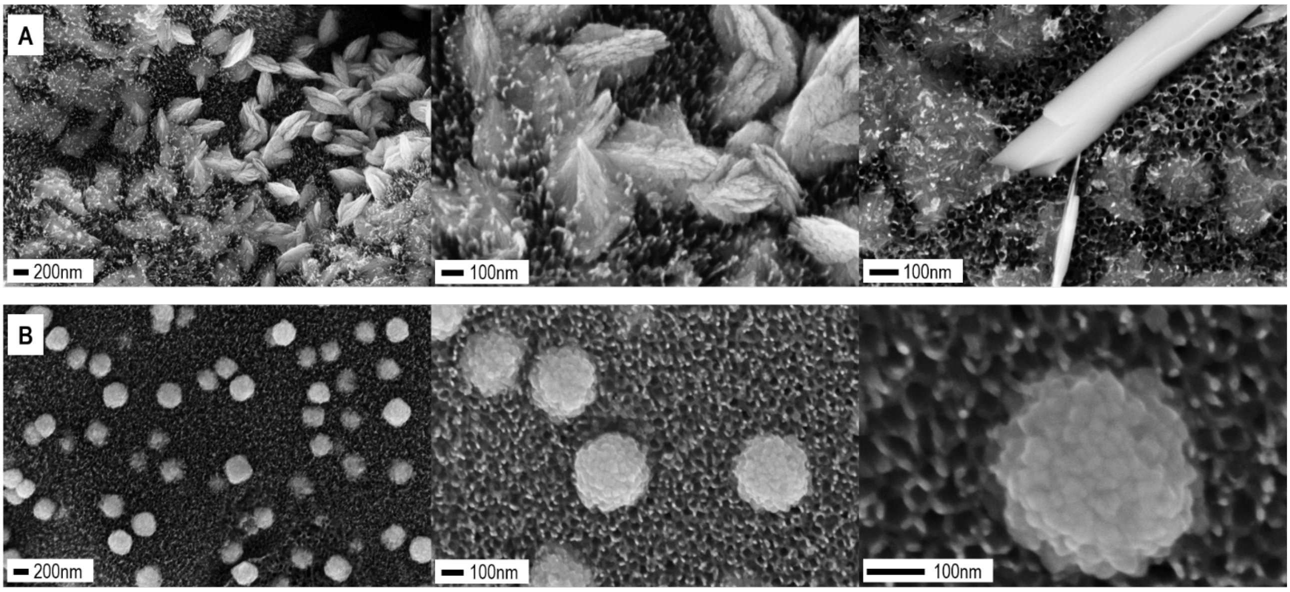

Figure 6.40 - FE-SEM images of the samples characterized through a PL-LSV scan. A) under UV + visible irradiation (100 mW cm^{-2}) and B) under only visible irradiation (100 mW cm^{-2}). Each sample is represented at three levels of magnification.

As shown by the FE-SEM images (Figure 6.40), the sample produced after one PL-LSV scan under UV + visible irradiation (Figure 6.40, A) is indeed characterized by the formation of the planar leaf structures.

The images collected for the samples characterized under only visible light shows a different cauliflower-like morphology (Figure 6.40, B). This morphology is more similar to the clusters formed during repeated polarization (Figure 6.37), which are characterized by increased dimensions with respect to the starting NPs and by an eroded morphology. In this case, the recrystallization of the Cu_2O NPs can thus be mainly attributed to polarization rather than to the interplay between polarization and illumination.

Based on this evidence, a different post treatment was developed in order to achieve the direct transition to leaf like morphologies and prevent the OCP stabilization, which was required during the photoelectrochemical tests performed after lighted, dark and double LSV. The treatment consists of repeated PL-LSV up to 60 cycles in the potential range between 0 and 1.5 V (vs. Ag/AgCl) under UV + visible light (100 mW cm^{-2}). Figure 6.41 shows the FE-SEM images of the electrodes produced by this post-treatment. A transition of Cu_2O from NPs to leaf like structures is observed, according to the hypothesis of a synergistic role played by applied potential and illumination. This treatment was performed on two different series of Short NTs electrodes, characterized by different amounts of deposited Cu_2O. The potentials imposed during the treatment fall within the range ensuring forward bias polarization of the p-Cu_2O/n-TiO_2 photoanode, and UV + visible light was used, according with the assumption that the synergistic effect of the irradiation was attributed to the generation of holes in TiO_2 side of the junction.

Figure 6.42 shows the PL-LSV scans obtained with the Short NTs characterized by the lowest (10 mC; Figure 6.42, A) and highest (120 mC; Figure 6.42, B) amount of Cu_2O deposited during the electrodeposition. With both the electrodes, the photocurrent increases with increasing the number of PL-LSV scans. Particularly, no decrease in the photocurrent response was observed over the performed cycles, in contrast to what reported by ref. [109].

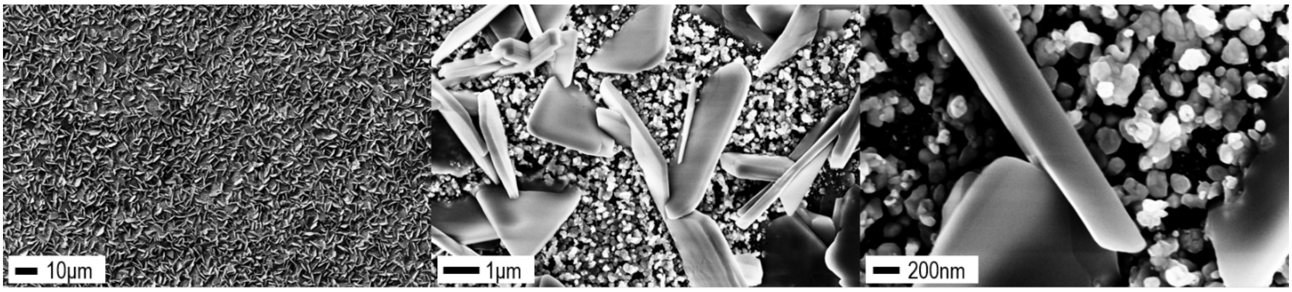

Figure 6.41 - FE-SEM images of the sample treated through repeated PL-LSV, carried out in the potential range between 0 and 1.5 V Vs Ag/AgCl for 60 cycles under UV + visible light (100 mW cm^{-2}). The sample is represented at three levels of magnification.

The evolution of the photocurrent during the performed cycles quantitatively varies with the amount of Cu_2O previously deposited over the electrode. With the lower Cu_2O content, the photocurrent is higher during the first cycle, but it then increases during the successive polarization cycles more slowly as compared to the electrode with the higher Cu_2O content. With the higher Cu_2O content, increasing the number of scans the photocurrent more rapidly increases and eventually attain a stable value which is larger than that attained with the lower Cu_2O content.

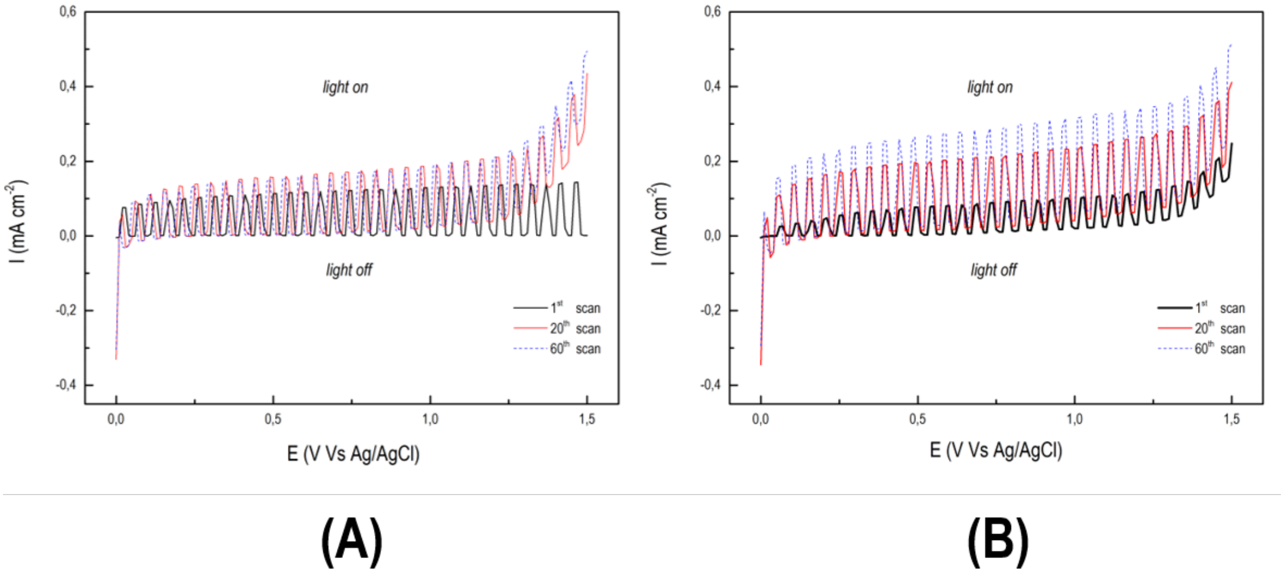

Figure 6.42 - Repeated PL-LSV carried out in the potential range between 0 V and 1.5V Vs Ag/AgCl for 60 cycles under UV + visible light (100 mW cm^{-2}). A) Short NTs, 10 mC and B) Short NTs, 120 mC.

Furthermore, comparing the first cycles of the two electrodes, lowest Cu_2O contents show higher photocurrent densities. This is in line with the trend observed during the photodegradation experiments (Paragraph 6.5.1), where deteriorating performances was observed increasing the

Cu_2O NPs sizes (Figure 6.18, A), to further support of the hypothesis on the deteriorating performances due to exceedingly sizes of the deposits, which was been at the basis of the wide discussion addressed above.

6.6 Electrodialytic Remediation employing TiO_2 electrocatalysts

The experiments described below were carried out in three compartment (3C) electrodialytic cells developed by CENSE (Center for environmental and sustainability research) researchers of NOVA University of Lisbon, within the *e.THROUGH* (Thinking rough towards sustainability) European Union's Horizon 2020 project under the Marie Skłodowska-Curie grant agreement No. 778045 (H2020-MSCA-RISE-2017-778045).

As reported from several authors among the available literature, ED remediation treatments are generally carried out employing commercial electrodes (metal and/or metal oxides based), like Ti/MMO (Mixed Metal Oxides), for both, anode and cathode [118], [123]–[125].

In the present study the possibility to employ non-commercial TiO_2 based electrocatalyst as cathodic materials, characterized by high aspect ratio, was investigated. All the experiments illustrated below were carried out employing the electrodes of the Short NTs series identified as Anatase TiO_2 and Black TiO_2.

Prior to employ the synthesized electrodes in ED remediation processes, a set of "blank experiments" was carried out in order to have a preliminary comparison on the catalytic activity, in terms of Hydrogen production, between commercial Ti/MMO and non-commercial Ti/TiO_2 NTs cathodes. Besides that, considering the strategy proposed by Magro et al. to minimize the overall process energy cost, which is the critical factor for the real use of these technologies, the produced H_2 would play a key role [122]. They addressed the feasibility (proof-of-concept) of using the H_2 produced by electrochemically-induced remediation as fuel in a proton-exchange membrane fuel cell to produce electrical energy and reduce the overall energy costs of electroremediation processes. So, this set of experiments would guarantee at the same time to have a preliminary indication on the electrocatalyst efficiency in terms of hydrogen production.

Figure 6.43 shows equivalent absorption spectra collected for Black TiO_2 (b, black line) and Amorphous TiO_2 (a, dark yellow line) achieved at the end of the anodization, i.e. prior to the electrochemical reduction for transformation to Black TiO_2. Respect to the Amorphous TiO_2, Black TiO_2 is characterized by a higher absorption in the visible region ($\lambda > 400$ nm).

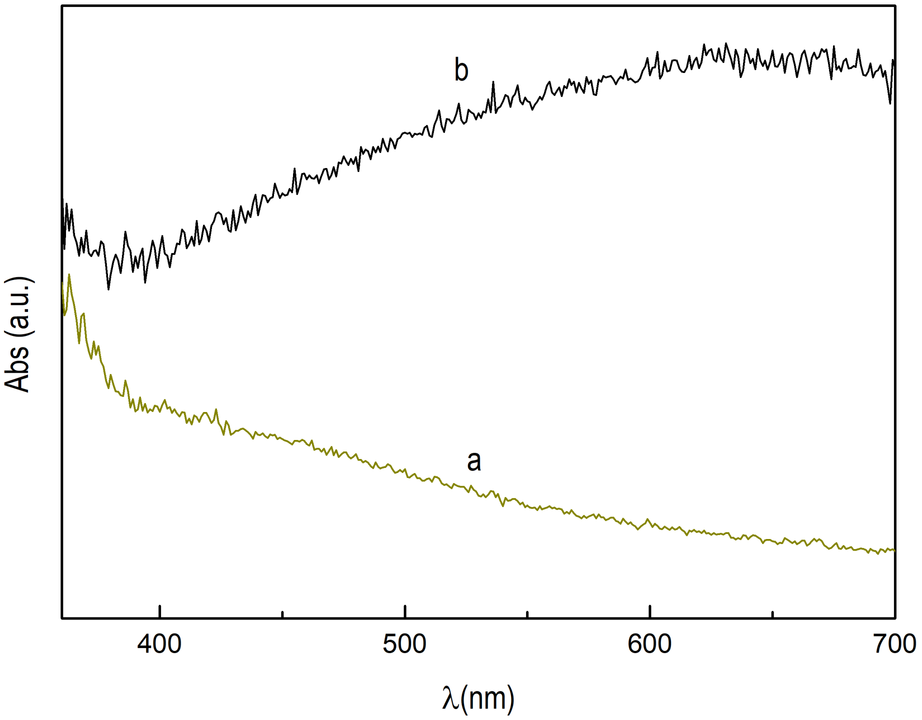

Figure 6.43 – Equivalent absorption spectra from DRS measurements. a) amorphous Ti/TiO_2 NTs (dark yellow line) and b) black Ti/TiO_2 NTs (black line).

As reported by many Authors, this is attributable to the presence of Ti^{3+} states characteristic of Black TiO_2 [169], [170]. Consequence of the Ti^{3+} states is the oxygen vacancies formation. Feng et al. reported on vacancy engineering useful to improve the TiO_2 electrocatalytic performances [140]. Furthermore, metal vacancies can also tune the electronic structure of the surface and improve the catalytic activity [171].

Besides that, it needs to be highlighted that in the experimental conditions of the electrodialytic experiments, amorphous TiO_2 as cathode would anyhow undergo transformation to black TiO_2 through electrochemical reduction in the cathodic compartment [159].

As reported in the diagram of Figure 6.44, black TiO_2 electrode showed the highest H_2 production rate. If compared to anatase TiO_2, the improved performances can be attributed to the above mentioned Ti^{3+} state and the contextual formation of oxygen vacancies, which can effectively tune the electronic properties of the surface, significantly improving the catalytic activity [172].

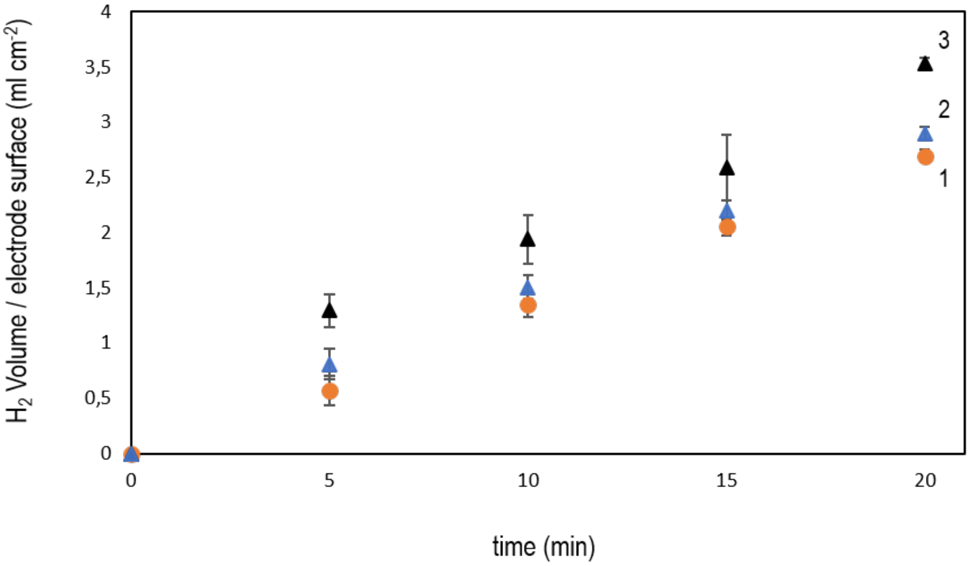

Figure 6.44 – Hydrogen production rate (normalized respect to the cathode surface) of: 1) commercial Ti/MMO; 2) non-commercial anatase TiO_2 NTs and 3) non-commercial "black TiO_2" NTs.

It is interesting to notice that Ti/MMO electrode shows lower performances respect both TiO_2 NTs based electrodes. This could be explained considering that Ir/Ru-based oxides which characterize the coating of the commercial Ti/MMO electrode, to date are the benchmark catalysts for OER, while for HER the benchmark is represented by Pt-group metals based electrocatalysts [128]. Although the employment of TiO_2 based electrodes as HER catalyst, would seem in contrast with the just defined benchmark, the same Authors clarify that benchmark doesn't take in account the pH influence, which otherwise could be a critical factor in electrodialytic water splitting considering the alkalization of the cathodic compartment during the current flow.

Based on the preliminary tests performed, black TiO_2 electrocatalysts were employed as cathodes in MTAW (Mine Tailings As W) remediation. This activity was carried out within e.Through project, which has the goal to tackle the EU dependency from Critical Raw Materials (CRMs), through strategies based on sustainable primary mining, recovery from secondary resources and recycling. Specifically, considering that MT are usually stored in open dumps with consequent environmental problems, the electrodialytic remediation approach could contextually guarantees the effectiveness of the remediation process and the exploitation of that mine residues as secondary source of CRMs.

The experiments were carried out employing as matrixes to treat Panasqueira mine residues from Covilhã (Portugal), which is an underground mine and one of the main Sn-W deposits in Europe. Panasqueira mine have a secondary production of copper. The mine tailings, which are confined in open landfills and contain around 30% of As due to the presence of arsenopyrite, which can cause environmental problems. At the same time these residues, if properly managed, can be seen as a secondary source due to the presence of critical raw materials, such as tungsten.

In this perspective, the objective of the remediation was the contextual recovery of a CRMs, i.e. tungsten, besides the extraction of the arsenic to reduce its concentration to levels which would allow a further reuse of the treated mine residues as inert material for building construction. The effectiveness of the electrodialytic remediation for the contextual recovery of critical raw materials was first investigated by CENSE researchers evaluating the recovery of W, Cu and Sn besides the extraction of As. The present study would be a further preliminary investigation on the employment of electrodic materials which could improve the effectiveness of the remediation process besides the reduction of the overall cost.

Experiments were carried out in two replicates for each condition, both employing black TiO_2 and Ti/MMO as cathodes, fixing the duration of the experiments to 5 days.

Figure 6.45 represents the distribution in the different phases of the investigated metals at the end of the electrodialytic process. The related concentrations are reported in Table 6.5 and 6.6, for "black TiO_2" and Ti/MMO respectively. The legend of the analysed samples reported in Tables is explicated in paragraph 3.5.

Prior to compare the results, for a facile analysis, “solid phase MTAW” must be intended as residual concentrations in the treated matrix, while the sum of the other components would represent the concentrations removed. Furthermore, in reason of the high heterogeneity of the MTAW in terms of composition, as start concentrations were assumed the sum of the concentrations estimated in the different phases at the end of the experiments for each element.

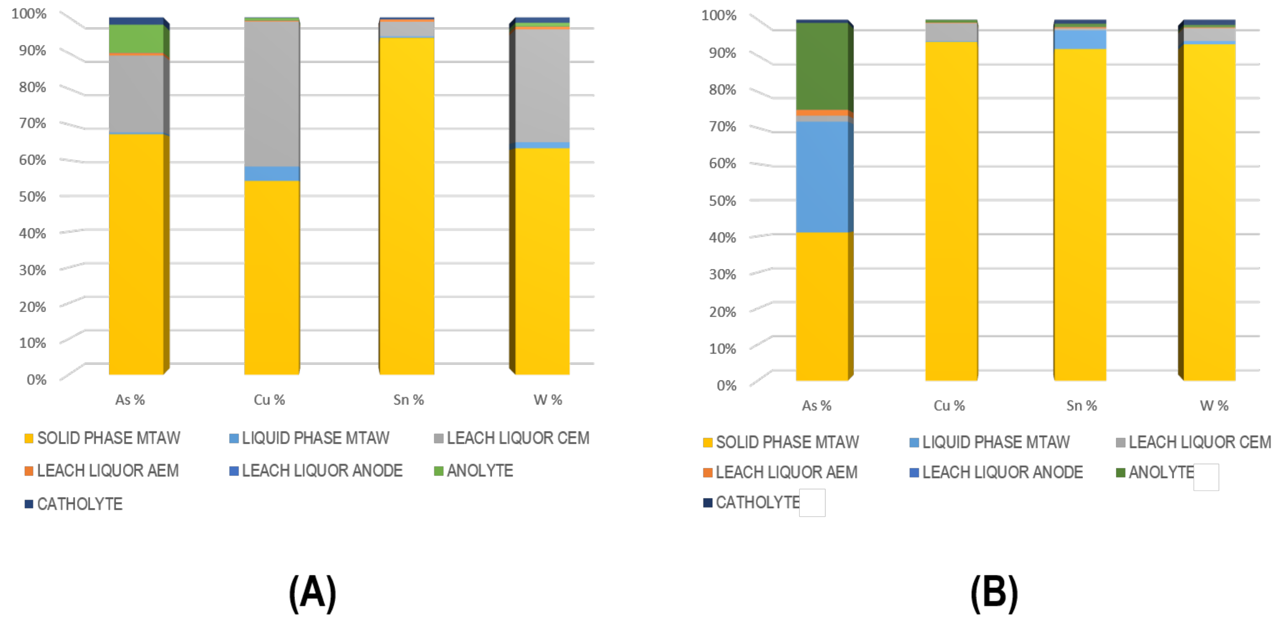

Figure 6.45 – Bar diagrams. Percentage distribution in the different phases of the investigated metals at the end of the electrodialytic treatment: A) employing “Black TiO_2”, and B) employing Ti/MMO. The legend is explicated in paragraph 3.5.

As diagrams report, experiments carried out employing black TiO_2 showed higher mobilization of Cu and W species respect to Ti/MMO, which on the contrary showed a higher extraction of As species.

Table 6.5 – Concentrations of the investigated metals at the end of the electrodialytic remediation experiments carried out employing “black TiO_2” as cathode

	As (mg/Kg)	s.d. (mg/Kg)	Cu (mg/Kg)	s.d. (mg/Kg)	Sn (mg/Kg)	s.d. (mg/Kg)	W (mg/Kg)	s.d. (mg/Kg)
LEACH LIQUOR ANODE	1,22	1,15	0,41	0,58	0,01	0,01	0,03	0,04
LEACH LIQUOR AEM	18,40	14,78	2,17	0,78	0,32	0,22	0,68	0,17

LEACH LIQUOR CEM	530,99	211,69	395,67	133,39	2,04	0,37	27,58	4,14
SOLID PHASE MTAW	1710,90	447,10	517,86	62,35	47,09	0,26	55,15	0,49
LIQUID PHASE MTAW	11,33	1,69	35,88	21,82	0,18	0,19	1,45	1,20
ANOLYTE	193,12	81,16	6,94	0,18	0,00	0,00	0,92	0,29
CATHOLYTE	55,43	74,08	1,53	1,52	0,29	0,34	1,34	0,73
Total	2521,40	243,66	960,45	173,90	49,94	0,25	87,15	3,60

Table 6.6 - Concentration of the investigated metals at the end of the electrodialytic remediation experiments carried out employing Ti/MMO as cathode

	As (mg/Kg)	s.d. (mg/Kg)	Cu (mg/Kg)	s.d. (mg/Kg)	Sn (mg/Kg)	s.d. (mg/Kg)	W (mg/Kg)	s.d. (mg/Kg)
LEACH LIQUOR ANODE	1,17	0,43	0,05	0,01	0,05	0,01	0,04	0,00
LEACH LIQUOR AEM	51,43	31,59	2,50	0,67	0,23	0,08	0,74	0,39
LEACH LIQUOR CEM	52,71	41,84	84,91	22,52	0,42	0,03	13,49	5,28
SOLID PHASE MTAW	1306,32	816,11	1607,94	119,86	69,04	0,34	352,09	22,24
LIQUID PHASE MTAW	1039,12	599,69	3,17	2,18	4,07	4,59	3,36	1,83
ANOLYTE	821,77	627,26	13,37	7,18	0,70	0,78	2,56	0,38
CATHOLYTE	29,58	0,49	1,00	0,49	0,85	0,18	5,44	5,47
Total	3302,09	337,33	1712,93	102,52	75,35	5,49	377,73	9,68

In Table 6.7 are reported the pH values measured for each compartment prior to start the current flow and at the end of 5 days of experiments carried out employing the two different cathodes.

In agreement with the ED cell configuration (Figure 6.46) the presence of the AEM membrane on the anodic side leads the compartment undergoes to acidification, as well as in reason of the CEM the cathodic compartment undergoes to basification, regardless of the employed cathode. For the central compartment (MTAW), in reason of the ED cell configuration and the non-ideal AEM selectivity, i.e. some H^+ would be free to move from anolyte towards MTAW compartment during the current flow, the decrease of the pH respect to the start value should be take place [119]. Furthermore, the exchange of H^+ ions from the catholyte with other ions through the cation exchange membrane could also contribute to the acidification [173]. They also report on the synergistic effect of this acidification which would contributes to dissolve metals in that compartment.

According to the above mentioned Authors the acidification of the MTAW compartment would be the expected behaviour.

Table 6.7 – pH behavior in the two set of experiments carried out employing different cathodes.

pH	Anolyte	Catholyte	MTAW compartment
Prior to start	5.4	5.4	7.7
End Black TiO_2	1.45	13.6	2.4
End Ti/MMO	1.53	13.4	12.2

As showed in Table 6.7 a strong difference among the experiments in relation to the employed cathode is observed for the MTAW compartment (i.e. central compartment).

In the experiments carried out with Black TiO_2 as cathode, pH decreases according to expected behaviour. On the contrary, employing Ti/MMO as cathode the basification of the MTAW compartment was observed. This difference, regardless of the heterogeneity of the treated matrix which wouldn't justify the increase of the pH respect to the start value, would be better consistent assuming leakages from the cathodic compartment due to a non-perfect assembly of the 3C ED cells (i.e. central compartment and catholyte in contact).

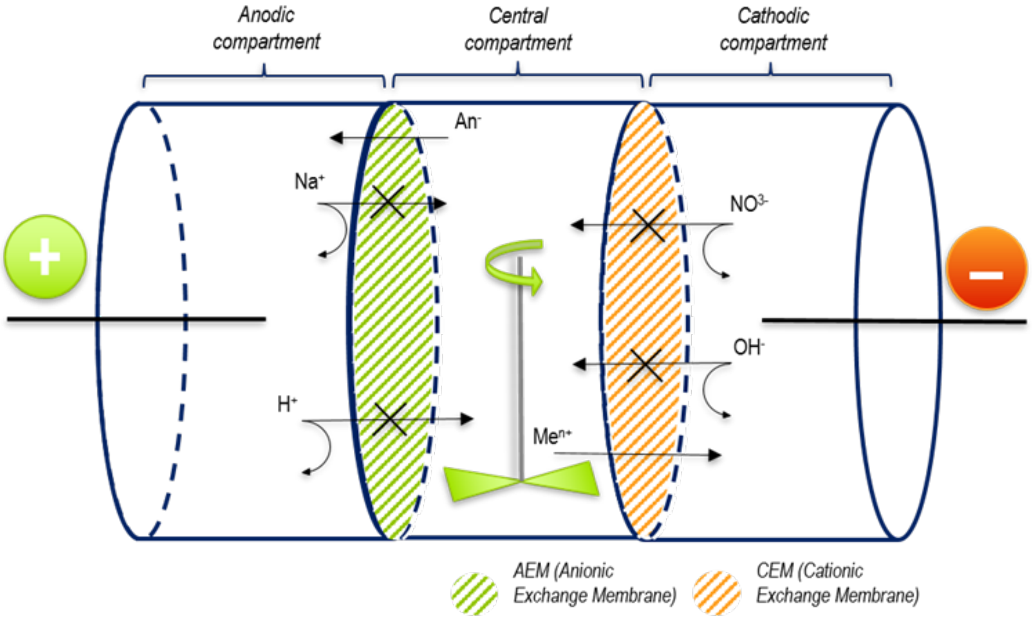

Figure 6.46 - Schematic representation of a 3C ED cell during current flow with $NaNO_3$ as both, anolyte and catholyte. It must to be highlighted that this representation doesn't take in account the non-ideal selectivity (< 100 %) of the AEM membrane.

Nevertheless, due to the heterogeneity of the input tailing and some deficiencies of the experimental apparatus (i.e. not perfect selectivity of AEM, besides possible leakage from cathodic compartment in experiments carried out with Ti/MMO cathodes) no direct relation can be assumed with the used electrodes.

Although this preliminary study would seem encouraging regard the increased activity, both respect the H_2 production rate and the Cu and W recovery, raises some concerns about the different activity regard As species mobilization. As reported by Fernandez et al. [174], the arsenopyrite electrochemical oxidation would be more pronounced in alkali than in acid solutions. This could justify in part the higher extraction observed for arsenic species in the experiment carried out employing Ti/MMO, where the basification of the central compartment was observed.

Given that the reason of the unexpected basification of MTAW, observed employing Ti/MMO cathodes, must be further investigated, these evidences would suggest that for high arsenic extraction a new ED cell design in which both anode and cathode would operate in the same alkali environment could further enhance the effectiveness of the remediation process. Furthermore, considering that in strong acidic media Black TiO_2 could be unstable (i.e. corrosion process), alkali media in both electrodic compartments would allow to employ Black TiO_2 for both, anode and cathode, in a symmetric cell configuration which could further improve the overall process.

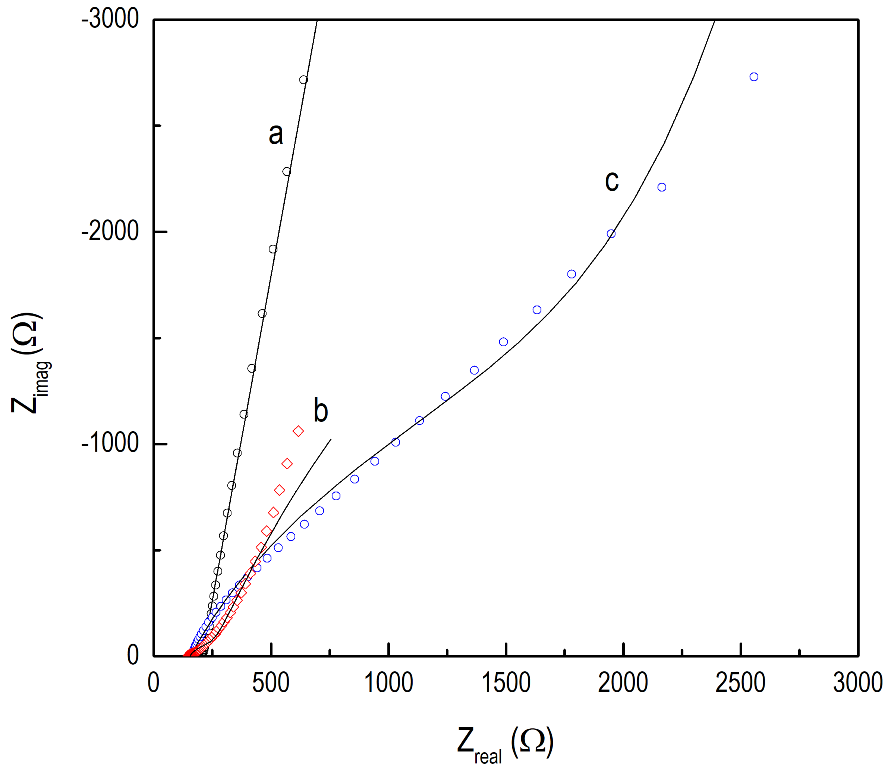

Figure 6.47 – Nyquist plot achieved in Na_2SO_4 for: a) black TiO_2 (black circles); b)Ti/MMO (red circles) and c) anatase TiO_2 . The black lines are the NLLS-fit based on the different equivalent circuit models (data not showed).

Despite these latter considerations, the differences observed, which could be attributed mainly to the high heterogeneity of the matrix, as well as to leakages in the 3C ED systems, would suggest that an experimental campaign with a higher number of tests would be required.

At last, to further support the potential of black TiO_2 electrocatalyst synthesized, the three different electrodes employed in the above mentioned experiments were characterized through Electrochemical Impedance Spectroscopy (EIS). Figure 6.47 report the related Nyquist plot.

The qualitative analysis of the curves already shows as the electrode characterized by the higher resistance to charge transfer (estimated parameters through the equivalent circuit models not showed) is the anatase TiO_2 (Figure 6.47, blue circle), which shows also a diffusive contribution to the curve in the low frequency region. Ti/MMO is characterized by a lower resistance to charge transfer (high frequency region) respect to anatase TiO_2 but also here a diffusive contribution would be hypnotizable (low frequency region). Black TiO_2 indeed show a different behaviour, typical of a porous polarizable electrode, without charge transfer resistance. This latter aspect would be particularly appealing considering that prevents collateral electrodeposition when it is employed as cathode, and consequently no regeneration of the electrodes would be requested. To this purpose further characterizations of the cathodes should be performed in future experimental campaign.

Besides that, as showed in previous section, considering that the non-commercial synthesized electrodes could be further functionalized through the electrodeposition of suitable co-catalysts, future studies could be focused in this direction to further improve the catalytic performances and as consequence the overall effectiveness of the process.

On these bases, the improved performances in terms of H_2 production rate and W and Cu extractions, would need to be evaluated in terms of reduced energy costs and economic added value respectively, through a life cycle assessment study in comparison with the actual benchmarks.

Conclusions

The electrochemical synthesis of TiO_2 NTs based electrodes was investigated. A novel one-step anodization method was preliminarily developed to synthesize Ti/TiO_2 NTs electrodes starting from Ti sheets, with NTs length varying from about 100 nm up to 10 µm. With the proposed method, TiO_2 nanotube arrays are directly produced by a unique anodization, thus considerably improving process sustainability as compared to the traditional synthesis process including the sequence of two anodizations separated by the dissolution of the first formed TiO_2 NTs. Particularly, the following difficulties encountered in the synthesis TiO_2 nanotubes with length around 10 µm and lower than 2 µm, respectively, were solved:

- Long NTs (length ≈ 10 µm; inner tube diameter ≈ 100 nm). A sonication post-treatment was optimized to remove the nanograss generated by the collapse of the top TiO_2 nanotube sections during anodization.
- Short NTs (length < 2 µm; inner tube diameter > 50 nm) with clearly accessible pores could be produced by simultaneously modifying the water content and slope of the potential ramp imposed during the early anodization stage.

Thermal annealing was then optimized to ensure almost complete transition to the Anatase TiO_2 (%Rutile < 5 %), which is the most photoactive phase.

Cu_2O electrodeposition over TiO_2 nanotubes was investigated to enable the light absorption across the visible region of the solar spectrum for the visible-inactive TiO_2. The influence of electrodeposition potential and overall transferred charge on the size and morphology of the Cu_2O nanoparticles was evaluated. This analysis evidenced a transition from octahedral to rounded spherical particles with increasing the cathodic electrodeposition potential and a progressive increase in the Cu_2O particle size with increasing the transferred charge. The produced electrodes were employed as photocatalyst to sustain the methylene blue photodegradation, and as photoanodes in a photoelectrochemical cell designed for water splitting process.

In the photodegradation experiments performed under UV + visible light, the composite Ti/TiO_2/Cu_2O exhibited performances lower as compared to the bare Ti/TiO_2 electrode.

Particularly, composite electrode performances decreased with increasing the size of the Cu_2O nanoparticles. Cu_2O octahedral nanoparticles exhibited improved performances as compared to the spherical nanoparticles.

Photoelectrochemical experiments were performed under UV + visible and only visible light irradiation. The composite electrodes could effectively work as photoanodes under visible light only. This confirmed the absorption across the visible range induced by Cu_2O deposition and the ability of the Cu_2O/TiO_2 heterojunction to effectively separate photogenerated holes and electrons. However, under UV + visible light, the photocurrent generated with the composite electrode was lower than with the bare TiO_2 electrode, thus confirming the results of the previous photo-degradation experiments.

It is hypothesized that the lower performances of the composite electrodes under UV + visible irradiation could be attributed to the exceedingly large size of the electrodeposited Cu_2O nanoparticles. In accordance with this idea, an electrochemical post-treatment was proposed to purposefully modify the size and the morphology of the electrodeposited Cu_2O nanoparticles and thus significantly improve the composite electrode photocatalytic activity. The proposed electrochemical post-treatment includes scanning the electrode potential under UV + visible light irradiation with an electrolyte solution not containing the precursor copper metal ion (i.e. without electrodeposition of any copper species). This post-treatment induced a transition to Cu_2O thin leaf-like structures, which allowed attaining, with the composite electrode, performances improved as compared to the bare TiO_2 electrode under UV + visible light.

The Short NTs were also employed as high aspect ratio HER electrocatalysts in Electrodialytic (ED) remediation processes within the *e.THROUGH* (Thinking rough towards sustainability) European Union’s Horizon 2020 project under the Marie Skłodowska-Curie grant agreement No. 778045 (H2020-MSCA-RISE-2017-778045), at CENSE (Center for environmental and sustainability research) laboratories of NOVA University of Lisbon. Black TiO_2 HER catalysts were successfully synthesized through a facile electrochemical reduction and employed as cathodes in place of the commercial Ti/MMO that are generally employed in ED processes, which resulted into:

- increased H_2 production rate in ED water splitting (H_2 recovery as strategy to minimize the treatment cost)
- Improved recovery of Cu and W in Mine Tailings remediation, while with respect to As extraction showed lower activity in comparison to commercial Ti/MMO. The variability in the composition of the matrix added to experimental issues didn't clarify this behavior.

References

[1] C. N. R. Rao, A. Müller, and A. K. Cheetham, *Nanomaterials Chemistry: Recent Developments and New Directions*. Wiley, 2007.

[2] A. Eftekhari, *Nanostructured Materials in Electrochemistry*. Wiley, 2008.

[3] H. Chik and J. M. Xu, "Nanometric superlattices: Non-lithographic fabrication, materials, and prospects," *Mater. Sci. Eng. R Reports*, vol. 43, no. 4, pp. 103–138, 2004.

[4] S. Y. Chou, P. R. Krauss, P. J. Renstrom, S. Y. Chou, P. R. Krauss, and P. J. Renstrom, "Nanoimprint lithography Nanoimprint lithography," *J. Vac. Sci. Technol. B Microelectron. Nanom. Struct.*, vol. 4129, no. 1996, pp. 9–14, 2014.

[5] P. Tartaj, M. P. Morales, T. González-Carreño, S. Veintemillas-Verdaguer, and C. J. Serna, "Advances in magnetic nanoparticles for biotechnology applications," in *Journal of Magnetism and Magnetic Materials*, 2005, vol. 290-291 PA, pp. 28–34.

[6] B. J. Murray, Q. Li, J. T. Newberg, E. J. Menke, J. C. Hemminger, and R. M. Penner, "Shape- and size-selective electrochemical synthesis of dispersed silver(l) oxide colloids," *Nano Lett.*, vol. 5, no. 11, pp. 2319–2324, Nov. 2005.

[7] Z. Zhao, N. Chamele, M. Kozicki, Y. Yao, and C. Wang, "Photochemical synthesis of dendritic silver nano-particles for anti-counterfeiting," *J. Mater. Chem. C*, vol. 7, no. 20, pp. 6099–6104, 2019.

[8] D. P. MacWan, P. N. Dave, and S. Chaturvedi, "A review on nano-TiO2 sol-gel type syntheses and its applications," *Journal of Materials Science*, vol. 46, no. 11. pp. 3669–3686, Jun-2011.

[9] S. P. Jiang, "A review of wet impregnation - An alternative method for the fabrication of high performance and nano-structured electrodes of solid oxide fuel cells," *Mater. Sci. Eng. A*, vol. 418, no. 1–2, pp. 199–210, Feb. 2006.

[10] P. G. Schiavi, P. Altimari, A. Rubino, and F. Pagnanelli, "Electrodeposition of cobalt nanowires into alumina templates generated by one-step anodization," *Electrochim. Acta*, vol. 259, pp. 711–722, Jan. 2018.

[11] D. Fang, K. Huang, S. Liu, and D. Qin, "High density copper nanowire arrays deposition inside ordered titania pores by electrodeposition," *Electrochem. commun.*, vol. 11, no. 4, pp. 901–904, Apr. 2009.

[12] J. M. Macak, B. G. Gong, M. Hueppe, and P. Schmuki, “Filling of TiO2 nanotubes by self-doping and electrodeposition,” *Adv. Mater.*, vol. 19, no. 19, pp. 3027–3031, 2007.

[13] A. Huczko, “Template-based synthesis of nanomaterials,” *Appl. Phys. A Mater. Sci. Process.*, vol. 70, no. 4, pp. 365–376, 2000.

[14] A. Milchev, *Electrocrystallization*. Boston: Kluwer Academic Publishers, 2002.

[15] P. G. Schiavi, P. Altimari, R. Zanoni, and F. Pagnanelli, “Morphology-controlled synthesis of cobalt nanostructures by facile electrodeposition: transition from hexagonal nanoplatelets to nanoflakes,” *Electrochim. Acta*, vol. 220, pp. 405–416, Dec. 2016.

[16] P. Altimari, P. G. Schiavi, A. Rubino, and F. Pagnanelli, “Electrodeposition of cobalt nanoparticles: An analysis of the mechanisms behind the deviation from three-dimensional diffusion-control,” *J. Electroanal. Chem.*, vol. 851, p. 113413, 2019.

[17] K. Vignarooban *et al.*, “Nano-electrocatalyst materials for low temperature fuel cells: A review,” *Cuihua Xuebao/Chinese Journal of Catalysis*, vol. 36, no. 4. Science Press, pp. 458–472, 20-Apr-2015.

[18] A. Nakajima, A. Nakamura, N. Arimitsu, Y. Kameshima, and K. Okada, “Processing and properties of transparent sulfated TiO2 thin films using sol-gel method,” *Thin Solid Films*, vol. 516, no. 18, pp. 6392–6397, 2008.

[19] L. V. Taveira, J. M. Macák, H. Tsuchiya, L. F. P. Dick, and P. Schmuki, “Initiation and Growth of Self-Organized TiO[sub 2] Nanotubes Anodically Formed in NH[sub 4]F⁄(NH[sub 4])[sub 2]SO[sub 4] Electrolytes,” *J. Electrochem. Soc.*, vol. 152, no. 10, p. B405, 2005.

[20] M. Ikraam, S. Shahid, S. Zaman, and M. N. Sarwar, “Fabrication and Characterization of TiO2 Nano Rods by Electrochemical Deposition into an Anodic Alumina Template,” *J. Electron. Mater.*, vol. 45, no. 8, pp. 4228–4236, Aug. 2016.

[21] R. Vijaya Kumar, Y. Diamant, and A. Gedanken, “Sonochemical synthesis and characterization of nanometer-size transition metal oxides from metal acetates,” *Chem. Mater.*, vol. 12, no. 8, pp. 2301–2305, 2000.

[22] Q. Chen, W. Zhou, G. H. Du, and L. M. Peng, “Trititanate nanotubes made via a single alkali treatment,” *Adv. Mater.*, vol. 14, no. 17, pp. 1208–1211, 2002.

[23] S. P. Albu and P. Schmuki, “TiO2 nanotubes grown in different organic electrolytes: Two-size self-organization, single vs. double-walled tubes, and giant diameters,” *Phys. Status Solidi - Rapid Res. Lett.*, vol. 4, no. 8–9, pp. 215–217, Sep. 2010.

[24] J. M. Macak *et al.*, “TiO2 nanotubes: Self-organized electrochemical formation, properties and applications,” *Curr. Opin. Solid State Mater. Sci.*, vol. 11, no. 1–2, pp. 3–18, Feb. 2007.

[25] A. Ghicov, H. Tsuchiya, J. M. MacAk, and P. Schmuki, “Titanium oxide nanotubes prepared in phosphate electrolytes,” *Electrochem. commun.*, vol. 7, no. 5, pp. 505–509, 2005.

[26] P. Roy, S. Berger, and P. Schmuki, “TiO2 nanotubes: Synthesis and applications,” *Angew. Chemie - Int. Ed.*, vol. 50, no. 13, pp. 2904–2939, Mar. 2011.

[27] K. S. Raja, T. Gandhi, and M. Misra, “Effect of water content of ethylene glycol as electrolyte for synthesis of ordered titania nanotubes,” *Electrochem. commun.*, vol. 9, no. 5, pp. 1069–1076, 2007.

[28] C. Dumitriu, C. Pirvu, and I. Demetrescu, “ The Electrochemical Formation and Shielding Mechanism of TiO 2 Nanotubes in Organic Electrolytes with Different Viscosity ,” *J. Electrochem. Soc.*, vol. 160, no. 2, pp. G55–G60, 2013.

[29] C. A. Grimes and G. K. Mor, *TiO2 nanotube arrays: Synthesis, properties, and applications*. 2009.

[30] M. Paulose *et al.*, “TiO 2 nanotube arrays of 1000 μm length by anodization of titanium foil: Phenol red diffusion,” *J. Phys. Chem. C*, vol. 111, no. 41, pp. 14992–14997, 2007.

[31] R. Sánchez-Tovar, I. Paramasivam, K. Lee, and P. Schmuki, “Influence of hydrodynamic conditions on growth and geometry of anodic TiO2 nanotubes and their use towards optimized DSSCs,” *J. Mater. Chem.*, vol. 22, no. 25, pp. 12792–12795, 2012.

[32] S. K. Mohapatra, K. S. Raja, V. K. Mahajan, and M. Misra, “Efficient photoelectrolysis of water using TiO2 nanotube arrays by minimizing recombination losses with organic additives,” *J. Phys. Chem. C*, vol. 112, no. 29, pp. 11007–11012, Jul. 2008.

[33] J. Wang, G. Ji, Y. Liu, M. A. Gondal, and X. Chang, “Cu2O/TiO2

heterostructure nanotube arrays prepared by an electrodeposition method exhibiting enhanced photocatalytic activity for CO2 reduction to methanol," *Catal. Commun.*, vol. 46, pp. 17–21, 2014.

[34] A. Auer and J. Kunze-Liebhäuser, "Recent progress in understanding ion storage in self-organized anodic TiO2 nanotubes," *Small Methods*, vol. 3, no. 8, p. 1800385, 2019.

[35] H. Zhou and Y. Zhang, "Electrochemically self-doped TiO2 nanotube arrays for supercapacitors," *J. Phys. Chem. C*, vol. 118, no. 11, pp. 5626–5636, 2014.

[36] L. K. Tsui and G. Zangari, "Modification of TiO2 nanotubes by Cu2O for photoelectrochemical, photocatalytic, and photovoltaic devices," *Electrochim. Acta*, vol. 128, pp. 341–348, 2014.

[37] M. Ge *et al.*, "A review of one-dimensional TiO2 nanostructured materials for environmental and energy applications," *J. Mater. Chem. A*, vol. 4, no. 18, pp. 6772–6801, 2016.

[38] T. Saboo *et al.*, "Water splitting on 3D-type meso/macro porous structured photoanodes based on Ti mesh," *Sol. Energy Mater. Sol. Cells*, vol. 178, no. January, pp. 98–105, 2018.

[39] V. Malgras *et al.*, "Nanoarchitectures for Mesoporous Metals," *Adv. Mater.*, vol. 28, no. 6, pp. 993–1010, 2016.

[40] V. Zwilling, M. Aucouturier, and E. Darque-Ceretti, "Anodic oxidation of titanium and TA6V alloy in chromic media. An electrochemical approach," *Electrochim. Acta*, vol. 45, no. 6, pp. 921–929, Dec. 1999.

[41] Q. Cai, M. Paulose, O. K. Varghese, and C. A. Grimes, "The effect of electrolyte composition on the fabrication of self-organized titanium oxide nanotube arrays by anodic oxidation," *J. Mater. Res.*, vol. 20, no. 1, pp. 230–236, Jan. 2005.

[42] H. E. Prakasam, K. Shankar, M. Paulose, O. K. Varghese, and C. A. Grimes, "A new benchmark for TiO2 nanotube array growth by anodization," *J. Phys. Chem. C*, vol. 111, no. 20, pp. 7235–7241, 2007.

[43] H. J. Seifert and P. V Nerikar, "208th ECS Meeting, Abstract #1037, copyright ECS," vol. 23, no. 1978, p. 1985, 1985.

[44] X. Chen, M. Schriver, T. Suen, and S. S. Mao, "Fabrication of 10 nm diameter

TiO2 nanotube arrays by titanium anodization," *Thin Solid Films*, vol. 515, no. 24 SPEC. ISS., pp. 8511–8514, Oct. 2007.

[45] J. M. Wu, "Low-temperature preparation of titania nanorods through direct oxidation of titanium with hydrogen peroxide," *J. Cryst. Growth*, vol. 269, no. 2–4, pp. 347–355, Sep. 2004.

[46] N. K. Allam, K. Shankar, and C. A. Grimes, "Photoelectrochemical and water photoelectrolysis properties of ordered TiO2 nanotubes fabricated by Ti anodization in fluoride-free HCl electrolytes," *J. Mater. Chem.*, vol. 18, no. 20, pp. 2341–2348, 2008.

[47] G. K. Mor, O. K. Varghese, M. Paulose, K. Shankar, and C. A. Grimes, "A review on highly ordered, vertically oriented TiO2 nanotube arrays: Fabrication, material properties, and solar energy applications," *Solar Energy Materials and Solar Cells*, vol. 90, no. 14. pp. 2011–2075, 06-Sep-2006.

[48] Y. Y. Song, R. Lynch, D. Kim, P. Roy, and P. Schmuki, "TiO2 nanotubes: Efficient suppression of top etching during anodic growth: Key to improved high aspect ratio geometries," *Electrochem. Solid-State Lett.*, vol. 12, no. 7, p. C17, 2009.

[49] D. Kim, A. Ghicov, and P. Schmuki, "TiO2 Nanotube arrays: Elimination of disordered top layers ('nanograss') for improved photoconversion efficiency in dye-sensitized solar cells," *Electrochem. commun.*, vol. 10, no. 12, pp. 1835–1838, 2008.

[50] J. W. Schultze and M. M. Lohrengel, "Stability, reactivity and breakdown of passive films. Problems of recent and future research," *Electrochim. Acta*, vol. 45, no. 15–16, pp. 2499–2513, May 2000.

[51] M. Christophersen, J. Carstensen, K. Voigt, and H. Föll, "Organic and aqueous electrolytes used for etching macro- and mesoporous silicon," in *Physica Status Solidi (A) Applied Research*, 2003, vol. 197, no. 1, pp. 34–38.

[52] S. P. Albu *et al.*, "Formation of double-walled TiO2 nanotubes and robust anatase membranes," *Adv. Mater.*, vol. 20, no. 21, pp. 4135–4139, Nov. 2008.

[53] L. K. Tsui, T. Homma, and G. Zangari, "Photocurrent conversion in anodized TiO2 nanotube arrays: Effect of the water content in anodizing solutions," *J. Phys. Chem. C*, vol. 117, no. 14, pp. 6979–6989, 2013.

[54] L. Tsui and G. Zangari, "Titania Nanotubes by Electrochemical Anodization for

Solar Energy Conversion," *J. Electrochem. Soc.*, vol. 161, no. 7, pp. D3066–D3077, 2014.

[55] N. Mir, K. Lee, I. Paramasivam, and P. Schmuki, "Optimizing TiO 2 nanotube top geometry for use in dye-sensitized solar cells," *Chem. - A Eur. J.*, vol. 18, no. 38, pp. 11862–11866, 2012.

[56] M. M. Momeni and Y. Ghayeb, "Photoelectrochemical water splitting on chromium-doped titanium dioxide nanotube photoanodes prepared by single-step anodizing," *J. Alloys Compd.*, vol. 637, pp. 393–400, Jul. 2015.

[57] D. Regonini, C. R. Bowen, R. Stevens, D. Allsopp, and A. Jaroenworaluck, "Anodised TiO 2 nano-tubes: Voltage ramp influence on the nano-structured oxide and investigation of phase changes promoted by thermal treatments," in *Physica Status Solidi (A) Applications and Materials Science*, 2007, vol. 204, no. 6, pp. 1814–1819.

[58] A. Rubino, P. G. Schiavi, P. Altimari, and F. Pagnanelli, "Ti/TiO2/Cu2O electrodes for photocatalytic applications: Synthesis and characterization," in *AIP Conference Proceedings*, 2019, vol. 2145, no. August, p. 020005.

[59] Y. X. Leng *et al.*, "Influence of oxygen pressure on the properties and biocompatibility of titanium oxide fabricated by metal plasma ion implantation and deposition," in *Thin Solid Films*, 2002, vol. 420–421, pp. 408–413.

[60] S. Sankar and K. G. Gopchandran, "Effect of annealing on the structural, electrical and optical properties of nanostructured TiO2 thin films," *Cryst. Res. Technol.*, vol. 44, no. 9, pp. 989–994, Sep. 2009.

[61] A. Sasahara, T. C. Droubay, S. A. Chambers, H. Uetsuka, and H. Onishi, "Topography of anatase TiO2 film synthesized on LaAlO 3(001)," in *Nanotechnology*, 2005, vol. 16, no. 3.

[62] A. L. Linsebigler, G. Lu, and J. T. Yates, "Photocatalysis on TiO2 Surfaces: Principles, Mechanisms, and Selected Results," *Chem. Rev.*, vol. 95, no. 3, pp. 735–758, 1995.

[63] S. Yoriya, G. K. Mor, S. Sharma, and C. A. Grimes, "Synthesis of ordered arrays of discrete, partially crystalline titania nanotubes by Ti anodization using diethylene glycol electrolytes," *J. Mater. Chem.*, vol. 18, no. 28, pp. 3332–3336, 2008.

[64] L. Giorgi *et al.*, "Electrochemical synthesis of self-organized TiO2 crystalline

nanotubes without annealing," *Nanotechnology*, vol. 29, no. 9, Jan. 2018.

[65] W. Jun and L. Zhiqun, "Anodic formation of ordered TiO 2 nanotube arrays: Effects of electrolyte temperature and anodization potential," *J. Phys. Chem. C*, vol. 113, no. 10, pp. 4026–4030, 2009.

[66] L. K. Tsui, N. T. Nguyen, L. Wang, R. Kirchgeorg, G. Zangari, and P. Schmuki, "Hierarchical decoration of anodic TiO2 nanorods for enhanced photocatalytic degradation properties," *Electrochim. Acta*, vol. 155, pp. 244–250, 2015.

[67] F. Nasirpouri *et al.*, "Structural Defect-Induced Bandgap Narrowing in Dopant-Free Anodic TiO2 Nanotubes," *ChemElectroChem*, vol. 4, no. 5, pp. 1227–1235, 2017.

[68] B. Yang, C. K. Ng, M. K. Fung, C. C. Ling, A. B. Djurišić, and S. Fung, "Annealing study of titanium oxide nanotube arrays," *Mater. Chem. Phys.*, vol. 130, no. 3, pp. 1227–1231, 2011.

[69] P. Xiao, D. Liu, B. B. Garcia, S. Sepehri, Y. Zhang, and G. Cao, "Electrochemical and photoelectrical properties of titania nanotube arrays annealed in different gases," *Sensors Actuators, B Chem.*, vol. 134, no. 2, pp. 367–372, 2008.

[70] S. A. Ansari, M. M. Khan, M. O. Ansari, and M. H. Cho, "Nitrogen-doped titanium dioxide (N-doped TiO2) for visible light photocatalysis," *New Journal of Chemistry*, vol. 40, no. 4. Royal Society of Chemistry, pp. 3000–3009, 01-Apr-2016.

[71] C. Beer *et al.*, "Terrestrial gross carbon dioxide uptake: Global distribution and covariation with climate," *Science (80-.).*, vol. 329, no. 5993, pp. 834–838, Aug. 2010.

[72] Q. Lu and F. Jiao, "Electrochemical CO2 reduction: Electrocatalyst, reaction mechanism, and process engineering," *Nano Energy*, vol. 29, no. 29, pp. 439–456, Nov. 2016.

[73] K. Engeland, M. Borga, J. D. Creutin, B. François, M. H. Ramos, and J. P. Vidal, "Space-time variability of climate variables and intermittent renewable electricity production – A review," *Renew. Sustain. Energy Rev.*, vol. 79, no. May 2016, pp. 600–617, 2017.

[74] M. Momirlan and T. N. Veziroglu, "The properties of hydrogen as fuel

tomorrow in sustainable energy system for a cleaner planet," *Int. J. Hydrogen Energy*, vol. 30, no. 7, pp. 795–802, Jul. 2005.

[75] D. Wang *et al.*, "Photoelectrochemical water splitting with rutile TiO2 nanowires array: Synergistic effect of hydrogen treatment and surface modification with anatase nanoparticles," *Electrochim. Acta*, vol. 130, pp. 290–295, 2014.

[76] G. W. Luckey, "Introduction to Solid State Physics," *J. Am. Chem. Soc.*, vol. 79, no. 12, p. 3299, 1957.

[77] L. Clarizia, D. Spasiano, I. Di Somma, R. Marotta, R. Andreozzi, and D. D. Dionysiou, "Copper modified-TiO2 catalysts for hydrogen generation through photoreforming of organics. A short review," *Int. J. Hydrogen Energy*, vol. 39, no. 30, pp. 16812–16831, 2014.

[78] P. S. Shinde *et al.*, "Rapid Screening of Photoanode Materials Using Scanning Photoelectrochemical Microscopy Technique and Formation of Z-Scheme Solar Water Splitting System by Coupling p- and n-type Heterojunction Photoelectrodes," *ACS Appl. Energy Mater.*, vol. 1, no. 5, pp. 2283–2294, 2018.

[79] A. Fujishima and K. Honda, "Electrochemical photolysis of water at a semiconductor electrode," *Nature*, vol. 238, no. 5358, pp. 37–38, 1972.

[80] Y. Sun, G. Wang, and K. Yan, "TiO2 nanotubes for hydrogen generation by photocatalytic water splitting in a two-compartment photoelectrochemical cell," *Int. J. Hydrogen Energy*, vol. 36, no. 24, pp. 15502–15508, Dec. 2011.

[81] J. Li, "Distributed cooperative tracking of multi-agent systems with actuator faults," *Trans. Inst. Meas. Control*, vol. 37, no. 9, pp. 1041–1048, 2015.

[82] L. K. Tsui and G. Zangari, "Water content in the anodization electrolyte affects the electrochemical and electronic transport properties of TiO2 nanotubes: A study by electrochemical impedance spectroscopy," *Electrochim. Acta*, vol. 121, pp. 203–209, 2014.

[83] A. Di Paola, E. García-López, S. Ikeda, G. Marc, B. Ohtani, and L. Palmisano, "Photocatalytic degradation of organic compounds in aqueous systems by transition metal doped polycrystalline TiO2," *Catal. Today*, vol. 75, no. 1–4, pp. 87–93, Jul. 2002.

[84] M. Batzill, E. H. Morales, and U. Diebold, "Influence of nitrogen doping on the defect formation and surface properties of TiO2 rutile and anatase," *Phys. Rev.*

Lett., vol. 96, no. 2, Jan. 2006.

[85] T. Umebayashi, T. Yamaki, H. Itoh, and K. Asai, “Analysis of electronic structures of 3d transition metal-doped TiO2 based on band calculations,” *J. Phys. Chem. Solids*, vol. 63, no. 10, pp. 1909–1920, Oct. 2002.

[86] A. J. Cowan *et al.*, *One-Step Fabrication of CdS Nanorod Arrays via Solution Chemistry*, vol. 6, no. 1. Boston, MA: Springer US, 2015.

[87] A. Polman and H. A. Atwater, “Photonic design principles for ultrahigh-efficiency photovoltaics,” *Nat. Mater.*, vol. 11, no. 3, pp. 174–177, 2012.

[88] K. Sivula and R. Van De Krol, “Semiconducting materials for photoelectrochemical energy conversion,” *Nat. Rev. Mater.*, vol. 1, no. 2, Jan. 2016.

[89] Z. Chen, H. N. Dinh, and E. Miller, *Photoelectrochemical Water Splitting*, vol. 53, no. 24. New York, NY: Springer New York, 2013.

[90] R. Krol, “Principles of Photoelectrochemical Cells,” in *Photoelectro-chemical Hydrogen Production*, Springer, 2012, pp. 13–67.

[91] K. Zhu, T. B. Vinzant, N. R. Neale, and A. J. Frank, “Removing structural disorder from oriented TiO2 nanotube arrays: Reducing the dimensionality of transport and recombination in dye-sensitized solar cells,” *Nano Lett.*, vol. 7, no. 12, pp. 3739–3746, Dec. 2007.

[92] M. Wang, J. Ioccozia, L. Sun, C. Lin, and Z. Lin, “Inorganic-modified semiconductor TiO2 nanotube arrays for photocatalysis,” *Energy Environ. Sci.*, vol. 7, no. 7, pp. 2182–2202, 2014.

[93] K. A. Michalow *et al.*, “Synthesis, characterization and electronic structure of nitrogen-doped TiO2 nanopowder,” *Catal. Today*, vol. 144, no. 1–2, pp. 7–12, 2009.

[94] L. kun Tsui, Y. Xu, D. Dawidowski, D. Cafiso, and G. Zangari, “Efficient water oxidation kinetics and enhanced electron transport in Li-doped TiO2 nanotube photoanodes,” *J. Mater. Chem. A*, vol. 4, no. 48, pp. 19070–19077, 2016.

[95] L. Lei, Y. Su, M. Zhou, X. Zhang, and X. Chen, “Fabrication of multi-non-metal-doped TiO2 nanotubes by anodization in mixed acid electrolyte,” *Mater. Res. Bull.*, vol. 42, no. 12, pp. 2230–2236, 2007.

[96] Z. Huang, X. Wen, and X. Xiao, “Photoelectrochemical Properties of CuS-

TiO2 Composite Coating Electrode and Its Preparation via Electrophoretic Deposition," *J. Electrochem. Soc.*, vol. 158, no. 12, p. H1247, 2011.

[97] A. Franco, M. C. Neves, M. M. L. R. Carrott, M. H. Mendonça, M. I. Pereira, and O. C. Monteiro, "Photocatalytic decolorization of methylene blue in the presence of TiO2/ZnS nanocomposites," *J. Hazard. Mater.*, vol. 161, no. 1, pp. 545–550, 2009.

[98] S. Zhang, B. Peng, S. Yang, Y. Fang, and F. Peng, "The influence of the electrodeposition potential on the morphology of Cu2O/TiO2 nanotube arrays and their visible-light-driven photocatalytic activity for hydrogen evolution," *Int. J. Hydrogen Energy*, vol. 38, no. 32, pp. 13866–13871, 2013.

[99] M. Janczarek and E. Kowalska, "On the origin of enhanced photocatalytic activity of copper-modified titania in the oxidative reaction systems," *Catalysts*, vol. 7, no. 11, p. 317, Oct. 2017.

[100] Y. Wang *et al.*, "Electronic structures of C u2 O, C u4 O3, and CuO: A joint experimental and theoretical study," *Phys. Rev. B*, vol. 94, no. 24, 2016.

[101] L. K. Tsui, L. Wu, N. Swami, and G. Zangari, "Photoelectrochemical performance of electrodeposited Cu2O on TiO2 nanotubes," *ECS Electrochem. Lett.*, vol. 1, no. 2, pp. D15–D19, Jul. 2012.

[102] L. Huang *et al.*, "Controlled synthesis of octahedral Cu2O on TiO2 nanotube arrays by electrochemical deposition," *Mater. Chem. Phys.*, vol. 130, no. 1–2, pp. 316–322, 2011.

[103] M. Ichimura and Y. Kato, "Fabrication of TiO2/Cu2O heterojunction solar cells by electrophoretic deposition and electrodeposition," *Mater. Sci. Semicond. Process.*, vol. 16, no. 6, pp. 1538–1541, 2013.

[104] P. G. Schiavi, A. Rubino, P. Altimari, and F. Pagnanelli, "Two electrodeposition strategies for the morphology-controlled synthesis of cobalt nanostructures," in *AIP Conference Proceedings*, 2018, vol. 1990, no. July, p. 020005.

[105] L. Yang, M. Zhang, K. Zhu, J. Lv, G. He, and Z. Sun, "Electrodeposition of flake-like Cu 2 O on vertically aligned two-dimensional TiO 2 nanosheet array films for enhanced photoelectrochemical properties," *Appl. Surf. Sci.*, vol. 391, pp. 353–359, 2017.

[106] L. Assaud, V. Heresanu, M. Hanbücken, and L. Santinacci, "Fabrication of p/n

heterojunctions by electrochemical deposition of Cu 2O onto TiO2 nanotubes," *Comptes Rendus Chim.*, vol. 16, no. 1, pp. 89–95, 2013.

[107] W. Septina *et al.*, "Potentiostatic electrodeposition of cuprous oxide thin films for photovoltaic applications," *Electrochim. Acta*, vol. 56, no. 13, pp. 4882–4888, 2011.

[108] T. D. Golden, M. G. Shumsky, Y. Zhou, R. A. VanderWerf, R. A. Van Leeuwen, and J. A. Switzer, "Electrochemical Deposition of Copper(I) Oxide Films," *Chem. Mater.*, vol. 8, no. 10, pp. 2499–2504, 1996.

[109] L. Wu, L. K. Tsui, N. Swami, and G. Zangari, "Photoelectrochemical stability of electrodeposited Cu2O films," *J. Phys. Chem. C*, vol. 114, no. 26, pp. 11551–11556, Jul. 2010.

[110] L. Huang *et al.*, "Electrodeposition preparation of octahedral-Cu2O-loaded TiO 2 nanotube arrays for visible light-driven photocatalysis," *Scr. Mater.*, vol. 63, no. 2, pp. 159–161, 2010.

[111] Y. Yang, Y. Li, and M. Pritzker, "Control of Cu2O Film Morphology Using Potentiostatic Pulsed Electrodeposition," *Electrochim. Acta*, vol. 213, pp. 225–235, 2016.

[112] Y. Zhou and J. A. Switzer, "Electrochemical deposition and microstructure of copper (I) oxide films," *Scr. Mater.*, vol. 38, no. 11, pp. 1731–1738, 1998.

[113] S. Bijani, R. Schrebler, E. A. Dalchiele, M. Gabás, L. Martínez, and J. R. Ramos-Barrado, "Study of the nucleation and growth mechanisms in the electrodeposition of micro- and nanostructured Cu2O thin films," *J. Phys. Chem. C*, vol. 115, no. 43, pp. 21373–21382, 2011.

[114] K. Mocala, A. Navrotsky, and D. M. Sherman, "High-temperature heat capacity of Co3O4 spinel: thermally induced spin unpairing transition," 1992.

[115] A. B. Ribeiro, E. P. Mateus, and N. Couto, *Electrokinetics across disciplines and continents: New strategies for sustainable development*. 2016.

[116] K. R. Reddy and C. Cameselle, *Electrochemical Remediation Technologies for Polluted Soils, Sediments and Groundwater*. Hoboken, NJ, USA: John Wiley & Sons, Inc., 2009.

[117] Y. B. Acar and A. N. Alshawabkeh, "Principles of Electrokinetic Remediation," *Environ. Sci. Technol.*, vol. 27, no. 13, pp. 2638–2647, 1993.

[118] L. M. Ottosen, A. J. Pedersen, A. B. Ribeiro, and H. K. Hansen, “Case study on the strategy and application of enhancement solutions to improve remediation of soils contaminated with Cu, Pb and Zn by means of electrodialysis,” *Eng. Geol.*, vol. 77, no. 3-4 SPEC. ISS., pp. 317–329, Mar. 2005.

[119] P. Guedes, N. Couto, L. M. Ottosen, and A. B. Ribeiro, “Phosphorus recovery from sewage sludge ash through an electrodialytic process,” *Waste Manag.*, vol. 34, no. 5, pp. 886–892, 2014.

[120] P. Guedes, E. P. Mateus, J. Almeida, A. R. Ferreira, N. Couto, and A. B. Ribeiro, “Electrodialytic treatment of sewage sludge: Current intensity influence on phosphorus recovery and organic contaminants removal,” *Chem. Eng. J.*, vol. 306, pp. 1058–1066, 2016.

[121] L. M. Ottosen, H. K. Hansen, and C. B. Hansen, “Water splitting at ion-exchange membranes and potential differences in soil during electrodialytic soil remediation,” *J. Appl. Electrochem.*, vol. 30, no. 11, pp. 1199–1207, 2000.

[122] C. Magro, J. Almeida, J. M. Paz-Garcia, E. P. Mateus, and A. B. Ribeiro, “Exploring hydrogen production for self-energy generation in electroremediation: A proof of concept,” *Appl. Energy*, vol. 255, p. 113839, Dec. 2019.

[123] L. M. Ottosen, H. K. Hansen, S. Laursen, and A. Villumsen, “Electrodialytic remediation of soil polluted with copper from wood preservation industry,” *Environ. Sci. Technol.*, vol. 31, no. 6, pp. 1711–1715, Jun. 1997.

[124] T. R. Sun and L. M. Ottosen, “Effects of pulse current on energy consumption and removal of heavy metals during electrodialytic soil remediation,” in *Electrochimica Acta*, 2012, vol. 86, pp. 28–35.

[125] A. Rojo and L. Cubillos, “Electrodialytic remediation of copper mine tailings using bipolar electrodes,” *J. Hazard. Mater.*, vol. 168, no. 2–3, pp. 1177–1183, Sep. 2009.

[126] A. Tahira *et al.*, “Advanced Electrocatalysts for Hydrogen Evolution Reaction Based on Core-Shell MoS2/TiO2 Nanostructures in Acidic and Alkaline Media,” *ACS Appl. Energy Mater.*, vol. 2, no. 3, pp. 2053–2062, 2019.

[127] L. Chen, X. Dong, Y. Wang, and Y. Xia, “Separating hydrogen and oxygen evolution in alkaline water electrolysis using nickel hydroxide,” *Nat. Commun.*, vol. 7, no. May, pp. 1–8, 2016.

[128] Y. Yan, B. Y. Xia, B. Zhao, and X. Wang, “A review on noble-metal-free bifunctional heterogeneous catalysts for overall electrochemical water splitting,” *J. Mater. Chem. A*, vol. 4, no. 45, pp. 17587–17603, 2016.

[129] Y. Yan, B. Xia, Z. Xu, and X. Wang, “Recent development of molybdenum sulfides as advanced electrocatalysts for hydrogen evolution reaction,” *ACS Catal.*, vol. 4, no. 6, pp. 1693–1705, 2014.

[130] J. Wang, W. Cui, Q. Liu, Z. Xing, A. M. Asiri, and X. Sun, “Recent Progress in Cobalt-Based Heterogeneous Catalysts for Electrochemical Water Splitting,” *Adv. Mater.*, vol. 28, no. 2, pp. 215–230, 2016.

[131] S. K. Mohapatra, M. Misra, V. K. Mahajan, and K. S. Raja, “Design of a highly efficient photoelectrolytic cell for hydrogen generation by water splitting: Application of TiO 2-xC x nanotubes as a photoanode and Pt/TiO 2 nanotubes as a cathode,” *J. Phys. Chem. C*, vol. 111, no. 24, pp. 8677–8685, 2007.

[132] R. Vadakkekara, R. Illathvalappil, and S. Kurungot, “Layered TiO2 Nanosheet-Supported NiCo2O4 Nanoparticles as Bifunctional Electrocatalyst for Overall Water Splitting,” *ChemElectroChem*, vol. 5, no. 24, pp. 4000–4007, 2018.

[133] W. Xie *et al.*, “Electrocatalytic activity of Pd-loaded Ti/TiO2 nanotubes cathode for TCE reduction in groundwater,” *Water Res.*, vol. 47, no. 11, pp. 3573–3582, 2013.

[134] S. Marini *et al.*, “Advanced alkaline water electrolysis,” *Electrochim. Acta*, vol. 82, pp. 384–391, 2012.

[135] J. X. Feng, H. Xu, Y. T. Dong, X. F. Lu, Y. X. Tong, and G. R. Li, “Efficient Hydrogen Evolution Electrocatalysis Using Cobalt Nanotubes Decorated with Titanium Dioxide Nanodots,” *Angew. Chemie - Int. Ed.*, vol. 56, no. 11, pp. 2960–2964, 2017.

[136] Y. Yan *et al.*, “Plasma Hydrogenated TiO2/Nickel Foam as an Efficient Bifunctional Electrocatalyst for Overall Water Splitting,” *ACS Sustain. Chem. Eng.*, vol. 7, no. 1, pp. 885–894, 2019.

[137] R. E. Fuentes, J. Farell, and J. W. Weidner, “Multimetallic electrocatalysts of Pt, Ru, and Ir supported on anatase and rutile TiO2 for oxygen evolution in an acid environment,” *Electrochem. Solid-State Lett.*, vol. 14, no. 3, p. E5, 2011.

[138] W. Hu, S. Chen, and Q. Xia, “IrO2/Nb-TiO2 electrocatalyst for oxygen evolution reaction in acidic medium,” *Int. J. Hydrogen Energy*, vol. 39, no. 13,

pp. 6967–6976, 2014.

[139] Z. X. Lu, Y. Shi, C. F. Yan, C. Q. Guo, and Z. Da Wang, “Investigation on IrO2 supported on hydrogenated TiO2 nanotube array as OER electro-catalyst for water electrolysis,” *Int. J. Hydrogen Energy*, vol. 42, no. 6, pp. 3572–3578, 2017.

[140] H. Feng *et al.*, “Activating Titania for Efficient Electrocatalysis by Vacancy Engineering,” *ACS Catal.*, vol. 8, no. 5, pp. 4288–4293, May 2018.

[141] O’SULLIVAN JP and WOOD GC, “Morphology and mechanism of formation of porous anodic films on aluminum,” *Proc Roy Soc Ser A Math Phys Sci*, vol. 317, no. 1731, 1970.

[142] X. Z. Ding, X. H. Liu, and Y. Z. He, “Grain size dependence of anatase-to-rutile structural transformation in gel-derived nanocrystalline titania powders,” *J. Mater. Sci. Lett.*, vol. 15, no. 20, pp. 1789–1791, 1996.

[143] S. Sreekantan, R. Hazan, and Z. Lockman, “Photoactivity of anatase-rutile TiO2 nanotubes formed by anodization method,” *Thin Solid Films*, vol. 518, no. 1, pp. 16–21, 2009.

[144] S. Zhang, S. Zhang, F. Peng, H. Zhang, H. Liu, and H. Zhao, “Electrodeposition of polyhedral Cu2O on TiO2 nanotube arrays for enhancing visible light photocatalytic performance,” *Electrochem. commun.*, vol. 13, no. 8, pp. 861–864, 2011.

[145] J. Torrent and V. Barron, “Diffuse reflectance spectroscopy of iron oxides,” *Encycl. Surf. Colloid Sci.*, pp. 1438–1446, 2002.

[146] M. Radecka *et al.*, “Ti0 2-based nanopowders and thin films for photocatalytical applications,” *J. Nanosci. Nanotechnol.*, vol. 10, no. 2, pp. 1032–1042, 2010.

[147] J. Tauc, “Absorption edge and internal electric fields in amorphous semiconductors,” *Mater. Res. Bull.*, vol. 5, no. 8, pp. 721–729, 1970.

[148] A. Rubino, P. G. Schiavi, P. Altimari, A. Latini, and F. Pagnanelli, “Ti/TiO2/Cu2O based electrodes as photocatalysts in PEC cells,” *Chem. Eng. Trans.*, vol. 73, pp. 73–78, 2019.

[149] J. Li, L. Liu, Y. Yu, Y. Tang, H. Li, and F. Du, “Preparation of highly photocatalytic active nano-size TiO 2-Cu 2O particle composites with a novel

electrochemical method," *Electrochem. commun.*, vol. 6, no. 9, pp. 940–943, 2004.

[150] M. Wang, L. Sun, Z. Lin, J. Cai, K. Xie, and C. Lin, "P-n Heterojunction photoelectrodes composed of Cu2O-loaded TiO2 nanotube arrays with enhanced photoelectrochemical and photoelectrocatalytic activities," *Energy Environ. Sci.*, vol. 6, no. 4, pp. 1211–1220, 2013.

[151] L. Sang, J. Zhang, Y. Zhang, Y. Zhao, and J. Lin, " Preparation of Cu 2 O/TiO 2 nanotube arrays and their photoelectrochemical properties as hydrogen-evolving photoanode ," *Sol. Hydrog. Nanotechnol. X*, vol. 9560, p. 95600M, 2015.

[152] L. X. Sang, Z. Zhi-Yu, B. Guang-Mei, D. Chun-Xu, and M. Chong-Fang, "A photoelectrochemical investigation of the hydrogen-evolving doped TiO 2 nanotube arrays electrode," *Int. J. Hydrogen Energy*, vol. 37, no. 1, pp. 854–859, Jan. 2012.

[153] J. H. Yun, Y. H. Ng, C. Ye, A. J. Mozer, G. G. Wallace, and R. Amal, "Sodium fluoride-assisted modulation of anodized TiO 2 nanotube for dye-sensitized solar cells application," *ACS Appl. Mater. Interfaces*, vol. 3, no. 5, pp. 1585–1593, May 2011.

[154] P. Peerakiatkhajohn, J.-H. Yun, S. Wang, and L. Wang, "Review of recent progress in unassisted photoelectrochemical water splitting: from material modification to configuration design," *J. Photonics Energy*, vol. 7, no. 1, p. 012006, 2016.

[155] Z. Zhang and P. Wang, "Highly stable copper oxide composite as an effective photocathode for water splitting via a facile electrochemical synthesis strategy," *J. Mater. Chem.*, vol. 22, no. 6, pp. 2456–2464, 2012.

[156] X. Xu *et al.*, "Synthesis of Cu2O Octadecahedron/TiO2 Quantum Dot Heterojunctions with High Visible Light Photocatalytic Activity and High Stability," *ACS Appl. Mater. Interfaces*, vol. 8, no. 1, pp. 91–101, 2016.

[157] H. Yin, X. Wang, L. Wang, Q. Nie, Y. Zhang, and W. Wu, "Cu2O/TiO2 heterostructured hollow sphere with enhanced visible light photocatalytic activity," *Mater. Res. Bull.*, vol. 72, pp. 176–183, 2015.

[158] J. Xue, M. Shao, Q. Shen, X. Liu, and H. Jia, "Electrodeposition of Cu2O nanocrystalline on TiO2 nanosheet arrays by chronopotentiometry for

improvement of photoelectrochemical properties," *Ceram. Int.*, vol. 44, no. 10, pp. 11039–11047, 2018.

[159] Z. Zhang, M. N. Hedhili, H. Zhu, and P. Wang, "Electrochemical reduction induced self-doping of Ti3+ for efficient water splitting performance on TiO2 based photoelectrodes," *Phys. Chem. Chem. Phys.*, vol. 15, no. 37, pp. 15637–15644, Oct. 2013.

[160] L. Zhao, W. Dong, F. Zheng, L. Fang, and M. Shen, "Interrupted growth and photoelectrochemistry of Cu 2O and Cu particles on TiO 2," *Electrochim. Acta*, vol. 80, pp. 354–361, 2012.

[161] G. Li, N. M. Dimitrijevic, L. Chen, T. Rajh, and K. A. Gray, "Role of surface/interfacial Cu2+ sites in the photocatalytic activity of coupled CuO-TiO2 nanocomposites," *J. Phys. Chem. C*, vol. 112, no. 48, pp. 19040–19044, 2008.

[162] J. Yu and J. Ran, "Facile preparation and enhanced photocatalytic H2-production activity of Cu(OH)2 cluster modified TiO2," *Energy Environ. Sci.*, vol. 4, no. 4, pp. 1364–1371, 2011.

[163] H. Dang, X. Dong, Y. Dong, Y. Zhang, and S. Hampshire, "TiO2 nanotubes coupled with nano-Cu(OH)2 for highly efficient photocatalytic hydrogen production," *Int. J. Hydrogen Energy*, vol. 38, no. 5, pp. 2126–2135, 2013.

[164] C. Zhu, A. Osherov, and M. J. Panzer, "Surface chemistry of electrodeposited Cu2O films studied by XPS," *Electrochim. Acta*, vol. 111, pp. 771–778, 2013.

[165] M. R. Baklanov *et al.*, "Characterization of Cu surface cleaning by hydrogen plasma," *J. Vac. Sci. Technol. B Microelectron. Nanom. Struct.*, vol. 19, no. 4, pp. 1201–1211, 2001.

[166] B. Vanrenterghem, M. Bele, F. R. Zepeda, M. Šala, N. Hodnik, and T. Breugelmans, "Cutting the Gordian Knot of electrodeposition via controlled cathodic corrosion enabling the production of supported metal nanoparticles below 5 nm," *Appl. Catal. B Environ.*, vol. 226, no. December 2017, pp. 396–402, 2018.

[167] M. Johnsson, K. W. Tornroos, F. Mila, and P. Millet, "Tetrahedral clusters of copper(II): Crystal structures and magnetic properties of Cu2Te2O5X2 (X = Cl. Br)," *Chem. Mater.*, vol. 12, no. 10, pp. 2853–2857, 2000.

[168] C. H. B. Ng and W. Y. Fan, "Facile synthesis of single-crystalline y-cul

nanotetrahedrons and their induced transformation to tetrahedral CuO nanocages," *J. Phys. Chem. C*, vol. 111, no. 26, pp. 9166–9171, 2007.

[169] N. Liu *et al.*, "Black TiO2 nanotubes: Cocatalyst-free open-circuit hydrogen generation," *Nano Lett.*, vol. 14, no. 6, pp. 3309–3313, Jun. 2014.

[170] C. Mao, F. Zuo, Y. Hou, X. Bu, and P. Feng, "In Situ Preparation of a Ti3+ Self-Doped TiO2 Film with Enhanced Activity as Photoanode by N2H4 Reduction," *Angew. Chemie - Int. Ed.*, vol. 53, no. 39, pp. 10485–10489, Sep. 2014.

[171] Y. Teng and F. Teng, "Investigation on surface metal vacancy electrochemistry," *Electrochim. Acta*, vol. 244, pp. 1–7, Aug. 2017.

[172] Y. Wang *et al.*, "Layered Double Hydroxide Nanosheets with Multiple Vacancies Obtained by Dry Exfoliation as Highly Efficient Oxygen Evolution Electrocatalysts," *Angew. Chemie - Int. Ed.*, vol. 56, no. 21, pp. 5867–5871, 2017.

[173] G. M. Kirkelund, P. E. Jensen, and L. M. Ottosen, "Electrodialytic Extraction of Heavy Metals from Greenlandic MSWI Fly Ash As a Function of Remediation Time and L/S ratio," in *ISCORD 2013*, 2013, pp. 87–96.

[174] P. G. Fernandez, H. G. Linge, and M. W. Wadsley, "Oxidation of arsenopyrite (FeAsS) in acid Part I: Reactivity of arsenopyrite," *J. Appl. Electrochem.*, vol. 26, no. 6, pp. 575–583, 1996.